Review on the correlation between microstructure and mechanical performance for laser powder bed fusion AlSi10Mg

Lv Zhao[a,c], Lubin Song[a], Juan Guillermo Santos Macías[b], Yaxin Zhu[a,c], Minsheng Huang[a,c], Aude Simar[b], Zhenhuan Li[a,c*]

[a] *Huazhong University of Science and Technology, School of Aerospace Engineering, Department of Mechanics, Wuhan, China*

[b] *Université catholique de Louvain, Institute of Mechanics, Materials and Civil Engineering, IMAP, B-1348 Louvain la Neuve, Belgium*

[c] *Hubei Key Laboratory of Engineering Structural Analysis and Safety Assessment, Wuhan, China*

[*] Corresponding author. Email address: zhenhuanli@hust.edu.cn

Abstract

As important structural materials widely used in aerospace and automotive industries, aluminum alloys are perfect candidates for development of laser metal additive manufacturing (AM). Amongst AM aluminum alloys, laser powder bed fusion (LPBF) AlSi10Mg has received substantial attention due to its good printability and relatively low cost. Great efforts have been devoted to seek optimum process parameters that can enhance mechanical performance. However, a large scattering of material properties arises from the literature data, especially for the as built state, thus casting a shadow over further development of LPBF Al alloys. This review article aims to summarize the recent progresses on the characterization of microstructure, assessment of strengthening and damage mechanisms, evaluation of fracture and fatigue resistance, and attempts to build a primary comprehensive link between mechanical performance and microstructure for the as built state. Following the analysis of the state of the art, the review will finally provide an outlook on additional efforts needed to quantify the microstructure-property relation, based on which maximizing the potential of mechanical performance through optimizing microstructure may be achieved.

Keywords: Laser powder bed fusion, AlSi10Mg, Microstructure, Strength, Ductility, Fatigue

Contents

1. Introduction

Laser powder bed fusion (LPBF, also called selective laser melting, or SLM in short) is one of the most commonly used metal additive manufacturing (AM) techniques [1, 2]. When building parts, one or multiple laser beams scan and melt powder previously deposited on a build platform, following prescribed scanning paths to achieve a designed 3D geometry. After the current powder layer is selectively melted and solidifies, another layer of powder is laid and the laser scanning continues to proceed. Such operation will be repeated until the whole part is built. LPBF metals are therefore composed of metallurgically fused layers, sharing some characteristics with the laser welding process while involving a much higher cooling rate.

Among LPBF metals, AlSi10Mg stands out for its excellent printability and strength-to-weight ratio, granting this AM-Al alloy couple great potential for aerospace applications. Indeed, LPBF AlSi10Mg has been selected as candidate material for various spacecraft and aircraft structures, as recently reviewed by Blakey-Milner et al. [3]. In collaboration with EOS and Altair, RUAG designed and produced an optimized version of an existing antenna bracket for the latest Sentinel Earth observation satellite, allowing for a 40 percent weight reduction compared to the original version manufactured by conventional techniques [4]. With the help of topology optimization and AM techniques, RUAG and Altair also designed and produced the star tracker camera bracket for the CARBONITE-2 satellite using EOS machines [5]. This structure underwent various testing procedures such as computed tomography scans, geometric

analysis, tensile, microscopy and structural response testing. The manufactured LPBF AlSi10Mg components passed all testing criteria with comfortable margins [6]. Airplane manufacturers also turned to AM techniques, in particular AM Al alloys, for new commercial aircrafts. Working with Airbus and EOS, Sogeti succeeded in developing the vertical tail plane bracket for the new A350 XWB using LPBF AlSi10Mg [7]. Benefiting from the AM advantages, the production time was reduced from 70 days to only 19 hours. Moreover, the structure could be manufactured in a single run, whereas the conventionally produced component incorporated more than 30 individual parts. These industrial examples demonstrate the attractiveness of additively manufactured AlSi10Mg for creating lightweight components that can be approved for flight.

With the development of metal additive manufacturing, many other compositions of aluminum alloys have been attempted for LPBF, already achieving some success, for example Al 7075+Zr [8], Al-Zn-Mg-Cu [9-11], Al-Cu [12], Al-Mg-Si-Zr [13], Al-Mg-Si-Sc-Zr [14], Al-Mn-Si-Sc-Zr [15], Al-Li [16], Al-Cu-Mg-Li-Zr [17], Al-Mg-Sc-Zr [18], Al-Zn-Mg-Sc-Zr [19], Al 5083 [20, 21], Al 6061 [22], Al 6063 [23] and Al-Si alloys with modifications [24]. Note that this review article is dedicated to AlSi10Mg given its relatively higher maturity, seeking the comprehensive correlation between microstructure and mechanical performance based on solid ground of research data and raising perspectives for further development.

Indeed, LPBF AlSi10Mg has been investigated for more than 10 years, quite rich data have been documented in literature, allowing to understand its microstructure [25-31], defects [29, 32-38], strength [26, 39-44], ductility [27, 45-47], fracture [48, 49] and fatigue resistance [50-57]. Originating from the intrinsic features of laser-metal additive manufacturing, such as high cooling rate (up to 10^6 K/s [58]), strong thermal gradient (in the order of 10^6 K/m [59]) and complex laser-powder-melt pool interdependency dynamics [60], LPBF AlSi10Mg exhibits a hierarchical, trans-scale and heterogeneous microstructure [30], non-negligible porosity

(despite being in the order of 0.1% [61]) and important residual stresses [38]. As a consequence, built parts present relatively low ductility (generally lower than 10%) and unsatisfactory fatigue resistance, both still involving quite large scatter. To tackle these issues, great efforts have been devoted to develop post-treatments, based on either heat treatments or thermo-mechanical treatments, for instance direct annealing [62, 63], T6-like treatment [64], hot isostatic pressing (HIP) [65, 66] or friction stir processing (FSP) [57, 61, 63]. So far, no post-treatment can improve ductility and fatigue resistance while maintaining the initial high strength imparted by the fine microstructure. Nevertheless, there are some instances of potentially satisfactory compromises, e.g. a 448% increase in ductility and a fatigue life enhancement over two orders of magnitude after friction stir processing, with only a 34% decrease in yield strength [61].

Still, researchers continue to explore LPBF AlSi10Mg, with tremendous efforts not only from the industrial community seeking further process parameter optimization, but also from the field of mechanics of materials studying the link between microstructure and mechanical properties. The combination of both efforts will allow to establish the roadmap from optimum process parameters to sound microstructure and finally to desired mechanical performance or function [67]. Especially with the development of machine learning (ML) or deep learning (DL), researchers started to seek optimum parameter window [59, 68], assess internal porosity defects [69] and predict mechanical properties [70] using the ML method, the rich data on metal additive manufacturing being a perfect playground. Moreover, using advanced in situ testing techniques, operated with transmission scanning microscopy (TEM), synchrotron X-ray diffraction (SXRD) or neutron diffraction, the fundamental deformation mechanism [39], the internal stress partition between phases [44, 71] and the evolution of initial porosity during deformation [72] can be qualitatively or quantitatively probed. Therefore, comprehensive correlation between microstructure and mechanical performance is of great interest and will be the focus of investigations in the future.

This review will be mainly focused on the as built condition, the reviewed mechanical properties are mainly characterized with machined or polished samples, aiming to exclusively understand the role of the core microstructure and internal defects in the determination of mechanical performance while eliminating the influence of build surface roughness and machining flaws (in particular for fatigue assessment). Note that review papers on LPBF aluminum alloys increasingly emerged during the last few years. Readers may refer to Aboulkhair et al. [73], Zhang et al. [74], Fiocchi et al. [75], Ponnusamy et al. [76], Kotadia et al. [77] who paid more attention to alloy compositions and post-treatments. The present review will be focused on as built LPBF AlSi10Mg, systematically addressing microstructure, defects, strength, ductility (strengthening and damage mechanisms), fracture toughness, fatigue resistance, and their correlations, which, according to the authors, have not been fully established for the as built condition in literature.

2. Microstructure

Additively manufactured metals are known to present unique microstructure different from their counterparts produced by conventional methods [73, 78]. A comparison between as cast AlSi10Mg and as built LPBF AlSi10Mg is shown in Fig. 1. In general, the LPBF process leads to a markedly finer microstructure and a different microstructure morphology.

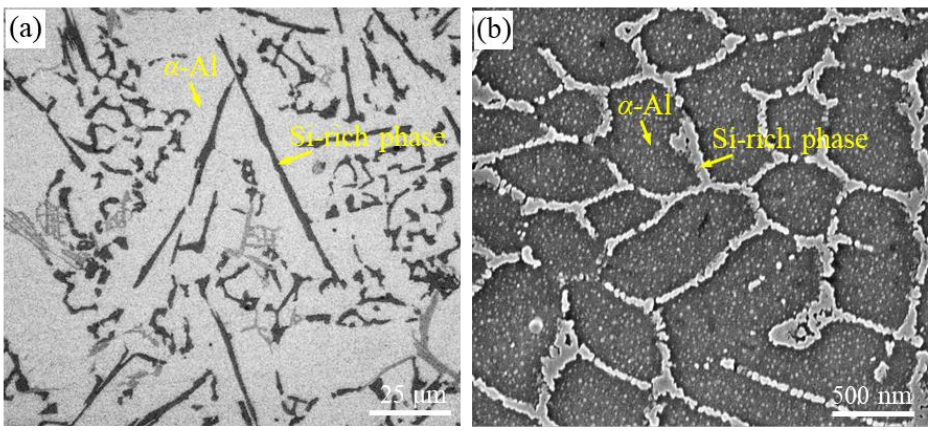

Fig. 1. Typical microstructure of as cast (a) and as built LPBF (b) AlSi10Mg. Note that the scale bars have the same physical length in (a) and (b).

As illustrated in Fig. 2, the LPBF process involves a moving heating source that rapidly melts metallic powder, the later then cools down and solidifies in a very short time, leading to a new deposit layer fused with the substrate (previous layer). This manufacturing process has a multi-physics nature and generates a specific microstructure in the printed part [60, 79].

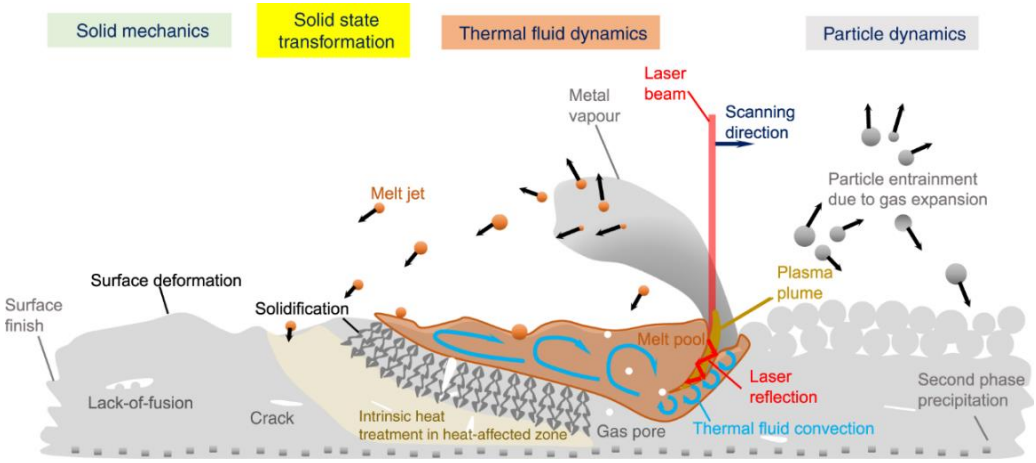

Fig. 2. Schematic illustration of the laser powder bed fusion process showing its complex multi-physics nature involving solid mechanics, solid state transformation, thermal fluid dynamics, and particle dynamics-porosity [79]. Such complex process could produce surface roughness, internal defects, residual stresses, microstructure heterogeneity, etc. The figure is reprinted with permission from Springer Nature.

Indeed, due to the high cooling speed (up to 10^6 K/s) [58] , strong thermal gradient (in the order of 10^6 K/m) [59] and variant thermal cycles seen by different zones, LPBF AlSi10Mg exhibits a quite complex microstructure, which is reflected by its trans-scale, hierarchical and heterogeneous characteristics. This section will first review these aspects separately and then depict the influence of manufacturing parameters.

2.1 Trans-scale aspect

As illustrated in Fig. 3, at different scales, the main structures of LPBF AlSi10Mg can be supersaturated atoms and their clusters (10^{-10}-10^{-9} m), nano-particles (10^{-9}-10^{-8} m), Si-rich eutectic networks (10^{-7}-10^{-8} m), grains and melt pools (10^{-5}-10^{-4} m). In fact, the microstructure of many metallic materials presents trans-scale features. For instance, heat-treatable Al alloys

contain nanoscale precipitates and microscale grains. However, the trans-scale microstructure of LPBF AlSi10Mg is associated with more characteristic lengths, mainly due to the presence of Si-rich eutectic between ultrafine particles and coarse grains and melt pool structures much larger than individual grains.

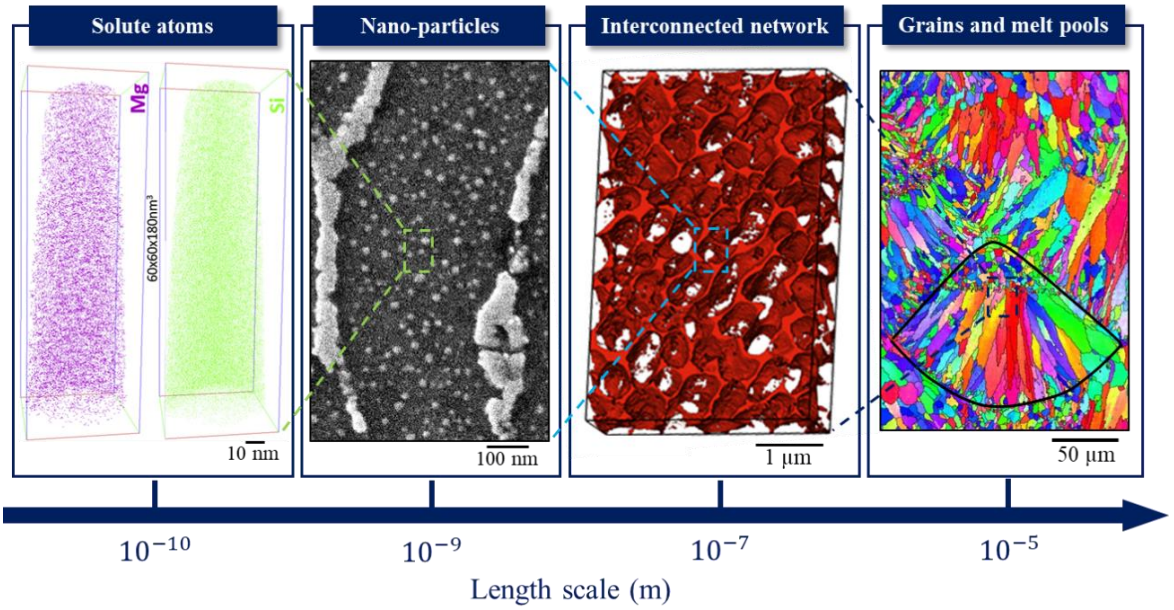

Fig. 3. Trans-scale aspect of the LPBF AlSi10Mg microstructure, from angstrom-size solute atoms [25], nano particles [27], and submicron-thick network (cells) [26], to micron sized grains and melt pools [26].

The trans-scale microstructure of LPBF AlSi10Mg spans over five orders of magnitude in the length scale and involves four structure features (Fig. 3), all playing important roles in determining macroscopic mechanical behavior, as will be discussed in sections 4, 5 and 6. The following subsections will review relevant works on each structure feature.

2.1.1 Solid solution

Rapid cooling from the melted state leads to a supersaturated matrix for LPBF Al-Si alloys [62, 80-82]. A detailed analysis of the supersaturated aluminum matrix was recently performed by Lefebvre et al. [25] on AlSi10Mg (built with 35°C platform temperature) with atom probe tomography (APT). It was found that the average solid solution content within the Al matrix is 3 at.% for Si and 0.14 at.% for Mg, the Si content being significantly higher than the theoretical

solubility of the element, i.e., approximately1.6 wt.% [25, 80].

In addition to dispersed Mg and Si solute atoms, two populations of atom clusters were identified by APT, namely Mg-free (containing Al) and Mg-rich (containing Si) clusters, as shown in Fig. 4a and b, respectively [25]. For the Mg-rich clusters, the Mg: Si ratio presents a large span, from roughly 0.3 to 6 (see Fig. 4c), indicating a high possibility of Mg_2Si absence. Note that Mg_2Si precipitates may be formed in as built LPBF AlSi10Mg with build platform preheating, as identified by scanning transmission electron microscopy (STEM) [83] (see section 2.4). Regarding the Si-rich clusters, the fraction of Si generally exceeds 50% (Fig. 4d), significantly higher than the average content (roughly 3 at.%) of Si in the Al matrix. Similar APT characterization results were obtained by Maeshima et al. [84]. Such supersaturation indicates that the high cooling rate leads to an extreme non-equilibrium state, which can even evolve when holding the built part at room temperature. Indeed, Fite et al. [85] reported a 16% decrease of Si solution content after approximately 3000 hours hold under ambient conditions. However, the Si solution reduction does not significantly influence the material hardness.

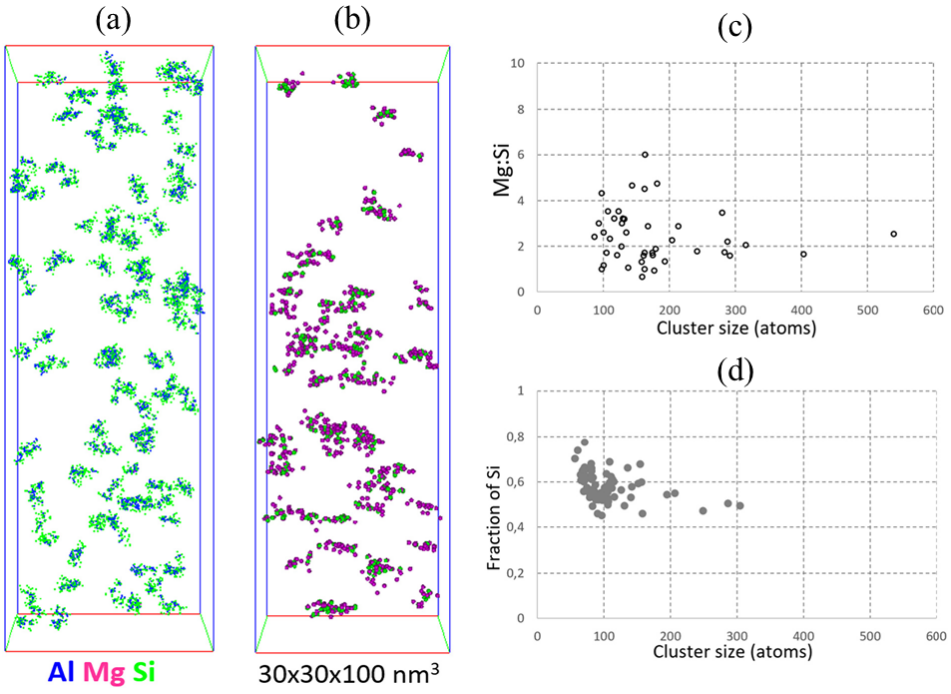

Fig. 4. Supersaturated Si and Mg atoms in Al matrix viewed by APT [25]. Si-rich atom clusters (a),

Mg-rich atom clusters (b), Mg: Si ratio in clusters in (b) (c), fraction of Si in clusters shown in (a) (d). The figures are reprinted with permission from Elsevier.

2.1.2 Nanosized Si-rich particles

The Al matrix may also incorporate nanosized Si-rich particles that present varying shapes and sizes depending on manufacturing parameters [26, 27, 29, 42, 86-88]. In fact, the presence of nanosized particle-like features has been reported relatively longtime ago in literature, mainly based on TEM observations [39, 84, 85]. Their identification was however only limited to the shape description in the early time. The Si-rich nature of nanosized particles within the Al matrix has been recently confirmed by sophisticated TEM characterization, via energy dispersive X-ray spectroscopy (EDS) mapping, high-resolution TEM (HRTEM) or fast Fourier transform (FFT) patterns (see Fig. 5).

When the build platform is not or just slightly heated (35°C for example), the Si-rich particles are generally spherical and present an equivalent diameter around 10 nm, as reported by Zhao et al. [27] and Wu et al. [29] (Fig. 5a, d and e). The average size of Si-rich particles could grow up to 60 nm [26, 42] in the case of 200°C preheated platform. The crystal nature of the Si-rich particles is further demonstrated by FFT patterns for both small and relatively large sizes, as illustrated in Fig. 5d-e and Fig. 5b-c, respectively. It is worth mentioning that Takata et al. [41] employed HRTEM and FFT to carefully investigate nanosized puncta in their samples (without platform preheating), but no clear reflections of crystalline structure were detected, excluding the possibility of Si or Mg_2Si precipitation. The authors proposed that the puncta observed in TEM micrograph corresponded to the solution clusters revealed by APT (Fig. 4).

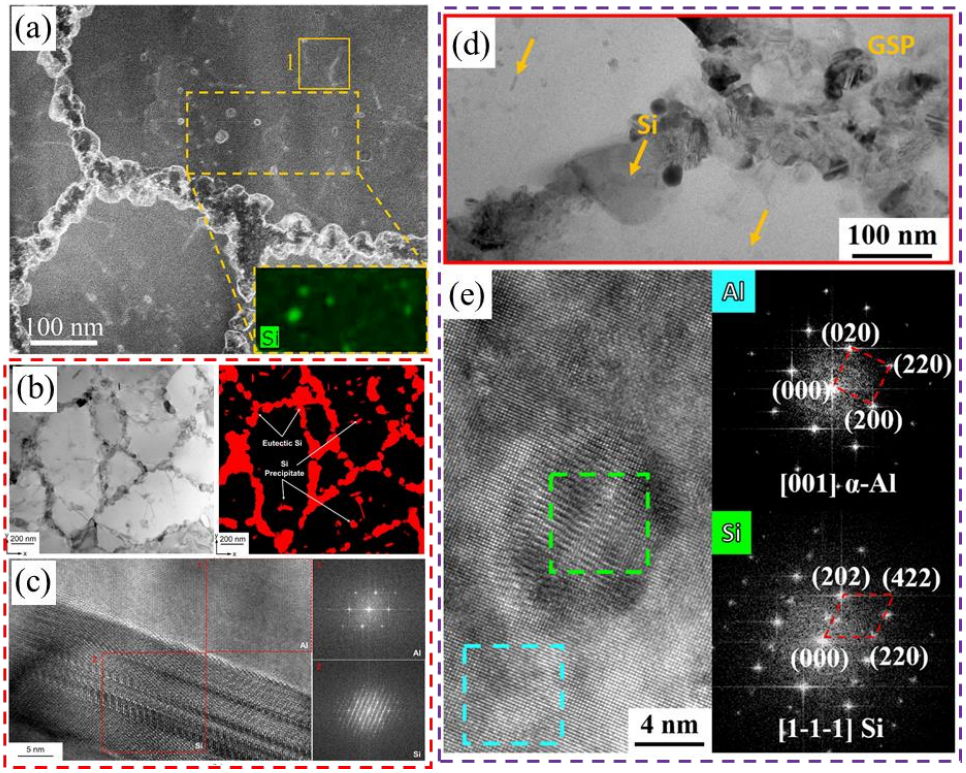

Fig. 5. Si-rich nanosized particles embedded in Al matrix characterized by TEM. HAADF/EDS map showing the Si-rich nature in a sample manufactured on a slightly preheated build platform (35°C) [27] (a), STEM-BF/EDS map (b) and HRTEM/FFT patterns (c) revealing the Si-precipitate in a sample manufactured using build platform preheating (200°C) [42], TEM-BF (d) and HRTEM/FFT patterns (e) revealing the Si-precipitate in a sample manufactured on a slightly preheated build platform (35°C) [29]. The images in (b) are taken with the beam direction along the low-index zone axis orientation of Al, the FFTs in (e) indicate an orientation relationship of ($[001]_{Al}$//$[1\text{-}1\text{-}1]_{Si}$ and $(020)_{Al}$ //$(202)_{Si}$) between the α-Al matrix and the precipitate. The figures are reprinted with permission from Elsevier.

From the abovementioned studies, it can be concluded that nanosized Si-rich particles exist only under certain manufacturing conditions and the precursor for their formation seems to be related to thermal history. Indeed, Hadadzadeh et al. [28] recently demonstrated that the Si precipitates exhibited different characteristics (size and density) at different sampling heights experiencing different thermal cycles. However, no systematic investigation has been performed to figure out the combination of process parameters and platform preheating

temperature leading to nanosized precipitate formation, as will be discussed in section 2.4. In addition, the analysis of nanosized particles was generally limited to fine melt pool zone in previous studies, whereas their size and distribution in different zones remain to be thoroughly assessed as it will be important in determining the local strength and consequently the deformation mechanism of built samples. Note that the nanosized particles could significantly enhance mechanical strength, as will be revealed in section 4.2.1.

2.1.3 Si-rich eutectic network

The Si element manifests mainly in the form of Si-rich eutectic in LPBF AlSi10Mg [30, 50, 62, 82], similarly to its cast counterpart [89]. However, the high cooling rate of LPBF leads to ultrafine eutectic dendrite enclosing the α-Al phase. The fast solidification could also render the eutectic metastable. As revealed by HRTEM (Fig. 6), the Si-rich eutectic has been found to mainly contain amorphous structures, in which local ordering (i.e., diamond Si) is dispersedly embedded [25]. Both the amorphous and crystal structures are confirmed by FFT patterns (Fig. 6b), and the local ordering has been further revealed by enlarged HRTEM image (Fig. 6c).

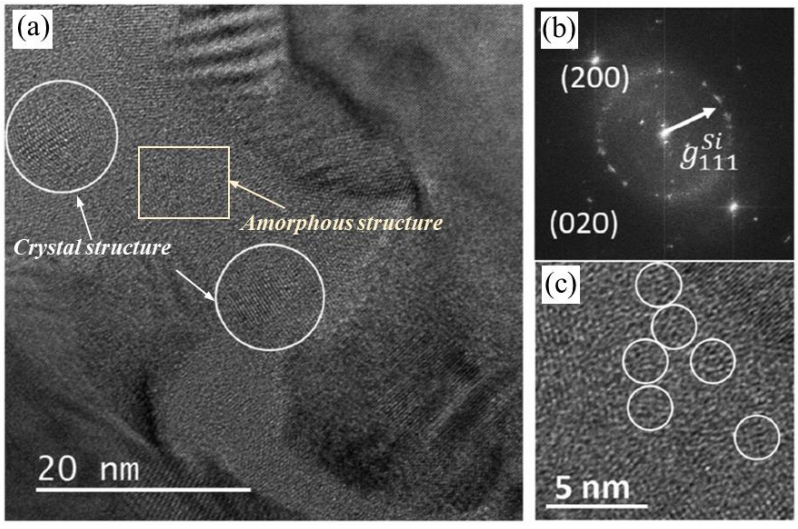

Fig. 6. TEM characterization of Si-rich eutectic showing the presence of both amorphous and crystal components [25]. HRTEM image of a eutectic zone surrounded by two Al cells oriented along a [001] zone axis, with the rectangle and circles pointing out the amorphous and crystal regions, respectively (a), FFT pattern of the whole image in (a) in which several spots consistent with the spatial frequency

of the (111) planes of diamond Si and the diffuse circle generated by the amorphous structure are present (b), enlarged HRTEM showing local ordering in the amorphous region (highlighted by the circles) confirming the presence of diamond Si (c). The figures are adapted with the permission from Elsevier.

It is noteworthy that the microstructure of the Si-rich eutectic presented in Fig. 6 corresponds to a build platform temperature of 35°C. Albu et al. [90] also reported an amorphous composition of the Si-rich eutectic in an as built sample with preheated build platform (150°C), suggesting that the amorphous nature of the Si-rich eutectic could be a common phenomenon in LPBF AlSi10Mg. This non-equilibrium state of as built microstructure was shown to begin to stabilize upon post-heating above 160°C, which drives crystallization of amorphous Si [90].

The Si-rich eutectic presents interconnected network morphology (cellular feature) at different cross-sections, according to 2D SEM micrographs [30]. Such unique cellular microstructure was frequently observed in LPBF metals, presumably involving Bernard Marangoni driven instability (BMI) and particle accumulated structure formation mechanism (PAS) with the help of strong thermal gradient, high grain growth rate, surface instability and solute transport due to surface tension effects [58]. With the use of FIB/SEM (Focused Ion Beam/Scanning Electron Microscopy) tomography, i.e., SEM 2D image being repeatedly acquired following serial FIB sectioning to obtain a SEM 3D volume with high resolution, the 3D morphology of the Si-rich eutectic was recently disclosed [26, 91]. Santos Macías et al. [26] showed the 3D microstructure of the melt pool core with a voxel size of 5 nm, as illustrated in Fig. 7. The branches of the network are found to be more plate than rod-shaped (see Fig. 7a and b). The perimeters of the Al cells are faceted instead of being perfectly round. In the FIB/SEM tomography, the Al cells could be described as elongated and tubular, generally presenting a much higher length than what was observed with 2D SEM imaging (see Fig. 7c).

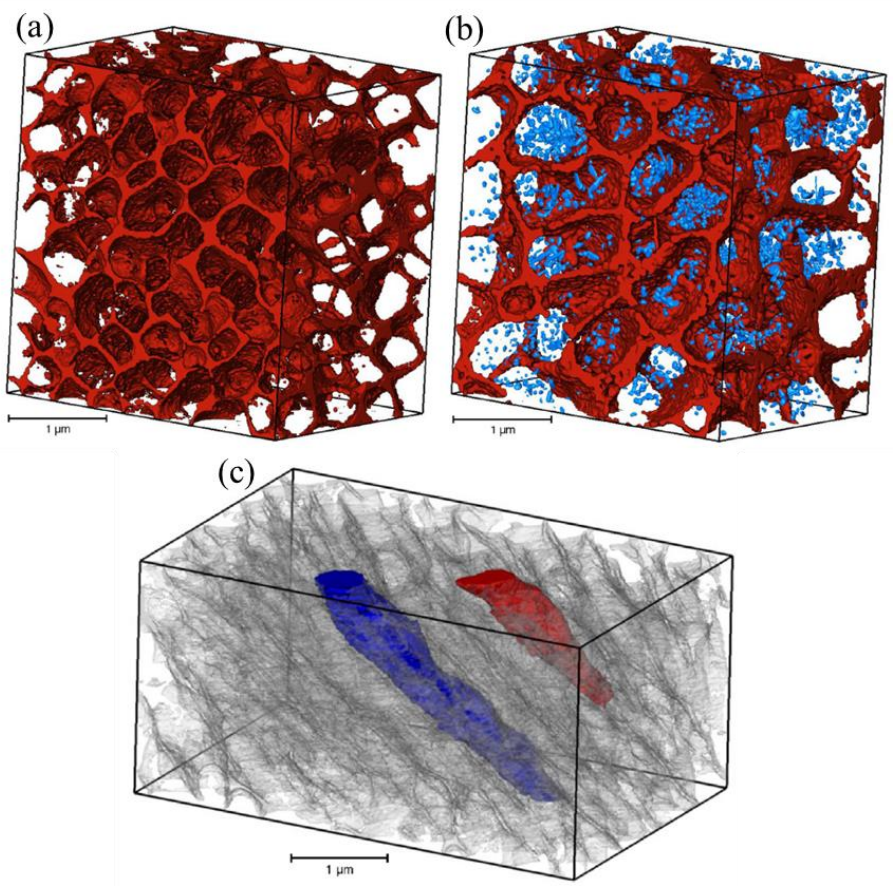

Fig. 7. FIB/SEM tomographies of the Si-rich eutectic of as built LPBF AlSi10Mg [26]. 3D rendering (3.5 × 3.4 × 2.5 µm) of melt pool core zone with building platform temperature of 35 °C (a) and 200 °C (b), visualization of two long tubular cellular structures exiting the reconstructed volume of the 35 °C material (c). The figures are reprinted with permission from Elsevier.

Thanks to the high resolution of the FIB/SEM tomography, even the Si-rich precipitates (60 nm) inside the Al matrix can be observed in preheated build platform material (200°C), as shown in Fig. 7b. The statistics of cellular structures and nanosized particles based on 3D data could be important for understanding or predicting the strength of LPBF AlSi10Mg. It is noteworthy that FIB/SEM appears to be an appropriate tool for resolving the fine microstructure of LPBF materials due to its balance between observation block size and resolution compared to other 3D techniques such as synchrotron X-ray tomography and APT.

2.1.4 Melt pools and grains

The melt pools and grains of LPBF AlSi10Mg can be regarded as structures at the same

scale (Fig. 8). The melt pool structures come from solidification of melted material induced by a moving heating source. They generally exhibit half-cylindrical shape characteristic of the conduction mode [29] usually used for manufacturing (see section 3.3). When looking at the melt pools on different cross-sections, a fish-scale (x-z and y-z planes in Fig. 8a) or an elliptical (x-y plane in Fig. 8a) morphology can be observed. Melt pool size is mainly controlled by layer thickness while melt pool structure arrangement is highly dependent on scan strategy [49].

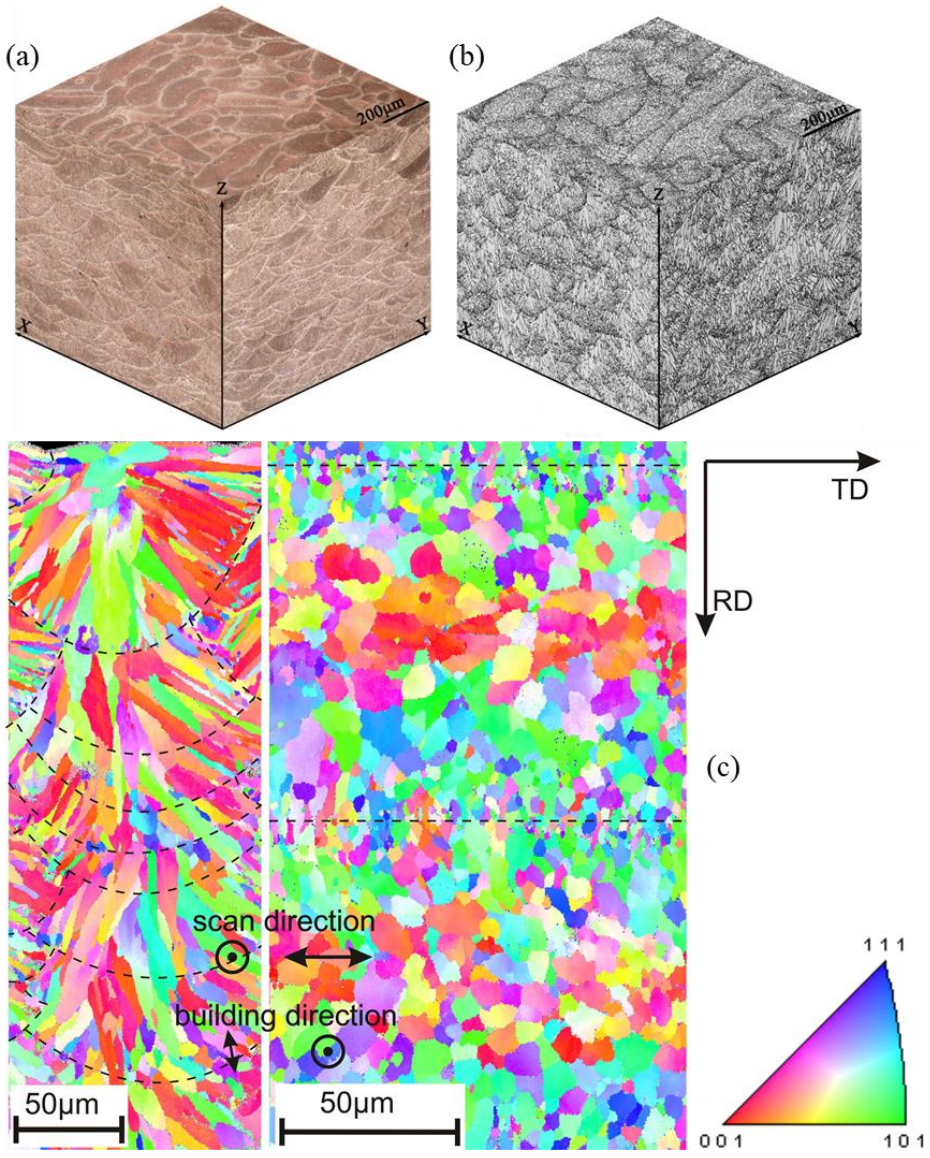

Fig. 8. 3D representation compiled from three orthogonal views manifesting the melt pool structures (a) and grain boundary distributions based on EBSD analysis (b) [92], typical grain morphology viewed at the sections parallel and perpendicular to the building direction (c) [30]. The figures are reprinted with permission from Elsevier.

In LPBF AlSi10Mg, the α-Al grains present directional growth in accordance with the heat flow direction. The latter typically drives the formation of columnar grain structures along the building direction inside the melt pools [30, 62, 82, 92], as can be seen in Fig. 8c. The elongated grains always grow normal to the melt pool border. Epitaxial growth (i.e., grains retain their crystallographic orientation across two or more melt pools) can be found at the centerline of the melt pool, while new grains nucleate and grow competitively away from the centerline. Only a few grains with specific orientations (<100> direction parallel to the thermal gradient direction according to Thijs et al. [30] and <001> orientation parallel to the scanning direction according to Liu et al. [82]) can grow further toward the melt pool interior, whereas the others remain small and equiaxed at the melt pool border. The grain size is generally one order of magnitude higher than that of the α-Al cell (or cellular Si-rich eutectic structure), in both building and transverse directions. Therefore, grain boundary strengthening can generally be neglected in the prediction of material strength [26].

Regarding the grain orientation distribution, a <100> fiber texture in the building direction was mostly reported in previous works [26, 30, 49, 62, 92, 93]. In fact, this specific texture is consistent with the epitaxial grain growth at the melt pool centerlines, where the heat flow is directed favorably to the <100> direction of previously solidified grains [30]. In contrast, for newly nucleated and grown columnar grains from the melt pool borders, only the grain directions between <110> and <111> tend to align with the building direction, as revealed by experimental characterization [26, 30, 62]. Moreover, the small and equiaxed grains at the melt pool borders mostly exhibit random orientations [26, 30, 82], in line with their growth kinetics. Although the texture feature strongly depends on the scanning strategy, as quantitatively assessed by Liu and To [94], the columnar grain morphology and <100> fiber texture are the most typical features of the LPBF AlSi10Mg mesostructure.

2.2 Heterogeneous aspect

Due to the layer-by-layer build strategy of the LPBF process, previously melted and solidified layer will be partially remelted when scanning the current layer, leading to a complex thermal history for the melt pool structure. Consequently, three zones can be differentiated according to the morphology and size of the Si-rich eutectic regardless of observation planes (cross-sections)[30, 82]: (i) Fine zone, also referred to as fine melt pool (FMP) zone, which occupies the majority of the whole melt pool. The Si-rich eutectic in the FMP exhibits the interconnected cellular shape that is directed normal to the melt pool border, consistent with the columnar grains present in this zone. (ii) Coarse zone, also referred to as coarse melt pool (CMP) zone, in which the Si-rich eutectic still remains interconnected and the α-Al grains present equiaxed shapes. The Si-rich network in the CMP is larger and thicker than that in the FMP. (iii) Heat affected zone (HAZ), where the interconnection of the Si network is significantly degraded. The CMP and HAZ constitute the melt pool border, the thickness of the CMP generally being larger than that of the HAZ [26].

According to Liu et al. [82], the three distinct zones correspond to three temperature regions during the heating of the current powder layer, see Fig. 9. In the region where the temperature is higher than the liquidus temperature, the powder and overlapped material are melted and then solidify into columnar α-Al grains and Si-rich eutectic cellular-dendrites, forming the FMP structure. In the region where the temperature is lower than the liquidus temperature but higher than the solidus temperature, the previously solidified material is reheated to semi-solid state, in which the α-Al phase changes to globular morphology and the Si-rich network is coarsened, forming the CMP structure. In the region where the temperature is lower than the solidus temperature, the heat source acts as a heat treatment for the previously solidified material and drives the globulization of the Si-rich network, therefore forming the HAZ structure.

The microstructure heterogeneity throughout the melt pools could also be explained by non-

steady solidification behavior. As revealed in several numerical studies [95, 96] (not for LPBF AlSi10Mg, but the trend should be common), the growth rate (R) is lower and the thermal gradient (G) is higher at the melt pool border during solidification, whereas R becomes higher and G becomes lower in the melt pool interior. Such behavior will lead to distinct solidification structure morphologies between internal and peripheral melt pool regions [97]. Moreover, Li et al. [80] showed, based on numerical heat transfer model, that the cooling rate inside the melt pool is also higher than that at the melt pool border, thus leading to a finer solidification structure in the melt pool interior of LPBF AlSi10Mg.

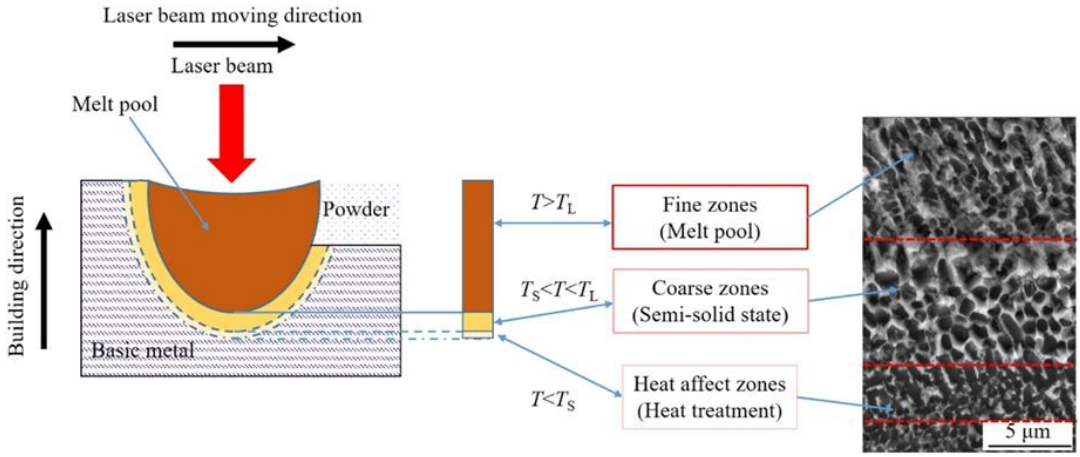

Fig. 9. Schematic diagram for the formation of three zones observed in LPBF AlSi10Mg [82]. T_L is the liquidus temperature, T_S is the solidus temperature. The figures are reprinted with permission from Elsevier.

Three-dimensional characterization of the three zones via FIB/SEM tomography was recently performed by Santos Macías et al. [26] and Zhao et al. [47], with a focus on the connectivity of the Si-rich network. Note that the connectivity mentioned in their works was defined as the volume fraction of the largest object of one phase with respect to the total volume fraction of that phase in the analyzed volume.

In fact, the connectivity evaluation depends on the analysis strategy. When assessing FMP, CMP and HAZ in separate volumes (see Fig. 10a-c), the connectivity was found to be 0.99, 0.85 and 0.1, respectively, suggesting a significant collapse of the network feature in the HAZ

[26]. Nevertheless, when a volume across the melt pool border was analyzed (see Fig. 10d and e), Zhao et al. [47] showed that the Si-rich eutectic of the three zones was well interconnected (Fig. 10d). Even if a smaller volume (Fig. 10e), being a subvolume of that of Fig. 10d, was taken, the HAZ could not be recognized as clearly as in 2D SEM images. The Si-rich eutectic of the HAZ was found to be part of the Si-rich network of the FMP. Zhao et al. [47] attributed the deviation between 2D and 3D characterizations to the specific branched morphology of the Si-rich eutectic in the HAZ (see Fig. 10f and g). The branched Si-rich eutectic can manifest as separate particles in 2D micrographs, whereas the real structure retains a much higher connectivity in space. It should be noted that the connectivity of the Si-rich eutectic in the heterogeneous microstructure of LPBF AlSi10Mg is important to understand the deformation and damage mechanisms, as will be reviewed in section 4.

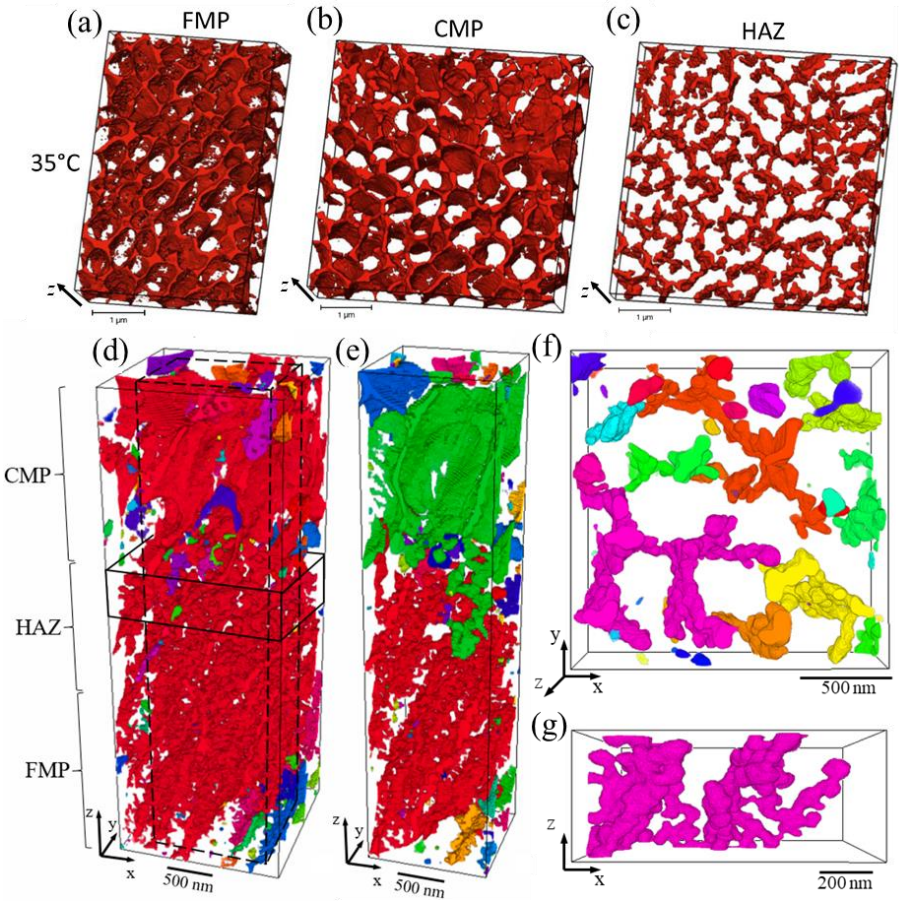

Fig. 10. FIB/SEM tomographies for the three distinct zones in an LPBF AlSi10Mg sample built with 35°C build platform (the z axis corresponds to the building direction). Si-rich eutectic network of

separate FMP (a), CMP (b) and HAZ (c), 3D rendering of Si-rich eutectic across the melt pool border (d) and a subvolume of (d) (e), local 3D views of HAZ along the building (f) and transverse (g) directions. The figures are reprinted from [26] and [47] with permission from Elsevier.

2.3 Hierarchical aspect

Section 2.1 depicts the microstructure of as built LPBF AlSi10Mg mainly from the scale viewpoint. When assessing the microstructure in terms of structure periodicity, two hierarchies can be defined, namely melt pool hierarchy and Al cell hierarchy (see the schematic drawing in Fig. 11). In fact, hierarchical microstructure is quite common among additively manufactured metals as many of them contain cellular structures composed of either secondary phase [73, 98] or dislocation networks [99, 100].

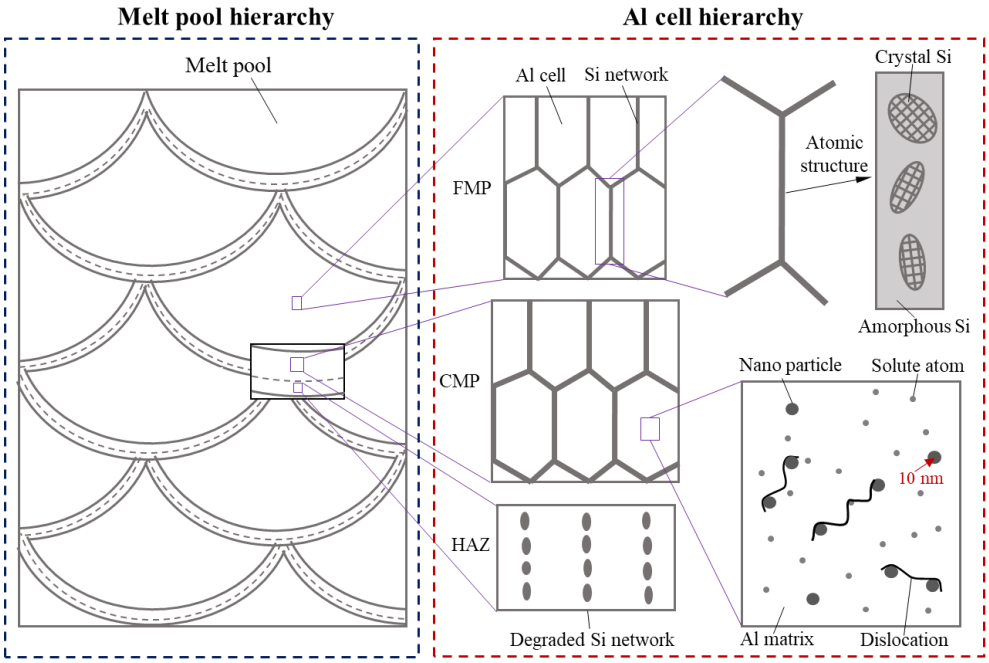

Fig. 11. Schematic illustration of the hierarchical character of the LPBF AlSi10Mg microstructure.

At the melt pool hierarchy, the structure features Al grains and Si-rich eutectic both in the melt pool interior and at the melt pool border. The variation of the structure lies on the grain shape and orientation as well as the morphology of the cellular Si-rich network. At the Al cell hierarchy, the structure features Si/Al interface, nanosized particles and solid solution in a single Al cell. The variation of the structure lies on the continuity of the interface (i.e., connectivity of

the Si-rich network) and the distribution of the nanosized particles and solute atoms.

The definition of hierarchy is important to treat the trans-scale structure of LPBF AlSi10Mg in modeling or simulation of mechanical response. First, the submicron microstructural information can be considered in modeling at the Al cell hierarchy. Then, the behavior of an aggregate of Al cells can be transferred to the melt pool hierarchy for up-scaled modeling. In this way, the understanding or prediction of correlation between mechanical performance and microstructure can be achieved. This point will be further discussed in section 7.2.

2.4 Effect of LPBF strategy on microstructure

The LPBF strategy plays a vital role on the microstructure of AlSi10Mg. The strategy review in this section incorporates not only laser parameters, but also build platform temperature and scan strategy. It should be noted that LPBF machines may also present an influence on built part quality, due to the difference in the inert gas used in the chamber, the way laser is delivered and the possibility and temperature limit of build platform preheating [76, 101, 102]. As the optimum processing conditions and parameters vary from one machine manufacturer to another, it is difficult to perform a direct comparison. Therefore, detailed discussion of this factor is out of the scope of the present review.

The morphology and fineness of LPBF microstructure are closely related to the thermal gradient G and the solidification (or growth) rate R, which highly depend on laser parameters [78]. The cooling rate, denoted as $G*R$, determines the size of the solidification structure, while the G/R ratio determines the stability of the solidification and hence the solidification mode, i.e., the morphology of the solidifying front. As shown in Fig. 12, solidification structures can be planar, cellular, columnar dendritic or equiaxed dendritic with decreasing G/R values. On the other hand, the dimension of solidification structures decreases when increasing cooling rate ($G*R$). The thermal gradient G can be influenced by many factors, a basic trend is that a higher linear heat input (laser power over scan speed) results in larger melt pools and

consequently lower thermal gradients [78]. The growth rate R depends on the speed of the moving source v and the angle between the direction of the moving source and the growth direction of the solidifying material φ. R is equal to v*cosφ assuming steady state conditions [103].

The cooling rate ($\dot{T}$) can be estimated using a one-dimensional Rosenthal equation [104], given by

$$\dot{T} = 2\pi k(T_{\text{solidus}} - T_0)(T_{\text{liquidus}} - T_0)\frac{v}{Q} \tag{1}$$

where k is the thermal conductivity, T_{solidus} and T_{liquidus} the solidus and liquidus temperatures, respectively, T_0 the build platform temperature, v the laser scan speed and Q the heat transferred from laser into powder which equals to βP (β is the laser absorption coefficient, P is the laser power).

Other two important laser parameters are volumetric (*VED*) and linear energy density (*LED*), defined as

$$VED = \frac{P}{vht} \tag{2}$$

$$LED = \frac{P}{v} \tag{3}$$

where h is the hatch spacing and t the layer thickness.

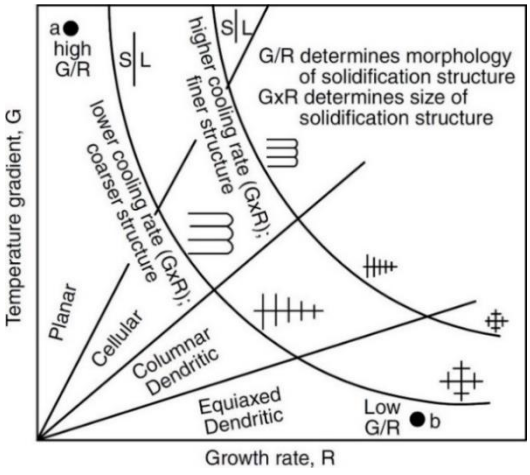

Fig. 12. Effect of temperature gradient G and growth rate R on the morphology and fineness of the

solidification structure [78]. The figure is reprinted with permission from Elsevier.

From the literature reports, it can be seen that as built LPBF AlSi10Mg always exhibits columnar grains and an interconnected Si-rich eutectic network. These microstructure features are induced by a high cooling rate and a moderate temperature gradient such that the solidification mode of LPBF AlSi10Mg lies at the boundary between the columnar dendritic and equiaxed dendritic regimes, i.e., low to moderate G/R.

Giovagnoli et al. [36] and Scipioni Bertoli et al. [105] demonstrated that the volumetric laser energy density cannot be used as the indicator of microstructure morphology and fineness as the same density can have different combinations of laser power, scan speed, hatch spacing and layer thickness, each of the four parameters potentially inducing an impact in itself. Paul et al. [49] studied the effect of hatch spacing and layer thickness while keeping the volumetric laser energy density constant. They revealed that increasing hatch spacing and layer thickness resulted in larger columnar grains with a wider Si-rich network. However, the microstructure fineness cannot be directly linked to hatch spacing and layer thickness from this work since both laser power and scan speed were varied to ensure a constant energy density. In fact, Thijs et al. [30] demonstrated that hatch spacing and layer thickness mainly affected crystal texture, a smaller hatch spacing or layer thickness leading to a higher amount of partial remelting of neighboring tracks and therefore generating a stronger <100> texture.

Liu et al. [68] fixed the hatch spacing and layer thickness and investigated the influences of laser power and scan speed on the microstructure. Typical trends revealed in that work are: a higher laser power or a lower scan speed leads to a coarser Si-rich network. Liu et al. [82] also showed that a higher laser power would promote larger mean grain size. These trends can be related to the cooling rate (Eq. 1), which increases and decreases with the increase of scan speed and laser power, respectively. Tang et al. [106] and Hyer et al. [107] showed a close correlation between Al cell size and cooling rate, a higher cooling rate leading to a finer cell structure (see

Fig. 13). It is noteworthy that although the data points in Fig. 13e are extracted from different studies involving different process parameters, the microstructure fineness-cooling rate correlation is qualitatively or even quantitatively consistent. This confirms that cooling rate can be regarded as the indicator of Al cell size of LPBF AlSi10Mg.

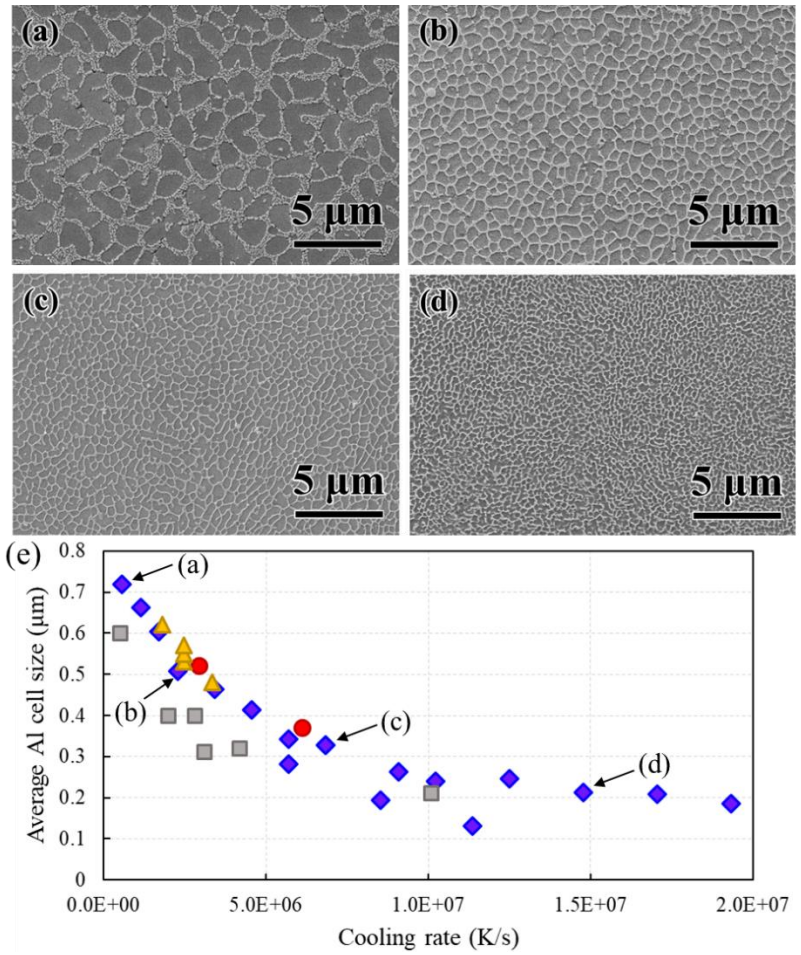

Fig. 13. Effect of cooling rate on Al cell size. SEM micrographs of Al cell structures [107] with a scan speed of 100 mm/s (a), 400 mm/s (b), 1200 mm/s (c) and 2600 mm/s (d) at fixed laser power (250 W), layer thickness (30 µm), hatch spacing (0.13 mm) and build platform temperature (100°C), relationship between average Al cell size and cooling rate calculated with Eq. 1 at fixed layer thickness and hatch spacing (e). The symbols of diamond, square, circle and triangle represent data from Refs [107], [106], [26] and [68], respectively. The corresponding cooling rates for (a)-(d) are marked in (e). The figures are reproduced with permission from Springer Nature.

However, when analyzing Si-rich particles within Al cells, their appearance, shape and size do not seem to depend on laser energy density nor cooling rate, as revealed by the comparison

between materials in different studies incorporating different laser parameters and build platform temperatures (see Table 1). For example, the Si-rich particles observed in [86] are much larger than that revealed in [26], despite a much higher cooling rate (Table 1). This contradicts the microstructure fineness-cooling rate correlation. There are also some studies where the authors performed TEM characterization but found no particles within Al cells with either non-preheated or preheated build platform, as presented in the last two rows of Table 1. In fact, the cooling rate mainly determines the solid solution content in the Al matrix upon solidification, whereas the precipitation behavior is expected to be more closely related to the thermal history after solidification, i.e., the solid state thermal cycling from subsequent tracks/layers. It is difficult to determine, based only on the process parameters, the exact thermal history the solidified microstructure will experience and whether it is appropriate to trigger the precipitation phenomenon [86].

Table 1. Nanosized Si-rich particles within Al cells of as built LPBF AlSi10Mg. The cooling rate is estimated using Eq.1 with a laser absorption coefficient of 0.35 [107], the energy density is estimated using Eq. 2.

Laser power (W)	Scan speed (mm/s)	Layer thickness (μm)	Hatch spacing (μm)	Platform temperature (°C)	Energy density (J/mm^3)	Cooling rate ($\times 10^6$ K/s)	Particle shape	Particle size (nm)	Ref.
370	1300	30	190	35	49.9	2.8	Sphere	Equiv. Φ: 5	[87]
390	1300	30	190	35	52.6	2.6	Sphere	Equiv. Φ: 12	[27]
275	2000	30	80	35	57.3	5.7	Ellipsoid or plate; Needle	Equiv. Φ: up to 30; Width: 25 Length: up to 300	[86]
275	500	50	120	-	91.7	-	Sphere	Equiv. Φ: 10	[29]
400	1300	30	190	-	54.0	-	Needle	Width: 10 Length: up to 300	[89]
350	930	50	170	150	44.3	1.3	Sphere	Equiv. Φ:20	[88]
390	1300	30	190	200	52.6	1.3	Needle	Equiv. Φ: 60	[26]
370	1300	30	190	200	49.9	1.3	Needle	Equiv. Φ: 61-65	[42]
380	1000	30	-	25	-	2.1	Sphere (nature not identified)	Equiv. Φ: 15	[41]
370	1500	30	105	25	78.3	3.3	Not found	Not found	[44]
350	1150	50	170	150	35.8	1.6	Not found	Not found	[90]

Another important factor highly influencing microstructure is build platform temperature. This factor can alter cooling rate (see Eq. 1) and thermal gradient during printing [108, 109], thus leading to microstructural changes. A wide range of build platform temperatures have been tried in literature, from 35°C to 300°C [26, 46, 55, 88, 91, 93, 110-120]. The common trend is that the Si-rich eutectic always manifests as an interconnected network, whereas the microstructure fineness varies with the temperature level. Santos Macías et al. [26] showed that increasing build platform temperature (from 35°C to 200°C maintaining the rest process parameters) could coarsen the microstructure from the following three aspects: first, both the CMP and HAZ regions become larger, as can be clearly seen in Fig. 14a and b; second, the Si-rich eutectic network is coarser in terms of equivalent diameter and wall thickness (see Fig. 14c and d); third, the Si-rich particles inside the Al cells are larger (see Fig. 14e and f). Nevertheless, the grain size and morphology were found to be little affected by build platform temperature. Similar observations were reported by Casati et al. [115] comparing build platform temperatures of 25°C and 160°C. It is noteworthy that if a higher build platform temperature was used, the microstructure could be further significantly coarsened. Recently, Bian et al. [121] succeeded in printing AlSi10Mg using electron beam melting (EBM). Note that the EBM process involves systematic powder bed preheating. With a preheating temperature of 430-470°C, it was found that the as built EBM AlSi10Mg sample exhibited only large dispersed Si-rich particles (approximately 2 μm) [121].

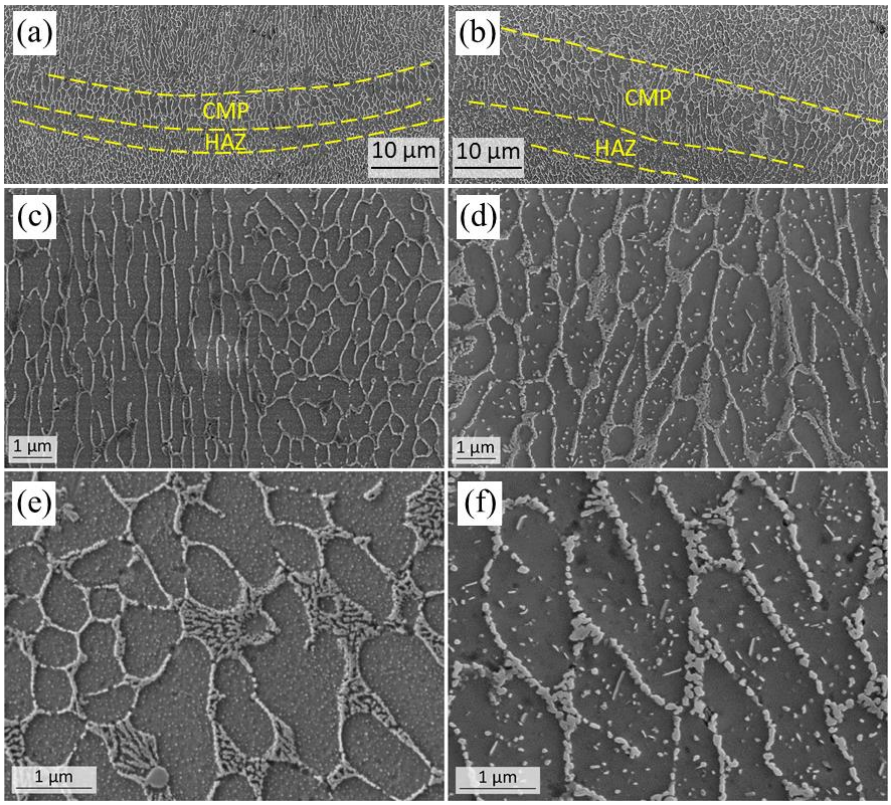

Fig. 14. Influence of build platform temperature on microstructure of LPBF AlSi10Mg [26]. Melt pool border (a), Si-rich network (c) and nanosized particles (e) in 35°C case, melt pool border (b), Si-rich network (d) and nanosized particles (f) in 200°C case. The figures are reproduced with permission from Elsevier

In addition to coarsening of Si-rich eutectic and nanoparticles, build platform preheating can also lead to in situ aging effect, reducing Si solute concentration (i.e., causing Si precipitation) and forming Mg_2Si precipitates within Al cells. Van Cauwenbergh et al. [81] showed that a 200°C preheating could reduce the Si concentration from 2.7 wt.% (without preheating) to 0.5 wt.%. Hadadzadeh et al. [83] demonstrated the presence of Mg_2Si precipitates in as built LPBF AlSi10Mg manufactured with a build platform temperature of 200°C. Such in situ precipitation however just slightly contributes to strengthening (around 13 MPa [83]) due to its low content, given a significant enrichment of Mg in the eutectic network [81]. It is noteworthy that no systematic studies have been devoted to identify the critical build platform temperature at which Mg_2Si precipitate starts to form.

The scan strategy can also induce a high impact on microstructure, mainly in the aspects of grain orientation and melt pool arrangement (i.e., at the melt pool hierarchy). Thijs et al. [30] studied the influence of the scan strategy on the crystallographic texture. They showed that a strong partial <100> fiber texture along the scanning direction was present when no rotation of scanning direction in the layer (i.e., islands) or between layers was applied. In contrast, when a 90° rotation was employed, a weak <100> cube texture along the building direction was formed. This indicates that the texture of LPBF AlSi10Mg can be controlled by rotations of scanning vectors. Paul et al. [49] demonstrated that the scan strategy could also control the melt pool arrangement, based on the comparison between 67° and 90° rotations. The 67° rotation case shows a similar melt pool morphology for any side view (i.e., sections parallel to the building direction), whereas the 90° rotation leads to a quite variable morphology.

2.5 Effect of post-printing heat treatments

Various post-printing heat treatments have been applied to mitigate residual stresses and enhance mechanical properties of LPBF AlSi10Mg, namely annealing (or stress relief heat treatment), T6 treatment and direct aging. Post-printing heat treatments result in distinct microstructure changes in function of temperature, as schematically shown in Fig. 15. According to an in situ heating test performed in TEM [90], the Si-rich eutectic remains nearly unchanged below 160°C, while it starts to coarsen and slightly globularize when the temperature is higher than 200°C. The network feature is still well retained at 260°C, whereas a full breakdown of the network occurs at 300°C.

Fiocchi et al. [122] and Zhao et al. [27] confirmed that a heat treatment at 263°C and 250°C retained the Si-rich eutectic network in bulk LPBF AlSi10Mg samples. Given that the network feature limits material ductility [27], stress relief heat treatment (SRHT) is generally performed at a temperature around 300°C [61-63, 81, 111, 114, 116, 123, 124], aiming to mitigate residual stresses [63] and increase ductility (a fourfold increase in true strain at fracture [61]). SRHT

microstructure typically presents a globular Si phase, which comes from the collapsed network (relatively large) and the growth of initial or precipitated nano-sized Si particles (relatively small) [27], therefore presenting a bimodal size distribution. After SRHT, Si solution content in Al cells drops to a low level of roughly 0.3 wt.% [27, 81]. Moreover, SRHT does not change grain size and orientation, as demonstrated by Takata et al. [62].

To fully homogenize the microstructure of LPBF AlSi10Mg while avoiding a significant drop of mechanical strength, T6 treatment (solution treatment at roughly 500°C and artificial aging at about 160°C) has also been widely investigated in literature [64, 112, 116, 123-125]. It globularizes and markedly coarsens the Si-rich eutectic during solution treatment, and then drives precipitation during artificial aging. The precipitate nature and distribution has been thoroughly analyzed by Zhou et al. [89]. They showed the existence of GP zones, β'' and Mg_2Si phases after T6 heat treatment. It should be noted that the high temperature applied during solution treatment also leads to a slight grain growth [62], in contrast to stress relief heat treatment.

Taking advantage of the supersaturated Si solution in Al cells with no or moderate build platform preheating, direct aging of as built LPBF AlSi10Mg has also been widely adopted in recent investigations [87, 115, 126-129], aiming to form fine precipitates and enhance mechanical strength. Such heat treatment is generally performed at a temperature below 200°C and does not influence the Si-rich network structure noticeably. Zhang et al. [128] compared the effects of direct aging at 130°C, 150°C, 170°C and 190°C, showing Si precipitation and its growth with temperature increase.

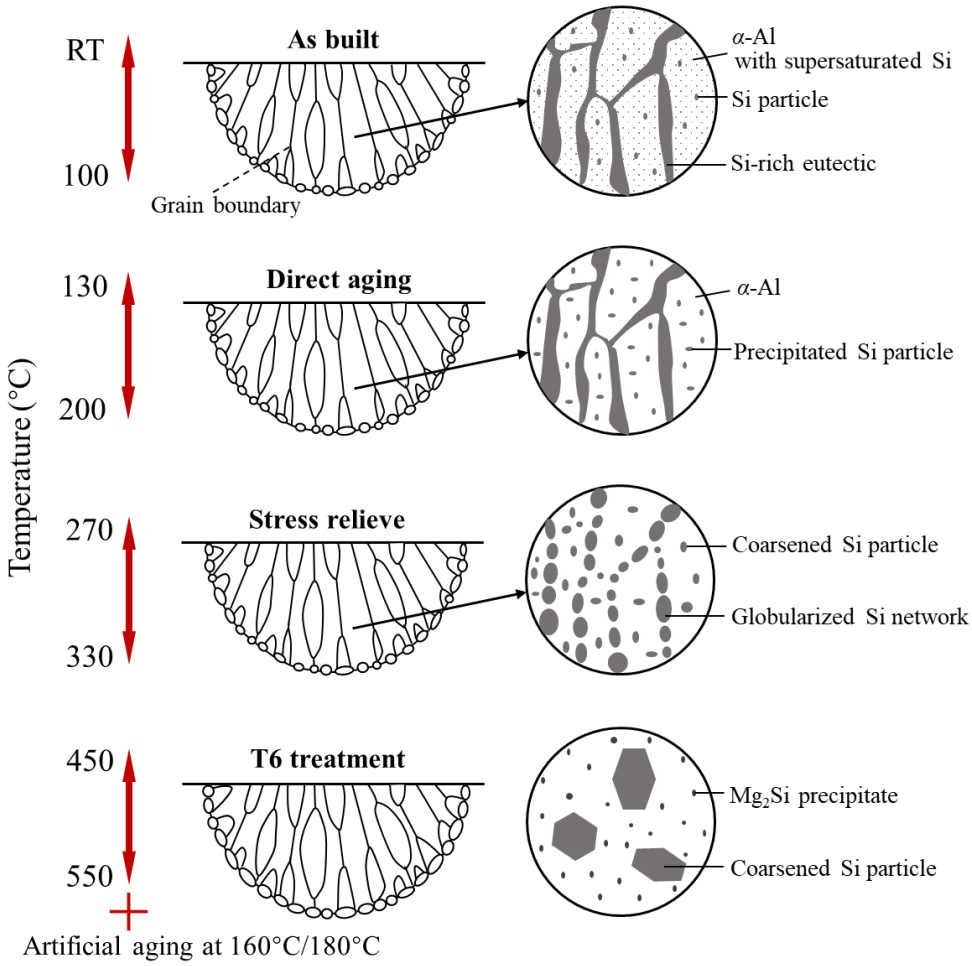

Fig. 15. Influence of post-printing heat treatment on microstructure of LPBF AlSi10Mg. This schematic drawing is modified from [62].

From the aforementioned studies, it can be concluded that the effect of post-printing heat treatment on microstructure shares some similarities but also shows differences compared to that of build platform preheating. On the one hand, both post-printing heat treatment and build platform preheating coarsen the microstructure of LPBF AlSi10Mg. On the other hand, build platform preheating always retains (even at 300°C) the interconnected nature of the Si-rich eutectic, whereas a post-printing heat treatment at or above 300°C leads to a network collapse. This implies that the thermal history experienced by solidified microstructure during printing with preheated build platform is significantly different from that during post-printing heat treatment. The effect of post-printing heat treatment on mechanical properties will be discussed in section 4.1.

3. Porosity

Porosity has been recognized as an intrinsic drawback of the LPBF process that involves very complex laser-powder-melt pool interdependency dynamics, as revealed by both multiphysical simulations [60] and experimental observations [130, 131].

Fig. 16 illustrates examples of powder vaporization, powder spattering as well as the interaction between spatter and laser rays, which are the fundamental triggers for pore formation regardless of the scanning strategy. As the high energy of the laser beam quickly boils and vaporizes metallic powder (see Fig. 16d), the entrained gas flow then generates powder spattering (see Fig. 16a-d). Khairallah et al. [60] further studied the laser rays' interaction with the spatter using a multiphysics model to understand the pore formation. They revealed that a high laser power could generate large impulse force which expulsed gas-entrained spatter away from the laser path (see Fig. 16e), without creating lack of fusion defects. In contrast, when using low laser power, the gas-entrained spatter could be pressed down into the melt pool, highly decreasing the melt pool depth, distorting the track direction and creating a large discontinuity, finally resulting in lack of fusion defects (see Fig. 16f). Particularly, in the case of an excessive energy input, a vapor depression could take place, strongly disturbing the melt pool shape and generating a keyhole defect (see Fig. 16g-j) [132]. For further summarization of porosity and its formation conditions, readers can refer to a recent review paper by Sanaei and Fatemi [133].

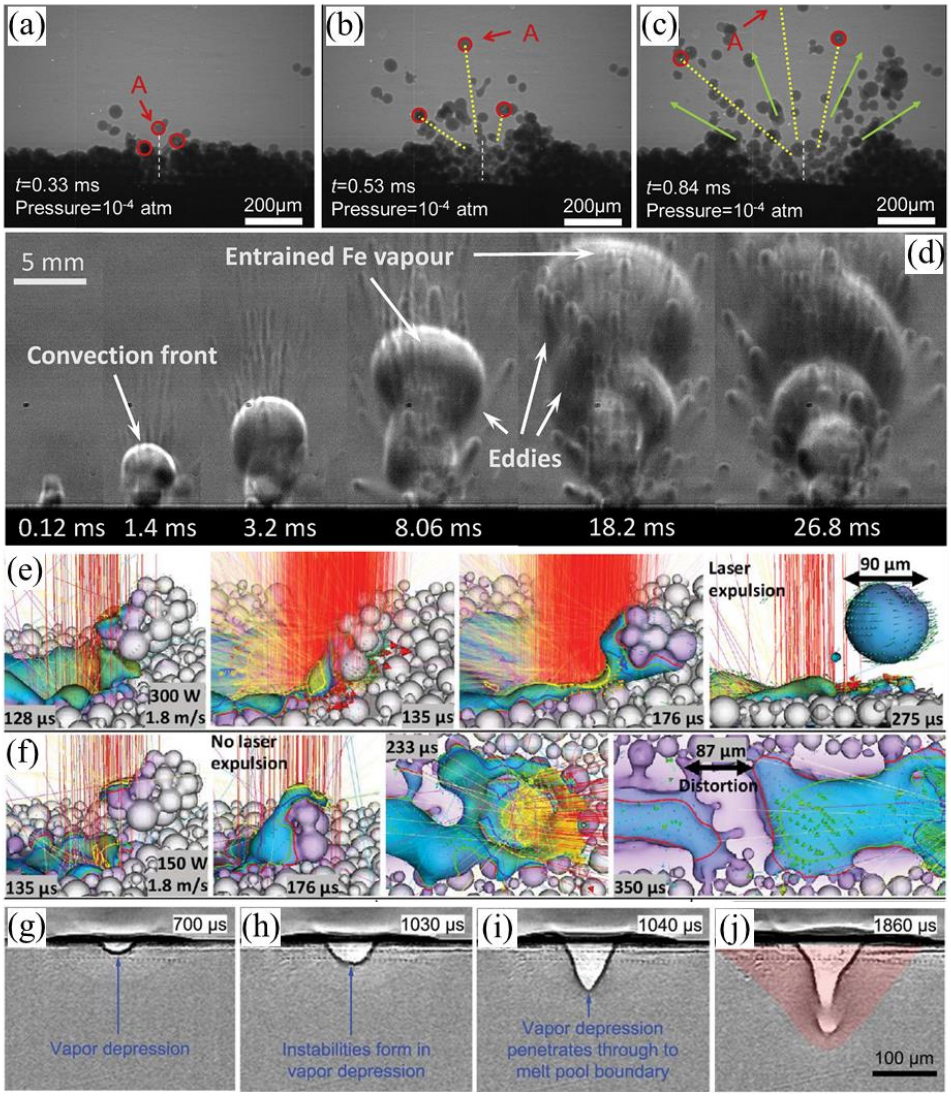

Fig. 16. Dynamic X-ray images showing powder motion at different moments [130] (a)-(c), schlieren high-speed images showing the motion of metallic vapor gas at different moments [131] (d), simulated melt pool dynamics due to laser expulsion of spatter (e) and head-on collision between spatter and melt pool (f) [60], ultrahigh-speed X-ray imaging revealed keyhole depression and instability at high energy density [132] (g)-(j). The figures are reprinted with permission from Elsevier, Springer Nature and AAAS.

As for LPBF AlSi10Mg, the common pore defects can be categorized into gas pores, lack of fusion pores and keyholes, exhibiting either spherical or irregular shapes (Fig. 17a). A general tendency of pore size and geometry found for LPBF AlSi10Mg is that decreasing size is generally accompanied by increasing sphericity [32, 34, 88]. With the use of X-ray computed

tomography, porosity in LPBF AlSi10Mg has been comprehensively assessed in recent years. Typical examples of porosity are given in Fig. 17b-e, as will be reviewed in the following subsections.

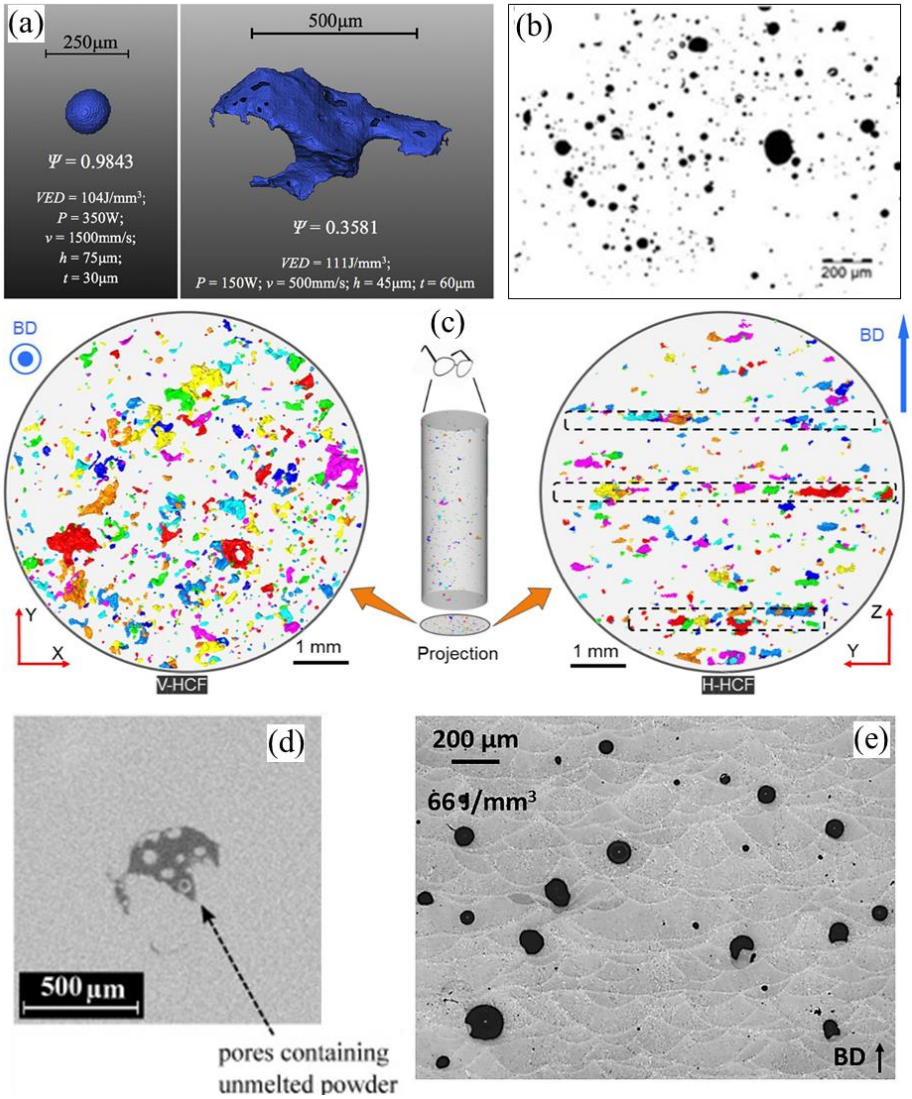

Fig. 17. Typical porosity present in LPBF AlSi10Mg. Spherical and irregular shaped pores [32] (a), hydrogen gas pores [33] (b), lack of fusion pores viewed at different projection planes [34] (c), pore formation due to unmelted powder [35] (d), keyhole porosity [36] (e). The figures are reprinted with permission from Elsevier.

3.1 Gas pores

Gas porosity is formed by either initially entrapped gas in the metal powder or the gas atmosphere of the LPBF machine [88, 134]. Gas pores generally present spherical shape and

small size (see Fig. 17b). Weingarten et al. [33] investigated hydrogen porosity resulting from moisture at the powder surface and dissolved hydrogen inside the powder. Physically, the nucleation of hydrogen pores takes place upon the local hydrogen concentration is higher than the maximum solubility in liquid aluminum. The growth of hydrogen pores is in itself a diffusion controlled process and is driven by hydrogen supply over the gaseous liquid interface of the pores. As the diffusion rate of hydrogen in the melt is much higher than that in the solid, the growth is therefore stopped when the pore is captured by the solidification front. In this sense, the time gap between the melting and the solidification (t_M), which can be influenced e.g. by the scan speed, is a significant parameter determining hydrogen porosity size and density. Apparently, a small t_M is required to reduce the pore density.

On the other hand, the solubility of hydrogen in liquid Al (0.7 mL/100g, [135]) is tenfold higher than that in solid Al, a hydrogen enrichment therefore occurs at the solidification front. When the material solidifies in a very short time period due to the intrinsic fast cooling rate of the LPBF process, the supersaturated hydrogen is trapped in the lattice of the solid phase, generating a metastable state. Note that this metastable state can promote pore enlargement or additional pore formation during post-heat treatments [136]. Naturally, a low hydrogen porosity could be obtained via a powder drying process, as demonstrated by Weingarten et al. [33] and Yang et al. [136].

3.2 Lack of fusion pores

Lack of fusion porosity is formed mainly due to insufficient energy density [136] and poor overlap of melt pools (scan tracks) [137]. Fine powder size could also increase the lack of fusion defects due to lower flowability and packing density [37, 138]. Lack of fusion pores typically present irregular shapes, as shown in Fig. 17c, in which unmelted powder particles are eventually embedded (see Fig. 17d). Unlike the gas pores, lack of fusion pores exhibit preferred orientations (see Fig. 17c). Their long axis is aligned either perpendicular (horizontally) or

parallel (vertically) to the building direction. Horizontally aligned defects are considered to result from insufficient energy density leading to poor fusion with the previous layer. They normally appear at layer-layer boundaries. Vertically aligned defects are considered to result from insufficient overlap between scan tracks due to a large hatch distance. They normally appear at track-track boundaries. Horizontally orientated lack of fusion pores, reported more frequently in literature [32, 35, 88], are considered responsible for anisotropic mechanical performance [34, 88], as will be reviewed in section 6.1.

3.3 Keyhole pores

Keyhole pores can be regarded as specific gas pores which are generally formed at high volumetric laser energy density. They normally present a spherical shape (see Fig. 17e). An excess of laser energy input can lead to metal vaporization and recoil pressure, which drive the melt pool surface deep into the material to form a vapor depression (i.e., keyhole). When such depression becomes unstable, it easily collapses, trapping inert shielding gas and forming pores located at the bottom of the melt pool. The formation process and dynamics of vapor depressions were nicely captured by in situ ultrahigh-speed X-ray imaging [132] and multiphysics simulations [139]. Readers can refer to these two publications for more details.

In addition to keyhole pore formation, high energy densities could also lead to a transition of melt pool morphology from shallow and semicircular (in what is known as conduction mode) to deep and narrow (keyhole mode) shape. It should be noted that the keyhole mode can be stable or unstable. Stable keyhole mode may even improve strength and ductility of LPBF metals [140], whereas unstable keyhole mode (usually at a higher energy input) generates detrimental pores due to keyhole collapse [141, 142]. Cunningham et al. [132] demonstrated that there exists a well-defined threshold from conduction mode to keyhole mode based on laser power density. Performing a systematic study, Wu et al. [29] identified the energy density ranges for different modes of LPBF AlSi10Mg (see Fig. 18), i.e., conduction mode (<50 J/mm^3),

transitional mode (~50–65 J/mm^3), and keyhole mode (>65 J/mm^3). The transition mode corresponds to cases where both shallow melt pools and keyhole-induced deep mode melt pools exist. It can be seen that the keyhole mode is normally associated with a low density. Moreover, the porosity level was found to increase with the increase of power density, as illustrated in Fig. 18. A similar trend was also reported by Giovagnoli et al. [36].

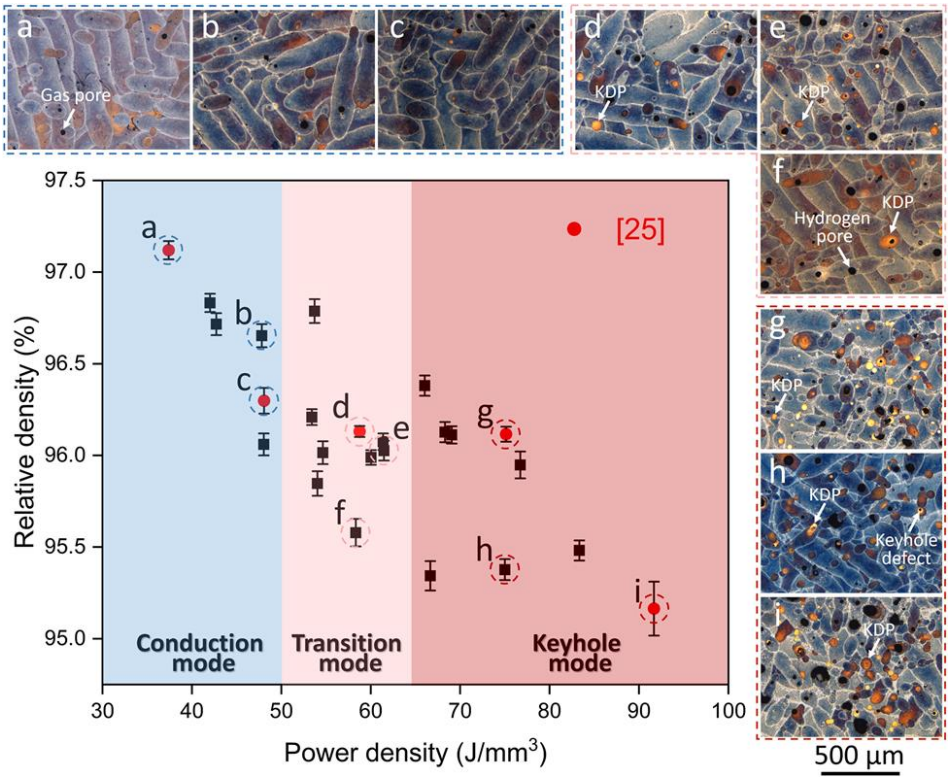

Fig. 18. Relationship between volumetric energy density and relative density of LPBF AlSi10Mg specimens [29]. The top-view images of the specimens labelled on the graph show the corresponding porosity defects. KDP denotes keyhole induced deep melt pool. The Ref. [25] in the plot is cited as [143] in the present paper. The figures are reprinted with permission from Elsevier.

The porosity level has been significantly mitigated with the advancement of the LPBF technique and with process parameter optimization [36, 68, 144]. Fig. 19 shows an example of porosity in LPBF AlSi10Mg fabricated with the machine (EOS M290) manufacturer suggested parameters [38]. According to statistics based on X-ray computed tomography with a voxel size of 1.6 µm, the porosity level was lower than 0.1%, and the detected maximum pore size was smaller than 100 µm, both showing a slight decrease when preheating the platform to 200°C

(see Fig. 19b and c). Most interestingly, the very large pores were removed with the 200°C preheating.

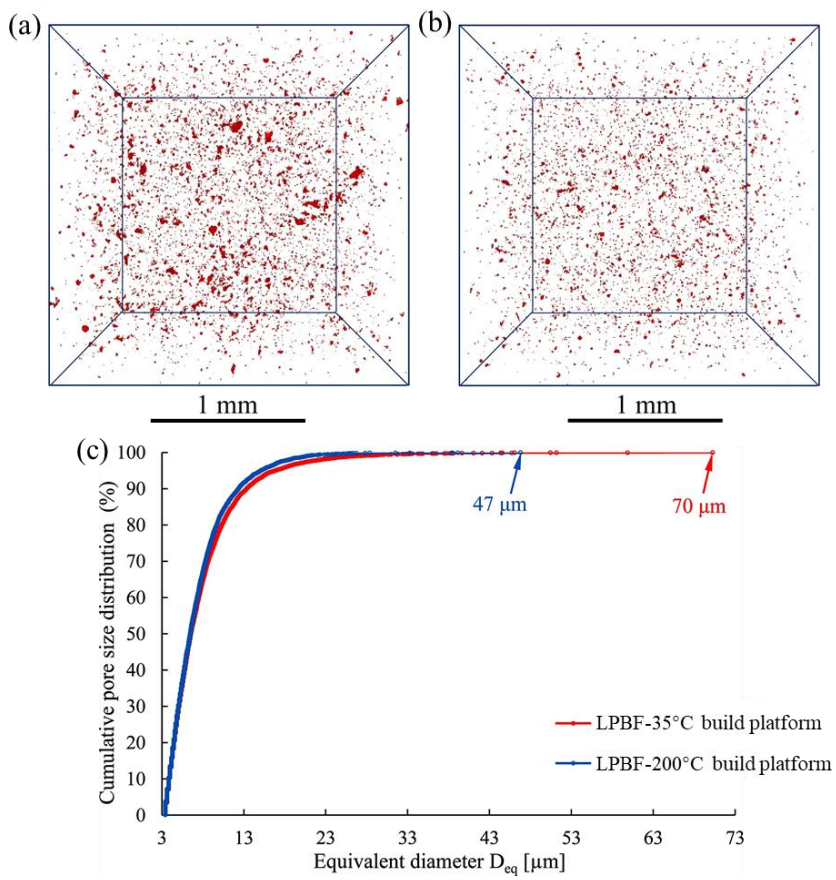

Fig. 19. 3D tomographies showing the porosity of LPBF AlSi10Mg manufactured using machine manufacturer suggested parameters (EOS M290) with a slight build platform preheating to 35°C (a) and a build platform preheating to 200°C (b), cumulative pore size distribution based on the data of (a) and (b) (c) [38]. The figures are reproduced with permission from Elsevier.

4. Strength and ductility

As important indicators of mechanical performance, high strength and ductility are generally required in engineering applications. Owing to the high cooling rate of the process, LPBF AlSi10Mg exhibits a fine microstructure, which imparts higher mechanical strength than its counterparts manufactured by conventional casting and powder metallurgy [26, 29, 40, 145].

4.1 Statistics on literature data

Based on data reported in previous works, statistics on tensile properties of as built LPBF

AlSi10Mg are performed and presented in Fig. 20, which involve specimens manufactured using different parameters/conditions and tensile tests in the directions both perpendicular (horizontal specimens) and parallel (vertical specimens) to the building direction. It should be noted that the cooling rate in Fig. 20f is estimated using Eq. 1, with thermal conductivity of 150 W/m/K [106], laser energy absorption coefficient of 0.35 [107], liquidus and solidus temperatures of 594°C and 558°C, respectively [106]. Note that quite many previous works did not provide complete process parameters, especially build platform temperature, Fig. 20c-f therefore presents fewer data points compared to Fig. 20a and b.

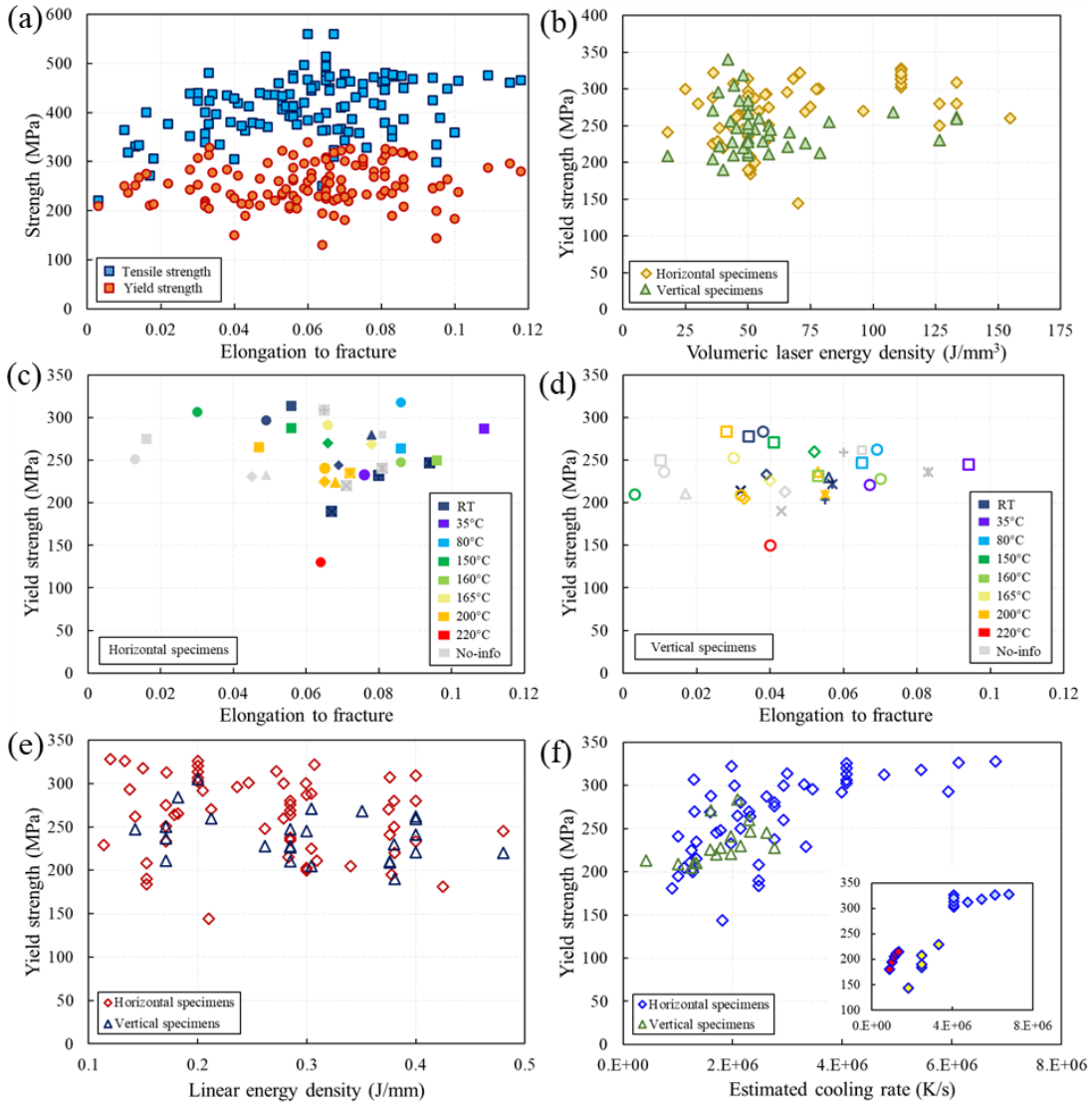

Fig. 20. Statistics on tensile properties of as built LPBF AlSi10Mg based on data reported in literature. Strength vs. elongation to fracture (a), yield strength vs. volumetric laser energy density (b), yield

strength vs. elongation to fracture with different build platform temperatures for horizontal specimens (c) and vertical specimens (d), yield strength vs. linear energy density (e), yield strength vs. estimated cooling rate (f). Horizontal specimens involve loading direction perpendicular to building direction while vertical specimens involve loading direction parallel to building direction. The data points are collected from Refs [27, 31, 36-38, 40, 41, 43-46, 49, 52, 55, 62, 64, 65, 68, 81, 88, 91, 93, 110-120, 123, 125, 127, 146-159]. The inset in (f) shows three individual studies (from left to right [159], [68], [155]) where the effect of cooling rate on yield strength of horizontal specimens can be observed.

From Fig. 20a, it can be seen that the yield strength and tensile strength are generally larger than 200 MPa and 350 MPa, respectively, both involving an important scattering. Interestingly, the well-known strength-ductility trade-off is absent, as the elongation to fracture seems to be independent of the yield or tensile strength (Fig. 20a). In addition, the correlation between strength and laser energy density cannot be established (see Fig. 20b) based on the data gathered from different works. Even in a same study fixing several influential factors such as powder quality, manufacturing environment, and build platform temperature, mechanical properties can still be different at identical energy density. Giovagnoli et al. [36] showed that the tensile properties could significantly vary at a similar energy density (fixing laser power and layer thickness) when varying the hatch spacing and scan speed. Paul et al. [49] also reported quite scattered tensile properties at different combinations of laser power, layer thickness, hatch spacing and scan speed, while keeping the energy density constant. In fact, mechanical strength seems to depend on individual laser parameter, in the opposite way to the microstructure fineness (see section 2.4) as finer microstructure grants higher strength [49, 68].

At fixed process parameters, build platform preheating was widely reported to induce a change in strength [26, 81, 160, 161]. Nevertheless, when plotting the literature data with different build platform temperatures and process parameters, no clear correlation between build platform temperature and mechanical properties can be established, as illustrated in Fig. 20c and d. Note that the solid and hollow symbols in Fig. 20c and d represent horizontal and

vertical specimens in a same study. This implies that the process parameters and build platform temperature jointly determine the mechanical properties of LPBF AlSi10Mg. In other words, it will be challenging to accurately predict the mechanical properties without resolving the coupled effect between laser parameters and build platform temperature.

Laser power (P) and scan speed (v) can influence microstructure fineness of LPBF AlSi10Mg (see section 2.4). When plotting yield strength vs. linear energy density ($LED=P/v$) with previously reported data involving different build platform temperatures, a faint trend such that a higher LED leads to a lower yield strength can be observed, see Fig. 20e. Furthermore, if the build platform temperature is also considered, i.e., turning to assess the cooling rate with Eq. 1, Fig. 20f shows that an increase of cooling rate generally results in an increase of yield strength. It should be noted that this trend is particularly enhanced by several studies ([68], [155] and [159]) shown in the inset of Fig. 20f, where the cooling rate-strength correlation is stronger since the same printing machine and powder are used in each study. Indeed, cooling rate can be regarded as an indicator of strength of LPBF metals when only varying process parameters, as also shown for other alloys, such as Cu-Sn [162] and Al-Ce [163] alloys.

Excluding the specific cases, the rest of the data points in Fig. 20f still present a moderate scattering. This scattering can be due to several factors, such as powder size [138], shape and manufacturing process [159], and usage of virgin or recycled powder [42]. Besides, nanosized Si-rich particles within Al cells cannot be fully linked to cooling rate, as discussed in section 2.4 (see also Table 1), whereas precipitate strengthening can be a major strengthening mechanism [26]. Moreover, the cooling rate calculated with Eq. 1 is just an approximation, the real thermal history being more complex during printing, as indirectly shown through precipitation shape and size by Hadadzadeh et al. [28].

LPBF AlSi10Mg has been widely reported to exhibit anisotropic tensile properties [46, 49, 55, 62, 81, 113, 116, 148], especially in terms of ductility, as shown in Table 2. When comparing

the tensile properties between horizontal and vertical specimens, horizontal specimens generally exhibit superior performance in terms of yield strength and elongation to fracture (see Table 2). Nevertheless, vertical specimens present higher strain hardening capacity and consequently higher ultimate tensile strength even with a lower elongation to fracture, as shown by Paul et al. [49] and Zhao et al. [47]. The mechanisms for these anisotropic behaviors will be addressed in section 4.5.

Table 2. Anisotropic strength and ductility of as built LPBF AlSi10Mg. Horizontal specimen means that loading direction is perpendicular to building direction, vertical specimen means that loading direction is parallel to building direction.

Laser power (W)	Scan speed (mm/s)	Layer thickness (μm)	Hatch spacing (μm)	Platform temperature (°C)	Specimen orientation	Yield strength (MPa)	Tensile strength (MPa)	Elongation to fracture (%)	Ref.
240	500	50	200	RT	Horizontal	245	420	5.9	[93]
					Vertical	220	400	3.2	
960	>1000	50	200	RT	Horizontal	232	415	8.0	
					Vertical	204	437	5.5	
380	1000	30	100	RT	Horizontal	280	472	7.8	[62]
					Vertical	230	475	5.6	
-	-	60	190	RT	Horizontal	247	425	9.4	[81]
					Vertical	222	400	5.7	
-	-	30	190	RT	Horizontal	190	323	6.7	[49]
					Vertical	214	340	3.2	
-	-	30	100	RT	Horizontal	244	367	6.9	
					Vertical	233	380	3.9	
-	-	30	100	RT	Horizontal	314	469	5.6	
					Vertical	278	437	3.4	
-	-	30	100	RT	Horizontal	297	436	4.9	
					Vertical	284	435	3.8	
390	1300	30	190	35	Horizontal	287	475	10.9	[47]
					Vertical	245	470	9.4	
400	1000	-	200	35	Horizontal	233	328	7.6	[110]
					Vertical	221	310	6.7	
370	1300	30	190	35	Horizontal	238	464	10.1	[111]
					Vertical	228	478	7.0	
370	1300	30	190	80	Horizontal	264	451	8.6	[112]
					Vertical	247	482	6.5	
370	-	30	100	80	Horizontal	318	450	8.6	[113]
					Vertical	263	410	6.9	
350	1650	30	130	150	Horizontal	270	450	6.6	[46]
					Vertical	260	460	5.2	
350	1150	50	170	150	Horizontal	288	414	5.6	[114]
					Vertical	271	419	4.1	
350	930	50	170	150	Horizontal	307	424	3.0	[88]
					Vertical	210	221	0.3	
340	1300	30	200	160	Horizontal	248	386	8.6	[115]
					Vertical	228	412	7.0	

-	-	30	-	160	Horizontal	250	389	9.6	[55]
					Vertical	232	423	5.3	
370	1300	30	130	165	Horizontal	269	418	7.8	[116]
					Vertical	226	429	4.0	
-	-	30	-	165	Horizontal	291	444	6.6	[118]
					Vertical	253	440	3.0	
370	1300	30	190	200	Horizontal	235	389	7.2	[117]
					Vertical	210	392	5.5	
350	930	50	420	200	Horizontal	241	399	6.5	[120]
					Vertical	209	357	3.2	
350	1150	50	170	200	Horizontal	225	364	6.5	[119]
					Vertical	205	377	3.3	
300	1650	30	130	200	Horizontal	265	440	4.7	[91]
					Vertical	284	438	2.8	
1000	-	60	-	200	Horizontal	224	365	6.8	[118]
					Vertical	236	406	5.3	
960	>1000	50	200	220	Horizontal	130	250	6.4	[93]
					Vertical	150	305	4.0	
400	1000	25	175	-	Horizontal	-	358	7.4	[146]
					Vertical	-	334	3.6	
175	1025	30	97.5	-	Horizontal	233	370	4.9	[147]
					Vertical	211	272	1.7	
-	-	-	-	-	Horizontal	241	379	8.1	[148]
					Vertical	236	351	8.3	
175	1025	30	97.5	-	Horizontal	251	331	1.3	[149]
					Vertical	237	318	1.1	
350	920	-	-	-	Horizontal	220	360	7.1	[150]
					Vertical	190	363	4.3	
175	1025	30	97.5	-	Horizontal	275	400	1.6	[65]
					Vertical	250	364	1.0	
100	250	30	100	-	Horizontal	280	455	8.1	[151]
					Vertical	262	474	6.5	
-	-	-	-	-	Horizontal	231	379	4.5	[31]
					Vertical	213	413	4.4	
200	1400	30	105	-	Horizontal	262	391	5.6	[152]
					Vertical	247	396	3.5	

As reviewed in section 2.5, post-printing heat treatments alter the microstructure of as built LPBF AlSi10Mg, leading to changes in mechanical properties. Fig. 21 shows normalized yield strength, tensile strength and elongation to fracture after direct aging, stress relief heat treatment and T6 treatment over as built state. It can be seen that direct aging generally enhances mechanical strength but decreases ductility. Stress relief heat treatment breaks down the Si-rich eutectic network, improving ductility at the expense of strength. T6 heat treatment eventually leads to a good combination of yield strength and ductility. Nevertheless, strain hardening capacity is always reduced after T6 treatment, as reflected by the lower tensile strength despite

much higher elongation to fracture (see Fig. 21b). Note that a strong strain hardening can enhance fracture toughness [164] and resistance to fatigue crack growth [165].

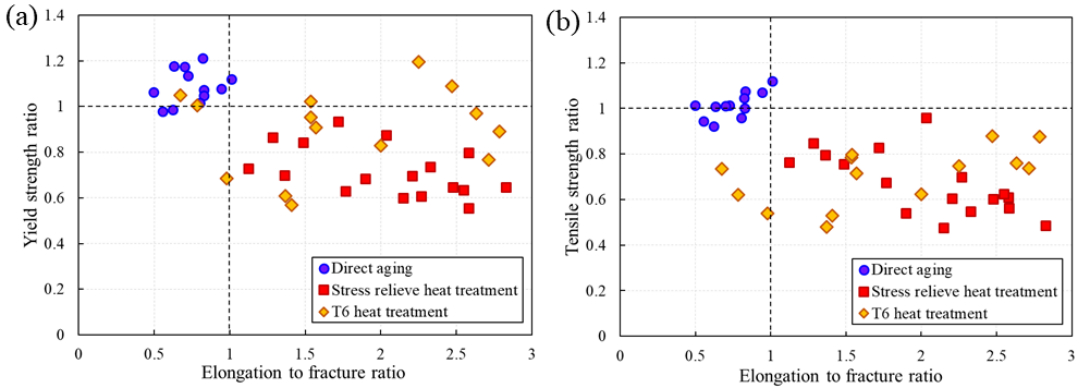

Fig. 21. Effect of post-printing heat treatments on mechanical properties of LPBF AlSi10Mg based on data reported in literature. Normalized yield strength vs. normalized elongation to fracture (a), normalized tensile strength vs. normalized elongation to fracture (b). The normalization is performed over strength and elongation to fracture of the as built state. In the two plots, direct aging involves a temperature range from 130°C to 200°C, stress relief heat treatment involves a temperature range from 290°C to 330°C, T6 treatment involves a solid solution temperature range from 525°C to 550°C and an artificial aging temperature range from 160°C to 190°C. The data points are collected from Refs [62, 64, 81, 111, 112, 114, 116, 123-125, 127-129].

From the current state of the art, it can be concluded that mechanical properties of LPBF AlSi10Mg present quite large scattering. It is still hard to directly correlate mechanical properties with process conditions (laser parameter, scan strategy and build platform temperature), although cooling rate can give an approximate indication of yield strength level. In view of building a process-microstructure-performance roadmap, the following subsections (4.2-4.5) will be devoted to thoroughly review the strengthening, hardening and damage mechanisms and identify their dependence on microstructure and defects of LPBF AlSi10Mg.

4.2 Strengthening mechanisms

The mechanical strength of LPBF AlSi10Mg is closely related to its trans-scale and hierarchical structure, which leads to multiple strengthening mechanisms. In literature, no

systematic investigation of strengthening mechanisms has been performed. Nevertheless, several attempts have been made to link tensile strength to internal structure features, using either experimental measurements or theoretical models. The present review will discuss several important mechanisms or potential contributing factors, from the viewpoints of dislocation evolution inside Al cells, load bearing effect of Si-rich network and strain gradient induced strengthening effect.

4.2.1 Dislocation motion related strengthening

Dislocation motion accommodates plastic deformation of the Al matrix and thus controls global yielding of the material. Interactions between dislocations and defects or secondary phases enhance dislocation slip resistance, leading to mechanical strength increase. As reviewed in section 2, LPBF AlSi10Mg presents a large volume fraction of Si-rich eutectic structure (roughly 12% at equilibrium state [62]), in the form of solid solution, nanosized particles and network, all impeding dislocation motion in theory.

The interactions between nanosized particles and dislocations have been experimentally observed. Wu et al. [39] conducted a series of in situ TEM compression tests to monitor dislocation motion in a bi-grain pillar containing thin and thick Si-rich networks (Fig. 22a-e). Fig. 22c-e shows detailed dislocation patterns in a single Al cell, corresponding to the square area in Fig. 22a. With the increase of load, many dislocations were observed to be pinned by the Si-rich particles in the Al cell center, as indicated by the red arrows in Fig. 22d. As the load was further increased, a higher dislocation density could be seen (Fig. 22e), implying a significant dislocation multiplication. Takata et al. [41] also revealed an extremely high dislocation density both in Al cell interior and at Al cell boundaries in a tensile sample deformed to 3%, as illustrated in Fig. 22f. In the case of preheating build platform to a relatively high temperature (e.g., 200°C), Si particles grow to a rather large size, and their effect on dislocations can be clearly captured by TEM observations. Hadadzadeh et al. [42] showed dislocation

pinning and bypassing processes during the interaction with the Si particles embedded in the Al cells (Fig. 22g).

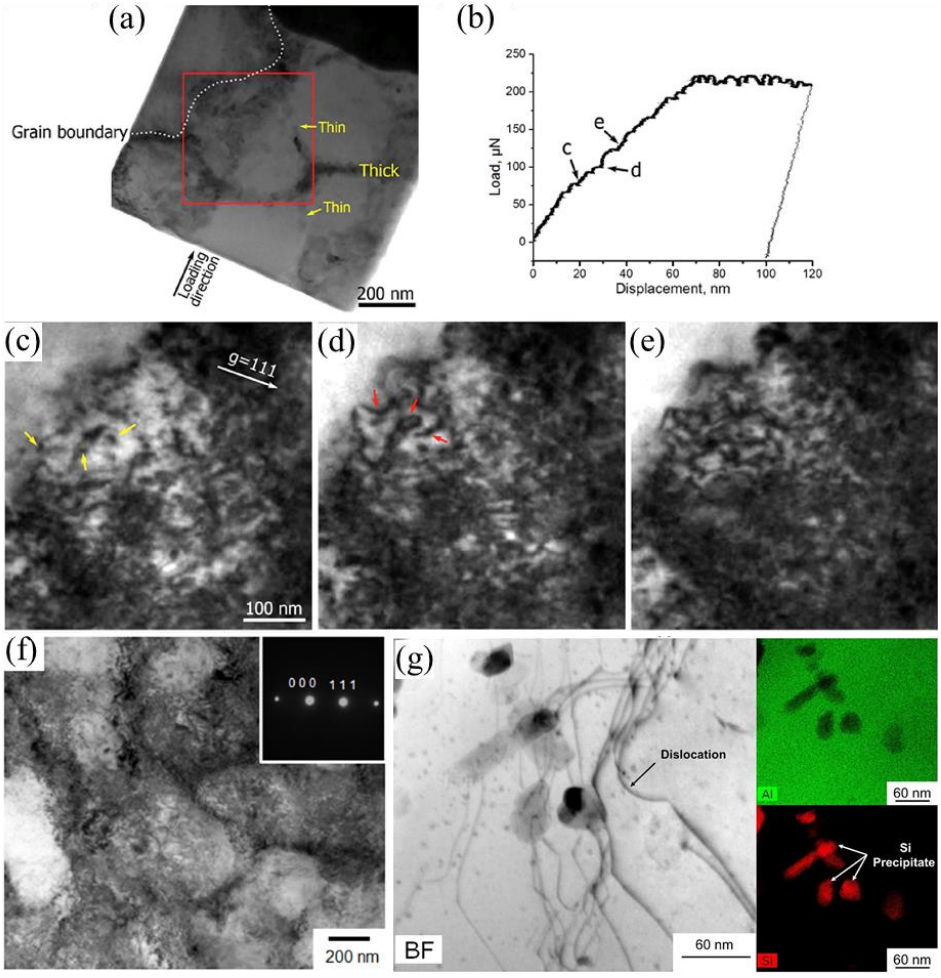

Fig. 22. Dislocation evolution during deformation of LPBF AlSi10Mg. In situ TEM compression test on a bi-grain containing thick and thin Si-rich eutectic networks (a), corresponding loading curve (b) and dislocation evolution during the compression observed in the area highlighted by the red rectangle in (a) and at different load levels indicated in (b) (c)-(e) [39], dislocation pattern in a tensile specimen deformed to 3% [41] (f), dislocation-Si precipitate interaction in a deformed tensile specimen containing relatively large Si particles [42] (g). The figures are reprinted with permission from Elsevier.

The strengthening contribution of nanosized particles (precipitates) with the bypassing interaction can be modeled by the Orowan equation [166]

$$\Delta\sigma_{\text{preci}} = \frac{MGb}{l} \tag{4}$$

where M is the Taylor factor, G is the shear modulus, b is the amplitude of Burger's vector and l is the particle spacing in the slip plane, which can be calculated with the mean diameter d_{preci} and the volume fraction f_{v} of the particles according to Friedel's statistical model [167]

$$l = \frac{d_{\text{preci}}}{2}\sqrt{\frac{2\pi}{3f_{\text{v}}}} \tag{5}$$

Note that a more accurate prediction of precipitate strengthening lies on a more precise measurement of particle size and volume fraction, which can be achieved by the FIB/SEM tomography or 3D TEM tomography [168]. Santos Macías et al. [26] recently estimated the contribution of Si particles to yield strength based on both FIB/SEM tomography and TEM imaging [27]. They found that the Orowan mechanism could induce a significant strengthening of 158 MPa (for a global yield strength of 286 MPa) from very fine particles (12 nm). Moreover, the precipitate contribution dropped to 44 MPa for large particles (60 nm), partially explaining the lower strength of material built with preheated build platform. The exceptional strengthening effect of nanosized particles was also suggested by Takata et al. [41], based on the comparison of strength between as built and annealed samples.

It is worth mentioning that the strengthening effect of solid solution should also be taken into account for as built LPBF AlSi10Mg, as it exhibits supersaturated Al matrix, see section 2.1.1. To estimate the contribution of solid solution, the following equation, widely used for heat-treatable Al alloys, can be employed

$$\Delta\sigma_{\text{ss}} = k_{(\text{Si})}(C_{\text{Si}})^{2/3} \tag{6}$$

where $k_{(\text{Si})}$ is a constant and C_{Si} denotes the concentration of Si in solid solution.

The concentration of Mg, presents a low value in AlSi10Mg and can be neglected. However, the solid solution of Si can be significant in the as built state [27, 81]. Santos Macías et al. [26] showed that a concentration of 2.4 wt.% could induce a strengthening as high as 71 MPa.

The Si-rich eutectic network also presents a strengthening effect. In contrast to the

conventional microstructure of Al alloys in which secondary phases are embedded in Al matrix, the Al matrix of LPBF AlSi10Mg is enclosed by the Si-rich network, forming submicron cells. Therefore, dislocations in the Al matrix are expected to pile-up at the Al cell boundaries [43]. Indeed, through in situ TEM compression tests, Wu et al. [39] noted that no obvious penetration of dislocations through cell boundaries could be observed, only some dislocations were transmitted through thin discrete Si network. Li et al. [43] also reported an extremely high dislocation density near the Al/Si interfaces, as illustrated in Fig. 23a-c.

The strengthening effect imparted by the Si-rich network can be analogue to grain boundaries. Some researchers [26, 42] have already attempted to model the effect of the Si-rich network via the Hall-Petch relation

$$\Delta\sigma_{\text{bound}} = \frac{k_d}{\sqrt{d_{\text{net}}}} \tag{7}$$

where d_{net} denotes the width of the Si-rich eutectic network and k_{d} the constant of Hall-Petch relation. The strength contribution of cell boundary (or Si network) was found to be about 50-60 MPa [26, 42], using the constant $k_{\text{d}} = 0.04$ MPa.m$^{1/2}$ generally adopted for Al alloys.

As illustrated earlier in this review, LPBF AlSi10Mg exhibits a heterogeneous microstructure, manifested by the difference in morphology and size of the Si phase in the FMP, CMP and HAZ. The dislocation pile-up is expected to be the strongest in the FMP, while it will be mitigated in the CMP due to larger cell size (i.e., lower constraint effect) and significantly weakened in the HAZ due to the degraded Si network connectivity. Assuming negligible variation in solid solution and nano-sized particles throughout the melt pool, the dislocation pile-up mechanism can partially explain the highest and lowest strength (hardness) in the FMP and HAZ, respectively (see Fig. 23d and e).

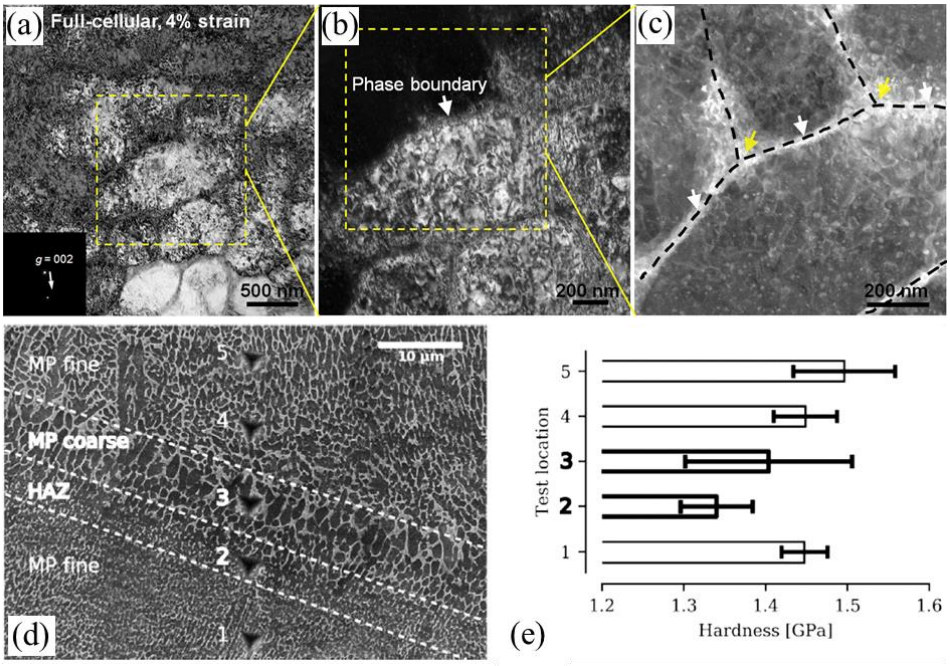

Fig. 23. TEM observation of dislocations in post-deformation sample at a strain of 4% under the {110}-type diffraction conditions (a)-(c) [43], nanoindentation tests across a melt pool border (d) and corresponding hardness values in FMP, CMP and HAZ (e) [45]. The figures are reprinted or reproduced with permission from Elsevier.

Given the complex morphology of the Si-rich network in the HAZ (see Fig. 10), it is quite challenging to establish a theoretical strengthening model to evaluate the interaction between the dislocations and the degraded network. Numerical simulations via discrete dislocation dynamics or crystal plasticity could be potential tools to tackle this issue.

4.2.2 Load bearing of Si-rich network

The previous subsection has addressed Al matrix strengthening from the dislocation motion viewpoint. As LPBF AlSi10Mg presents a non-negligible volume fraction of "hard" Si-rich network, the load bearing effect of the secondary phase also contributes to the yield strength. Using in situ X-ray diffraction or neutron diffraction, stress partition between Al and Si phases has been probed throughout the macroscopic deformation process [44, 71, 169]. Zhang et al. [44] showed that the average lattice strain in the loading direction (LD) was close between the Al and Si phases (around 3700×10^{-6} in the loading direction) before the macroscopic yield point,

as can be seen in Fig. 24. Note that the yield point approximately corresponds to the end of region 2. As the elastic modulus of Si is higher than that of Al (elastic modulus of amorphous Si is further discussed in section 4.3.2), the calculated effective stress is therefore higher in the Si phase, increasing the global yield strength [71].

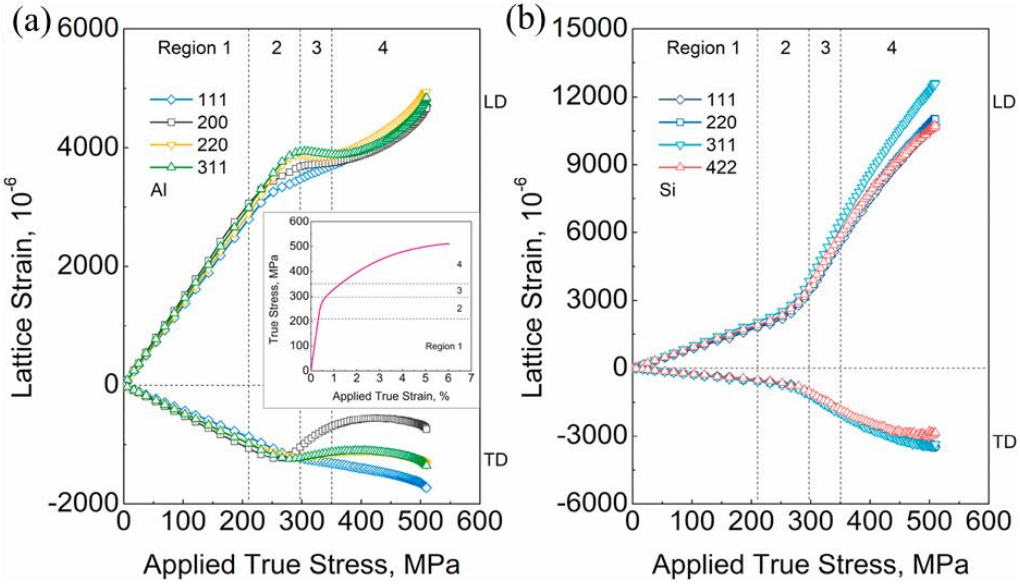

Fig. 24. Phase strain evolution as a function of applied true stress obtained from in situ X-ray diffraction tensile test [44]. The vertical dashed line between regions 2 and 3 marks approximately the yield point. Orientation-dependent strains of the selected lattice planes in the Al (a) and Si (b) phases. The figures are reprinted with permission from Elsevier.

The load bearing contribution can be considered using the simple composite model (i.e., rule of mixture)

$$\sigma^{y}_{\text{total}} = f_{\text{Al}}\sigma^{y}_{\text{Al}} + f_{\text{Si}}\sigma^{y}_{\text{Si}} \tag{8}$$

where f_{Al} and f_{Si} represent the volume fractions of the Al and Si phases, respectively, whilst σ^{y}_{Al} and σ^{y}_{Si} denote the phase stresses of the Al and Si phases upon yielding, respectively. Based on the calculated phase stresses from {311} strains, the stress partitioning ratio of Si (i.e., $f_{\text{Si}}\sigma^{y}_{\text{Si}} / \sigma^{y}_{\text{total}}$, with $f_{\text{Si}} = 9.6\%$) was found to be about 13.5% during the elastic stage [44], proving a slight strengthening from the secondary phase via the load bearing mechanism.

The analysis of strengthening mechanisms using analytical models allows to identify the critical microstructure feature favoring high strength, as generally employed for LPBF alloys [162]. Based on the aforementioned strengthening models (Eqs. 4-8), Santos Macías et al. [26] assessed the yield strength of as built LPBF AlSi10Mg samples presenting two distinct microstructures (see Fig. 14). The microstructure features were extracted from fine melt pool zone and the loading direction was perpendicular to the building direction (i.e., horizontal specimen). It is found that the precipitate strengthening presents the largest contribution when the nanosized Si-rich particles within Al cells are small (12 nm). On the other hand, when these Si-rich particles grow to a larger size (60 nm), there is no major strengthening mechanism, as the contributions from Si-rich particles, Si-rich eutectic network boundary, Si solid solution and Si-rich eutectic load bearing are quite similar (see Table 3).

Table 3. Estimation of yield strength of FMP in horizontal direction using theoretical strengthening models [26]. The units are in MPa.

$T_{\text{Build platform}}$	σ_0	$\Delta\sigma_{\text{preci}}$	$\Delta\sigma_{\text{bound}}$	$\Delta\sigma_{\text{ss}}$	$\Delta\sigma_{\text{disloc}}$	$f_{\text{net}} \times \sigma_{\text{load}}$	Estimated σ_{y}	Measured σ_{y}
35°C	10	158	66	71	37	46	347	286
200°C	10	44	55	54	37	46	222	203

4.3 Strain hardening

It has been widely recognized that as built LPBF AlSi10Mg exhibits an excellent strain hardening capacity [40, 41, 44, 47]. Compared to strengthening mechanisms, strain hardening mechanisms were rarely studied. In fact, the analysis of sources for hardening is akin to that for yield strength; i.e., the hardening of the Al phase related to the dislocation motion and the load bearing of the Si-rich network.

4.3.1 Dislocation driven hardening

Strain hardening of the Al phase originates from increasing barrier force against dislocation slip. The barriers can be dislocation forests, solute atoms, precipitates, grain boundaries and

phase boundaries.

For LPBF AlSi10Mg, the initial microstructure, i.e., supersaturated solid solution, nanosized Si particles and Si network boundaries, intrinsically act as effective strain hardening sources. On the other hand, dislocation density is revealed to rapidly increase during deformation, not only near the Al/Si interface, but also within the Al cells, significantly enhancing dislocation forest hardening. Hadadzadeh et al. [42] reported entangled dislocation networks in the cell interior of a deformed sample through TEM observations. Li et al. [43] also used TEM micrographs to estimate the dislocation density corresponding to a tensile deformation of 4%. They observed a high density of ~10^{16} m^{-2} within the Al cells and an exceptionally high density of ~10^{17} m^{-2} at the triple junctions of cells. Based on peak broadening of the X-ray diffraction spectrum, Zhang et al. [44] tracked the dislocation density evolution along with the tensile deformation. They revealed that the dislocation density first raised very quickly at the incipient stage of plastic deformation (<2%), and then the increase rate dropped significantly. The high dislocation density indicates the existence of substantial dislocation multiplication sites, probably being supersaturated solute atoms, nanosized particles and slip plane-dislocation forests intersecting points (i.e., Frank-Read sources).

Owing to the difference in mechanical strength, geometrically necessary dislocations (GNDs) are expected to develop to accommodate the strain gradient arising at both the melt pool and Al cell hierarchies. Indeed, the harder Si network would restrict the deformation of the softer Al near the interfaces, thus conferring a large strain gradient and consequently a high density of GNDs at/near the Al/Si interfaces. Li et al. [43] demonstrated enhanced kernel average misorientation at the Si network boundaries (see Fig. 25a and b), which was further translated into the GND density presenting a value of the order of 10^{16} m^{-2}. At the melt pool hierarchy, as the melt pool border (i.e., CMP and HAZ) presents a lower mechanical strength compared to the melt pool interior (i.e., FMP) (Fig. 23d and e), a strain gradient will be

established at the melt pool border, especially when the loading direction is parallel to the building direction. This was proved by Ben et al. [170] and Song et al. [171] who revealed concentrated KAM values near the melt pool border (see Fig. 25c and d).

It is noteworthy that the strain gradient is generally low at the macroscopic yield point (0.2% plastic strain), thus the strengthening effect of GNDs is not expected to be significant. On the contrary, the strain gradient would continuously increase during the flow stage, therefore leading to rapid generation of GNDs, which, in turn, would significantly enhance flow strength. Unfortunately, no quantitative analysis has been performed to account for GNDs in the strain hardening of LPBF AlSi10Mg.

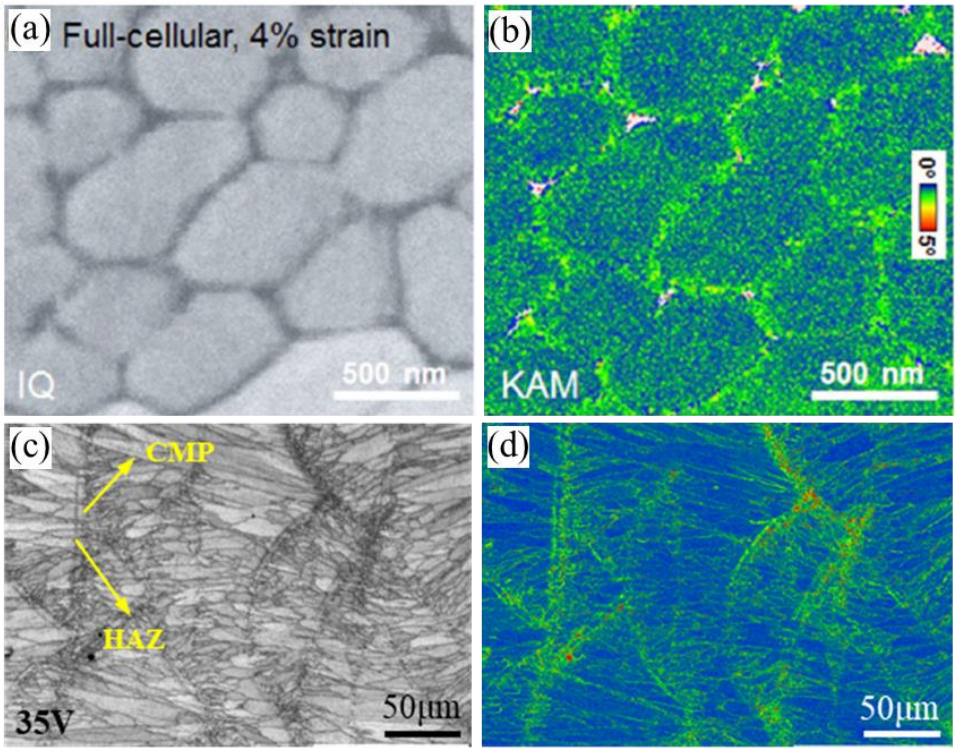

Fig. 25. Strain gradient at Al cell and melt pool hierarchies. Typical image quality (IQ) map (a) and KAM map (b) of the deformed Al cell structure (plastic strain: 4%) [43], typical image quality (IQ) map (c) and KAM map (d) of the deformed melt pool structure [171]. The figures are adapted with permission from Elsevier.

4.3.2 Load bearing driven hardening

The Si-rich eutectic network of as built LPBF AlSi10Mg is composed of both crystalline

and amorphous structures (see Fig. 6). The resistance to deformation of crystalline Si is much higher than that of crystalline Al due to the following two factors: first, Si is stiffer than Al; second, the α-Al phase exhibits plasticity while Si crystal normally deforms elastically. It is noteworthy that the Si-rich eutectic network of LPBF AlSi10Mg presents an amorphous component (see Fig. 6). Amorphous Si was widely reported to present a lower Young's modulus than its crystalline counterpart (130-188 GPa depending on the crystallographic orientation [172]). Experimental works reported a value of about 120 GPa [173, 174], while theoretical models predicted a value in the range of 90-100 GPa [175, 176]. Despite this discrepancy, these values are still higher than that of the Al phase (around 70 GPa). Moreover, a recent in situ TEM tensile test showed that amorphous Si deforms almost elastically till 5-6 GPa [177]. In this sense, elastically deformed Si-rich eutectic would exhibit an excellent load bearing capacity during the macroscopic plastic deformation of the whole material. Through in situ X-ray diffraction tensile tests, Zhang et al. [44] assessed the phase stresses, and showed a significant hardening effect owing to the high stress within the Si phase (up to 2 GPa, see Fig. 26a). The accuracy of phase stresses was further validated by the reasonably satisfied rule of mixture, as shown in Fig. 26b. Consequently, the contribution of the Si phase to the macroscopic flow stress was demonstrated to reach up to 35.4% with a volume fraction of 9.6% [44].

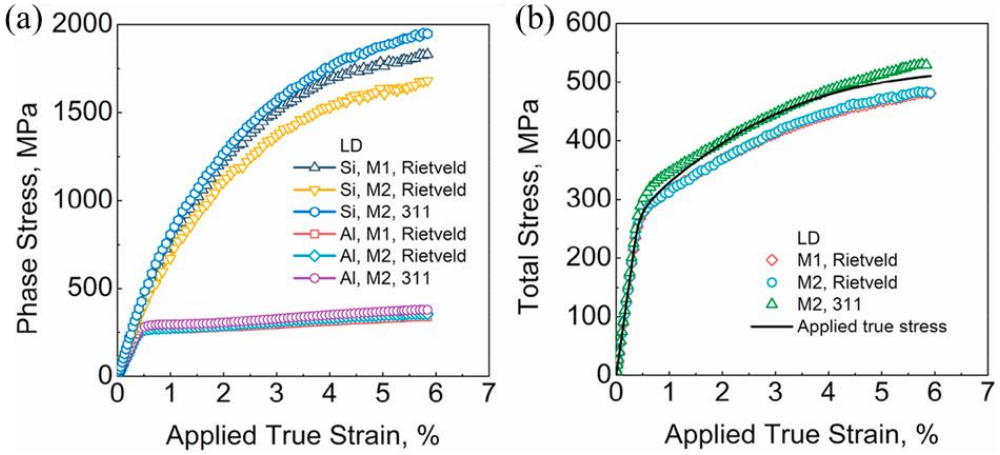

Fig. 26. Phase stress evolution as a function of applied true stress obtained from in situ X-ray diffraction tensile test (a), macroscopic stress evolution using the rule of mixture (b) [44]. The figures

are reprinted with permission from Elsevier.

It is noteworthy that, although Si is generally treated as an elastic material, the deformation mechanism of the Si-rich eutectic in LPBF AlSi10Mg is still not fully clear. Through TEM characterization of the deformed microstructure (see Fig. 27), Kim et al. [178] argued that the Si-rich eutectic might exhibit plastic deformation via formation of stacking faults and twins. The authors showed that during the plastic deformation of the Al-cells, dislocations would pile-up at the Al/Si interface (Fig. 27b), creating intensified stress that shears the Si phase. The possible signs of plasticity are the shear steps detected at the edges of the Si-rich eutectic (Fig. 27e).

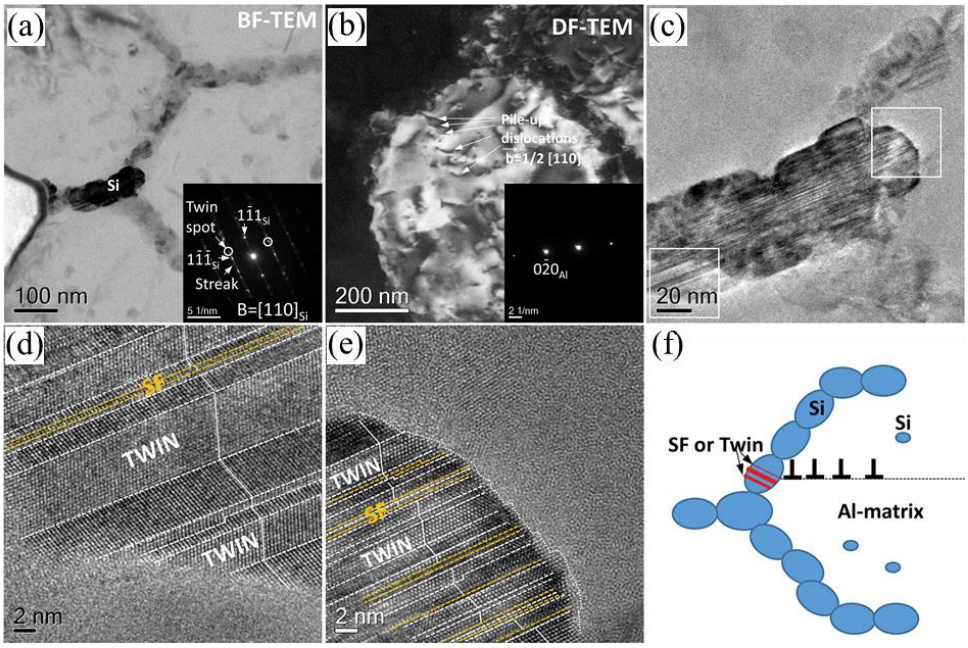

Fig. 27. Possible signs of plastic deformation in the Si-rich eutectic network under tensile load [178]. Bright field (BF)-TEM image and electron diffraction pattern (EDP) of a Si-rich eutectic under $[110]_{Si}$ on-axis conditions (a), dark-field (DF)-TEM image and corresponding EDPs of a α-Al grain (b), a high magnification image (c) and high-resolution (HR)-TEM images (d-e) of the Si-rich eutectic indicated in (a), schematic drawing of the deformation mechanism of the Si-rich eutectic (f). The figures are reprinted with permission from Elsevier.

Despite the possible yielding behavior, Zhang et al. [44] and Kim et al. [71] revealed a much higher phase stress of the Si-rich eutectic compared to the α-Al, confirming the strong load

bearing effect of the Si-rich eutectic and its significant contribution to macroscopic hardening. Nevertheless, the deformation mechanism of the Si-rich eutectic can strongly impact the load partition between the phases in LPBF AlSi10Mg. How to treat the Si-rich eutectic in modeling and simulation remains an important issue when aiming to quantitatively address the phase stress evolution, as will be discussed later in section 7.1.1. It is noteworthy that the phase stress can help to understand the damage mechanism of LPBF AlSi10Mg.

4.4 Damage mechanism

Ductile metallic materials generally fail by void nucleation, growth and coalescence [179]. The damage mechanism therefore determines material ductility. The study of the damage mechanism and its correlation to microstructure is important for AM Al alloys presenting a relatively low elongation to fracture compared to wrought materials. It can potentially point out the direction to optimize the microstructure for higher ductility.

4.4.1 Damage sites and distribution

Typical damage features of LPBF AlSi10Mg are presented in Fig. 28a and c, for horizontal and vertical specimens, respectively. It can be clearly observed that damage (voids) initiates on the Si-rich eutectic due to the fracture of the highly connected network. When looking at the vicinity of the fracture surface (see Fig. 28b and d), the voids are found to present a quite flat shape, as the void ligament size, being that of the Al cell, is relatively small for this cellular structure. The low inter-void spacing can lead to a fast void coalescence without significant growth [27, 47]. Due to the heterogeneous microstructure of LPBF AlSi10Mg, damage distribution is also heterogeneous and loading direction dependent. For horizontal specimens, damage sites are mainly located in the FMP and CMP [26, 27], while all three zones present damaged Si-rich eutectic in vertical specimens [47, 171].

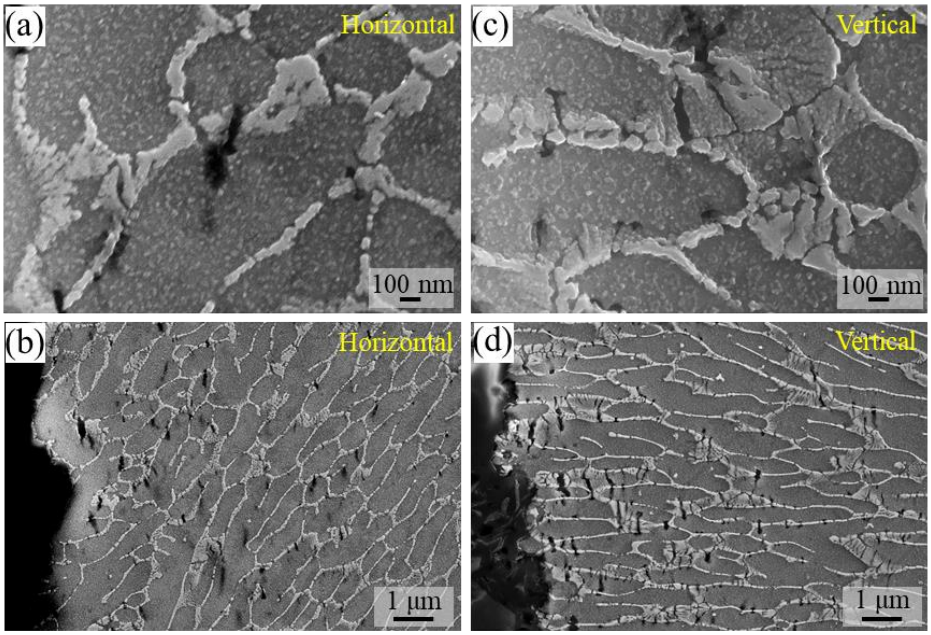

Fig. 28. Typical damage pattern at the vicinity of fracture surface for as built LPBF AlSi10Mg [47]. Damage of horizontal specimen (a)-(b), damage of vertical specimen (c)-(d). The loading direction coincides with the horizontal direction of all micrographs. The figures are reprinted with permission from Elsevier.

Few efforts have been devoted to characterize the macroscopic strain at damage onset. Using in situ SEM tensile testing, Zhao et al. [27] reported that no distinguishable damage evolution could be observed before final failure of horizontal specimens. Recently, Song et al. [171] performed interrupted tensile tests to probe damage status at different strain levels. They studied both horizontal and vertical specimens of two microstructures with different build platform temperatures (35°C and 200°C). It was found that for the finer microstructure (35°C), there was nearly no damage even at about 94% elongation to fracture. The relatively late damage nucleation coincides with the absence of significant damage growth, as explained by Song et al. [171]. For the coarser microstructure, damage could barely be observed at about 96% elongation to fracture in the horizontal specimen, while a large amount of damage was present at about 94% elongation to fracture in the vertical specimen, with a very slight concentration at the melt pool border (i.e., CMP and HAZ). From these observations, it can be concluded that damage evolution is highly dependent on microstructure and loading direction. The anisotropy

in damage behavior will be further discussed in section 4.5.3.

4.4.2 Fracture surface morphology

Fracture surface observation is routinary in the investigation of damage and fracture behavior of metallic materials as it can help to understand damage mechanism and identify the crack propagation path [179]. For as built LPBF AlSi10Mg, the fracture surface morphology is quite different from the round dimple features typically seen in ductile metals [27, 47]. Moreover, horizontal and vertical specimens present different morphologies [31, 47, 49, 150]. As shown in Fig. 29a and d, the fracture surface of vertical specimens generally reveals melt pool traces (also called scan tracks) [47, 49, 113, 150, 180], in contrast to horizontal ones where no melt pool hierarchy structure can be observed [27, 31, 47, 49, 113, 180].

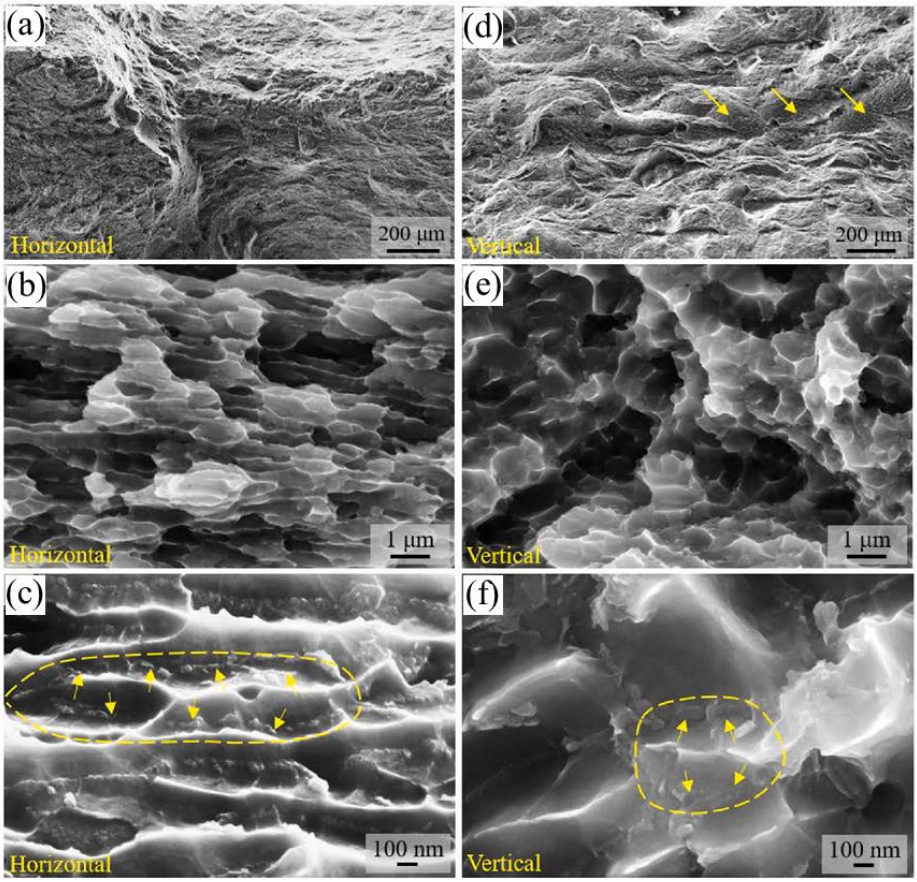

Fig. 29. SEM observations of fracture surface morphology at different magnifications for horizontal (a)–(c) and vertical (d)–(f) specimens [47]. The arrows in (d) point out the traces of the melt pool border. The arrows in (c) and (f) highlight the Si-rich eutectic. The dashed enclosing lines mark the Si-

rich eutectic network. The figures are reprinted with permission from Elsevier.

At higher magnification, lamellar features are generally observed for horizontal specimens [27, 47, 49, 127], as shown in Fig. 29b. This is reminiscent of the Si network shape. However, for vertical specimens, only ridge features can be observed (see Fig. 29e). When further increasing the magnification, the Si-rich eutectic is clearly seen on the fracture surface [27, 31, 45, 47], as illustrated in Fig. 29c and f for horizontal and vertical specimens, respectively. The presence of Si-rich eutectic on the fracture surface is consistent with the damage sites revealed in Fig. 28.

Given the presence of melt pool traces on fracture surface morphology, it can be deduced that failure frequently initiates from melt pool borders for vertical specimens [31, 45, 47, 49, 113, 150, 180]. Delahaye et al. [45] performed statistics on Si-rich eutectic spacing from both intact microstructure and fracture surface for vertical specimens. They argued that fracture preferentially took place through the HAZ based on close mean spacing between the HAZ and the fracture surface. In contrast, damage and fracture mainly occurs in the melt pool interior for horizontal specimens [27, 47, 171]. Patakham et al. [31] distinguished layer-layer and track-track melt pool borders. Based on the fracture surface morphology, they pointed out that cracks eventually propagated along the track-track melt pool borders for horizontal specimens.

4.4.3 Role of initial porosity

To understand how initial porosity participates in the damage and fracture processes of LPBF AlSi10Mg, two kinds of studies have been performed in the current state of the art, by either in situ observations or comparative tests. However, the role of initial porosity on the damage mechanisms of the as built state has not been fully clarified yet, as it seems to be dependent on the porosity size and sharpness, see the discussion below.

Some researchers attempted to monitor the evolution of initial pores during deformation and link them to final failure using in situ X-ray computed tomography [72]. Note that the

typical voxel size of such in situ testing is of the order of 1 μm to have sufficiently large and macroscopically representative tensile specimens. Hastie et al. [72] revealed that the initial pores nearly maintained their sizes in the whole gauge volume during the entire loading stage until fracture, as shown in Fig. 30. However, it cannot be concluded from such measurements that initial porosity does not contribute to damage evolution. The observations could simply be due to the fact that the new voids nucleated from the microstructure are too small (thickness of the flat void is much smaller than 1 μm, see Fig. 27) to be captured by the tomography scans (2.86 μm used in [72]).

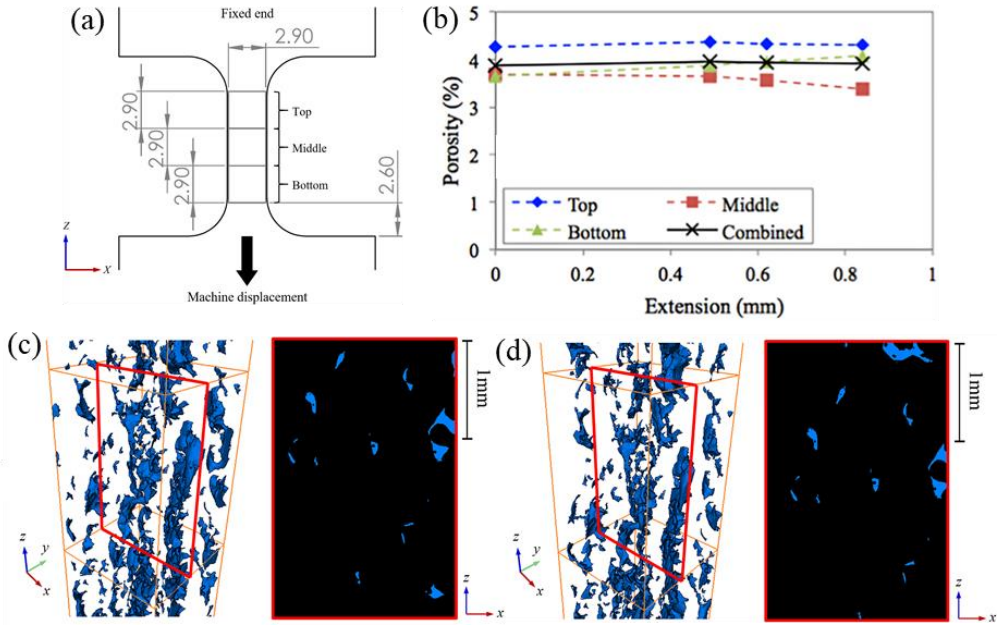

Fig. 30. Evolution of initial porosity during in situ X-ray tomography tensile test [72]. Shape of tensile specimen (a), evolution of porosity at different gauge volumes (b), tomography of pores with D_{eq}>50 μm before loading (c) and near the onset of final failure (d). The figures are reprinted with permission from Elsevier.

To qualitatively reveal the effect of initial pores on ductility, Zhao et al. [27] conducted a series of comparative tests. They demonstrated that a relatively low porosity (around 0.1%, pore equivalent diameter generally smaller than 100 μm) played a secondary role in the damage process, following the microstructure. Nevertheless, large and dense lack of fusion defects could significantly reduce the material ductility, especially for vertical specimens where the

defects promote high stress concentration due to their favorable orientation with respect to external load. The elongation to fracture of sound materials can be ten times larger than flawed ones for both horizontal and vertical specimens, as shown in Fig. 20c and d, respectively. This large scattering can be partially explained by the presence of sharp lack of fusion defects. Indeed, Yang et al. [155] demonstrated that such defects (equivalent diameter in the range of 100-300 μm) could reduce the elongation from 8% to 3% at the same yield strength, even for horizontal specimens. Suzuki et al. [181] also revealed a significant decrease of elongation from 9.3% to 1.4% when the density of LPBF Al-Si parts dropped from 99.8% to 98.2%, despite similar yield strength and strain hardening exponent. Large lack of fusion could even lead to very brittle fracture of as built LPBF AlSi10Mg, as reflected in a case of extremely low ductility (much smaller than 1%) [65, 88, 147]. From the aforementioned studies, it can be deduced that damage can be dominated by either microstructure or initial porosity, depending on the porosity size and sharpness. Moreover, the combined effects of microstructure and moderate initial porosity on ductility is still unclear.

4.5 Anisotropic features

LPBF AlSi10Mg has been widely reported to exhibit anisotropic mechanical properties, in terms of yield strength, strain hardening capacity and ductility (see Table 2). The underlying reasons for the anisotropic features were rarely addressed in previous studies. This section attempts to discuss the possible factors leading to anisotropy based on the afore-established understanding of mechanisms of strengthening, strain hardening and damage. The authors hope this section can inspire readers for further investigations.

4.5.1 Anisotropy in yield strength

As built LPBF AlSi10Mg generally presents higher yield strength when loaded perpendicular to the building direction (i.e., horizontal specimens), but the underlying mechanism is still unclear. Xiong et al. [150] proposed that the strength anisotropy was not

induced by the weak <001> fiber texture as the mean Schmid factor is even slightly higher for the horizontal specimens. This point was further proved by Li et al. [182] who conducted micro-pillar compression tests on single crystal and showed anisotropic strength even under the same crystallographic orientation. Based on the strengthening mechanisms reviewed in section 4.2, the following aspects can be considered for deeper investigations:

(1) Dislocation slip barriers: Assuming a homogeneous distribution of the supersaturated solid solution and nanosized particles, only the elongated cellular Si network can induce different dislocation blocking effects in different loading directions. The Si-rich network might act as a stronger barrier for dislocation slip in horizontal specimens.

(2) Load bearing of Si-rich network: The load transfer normally depends on the volume fraction and aspect ratio of the secondary phase [183, 184]. When considering the morphology of the Si-rich network for load transfer, the effective aspect ratio is higher for vertical specimens [185] (see Fig. 31, leading to higher load bearing effect. Nevertheless, the stress partitioning ratio of the Si phase is relatively low upon yielding ($\sigma_{Si}f_{Si}/\sigma_{macro}$=13.5% with f_{Si} being 9.6% according to Zhang et al. [44]) and the difference in load bearing contribution to yield strength might be relatively small for the two loading directions.

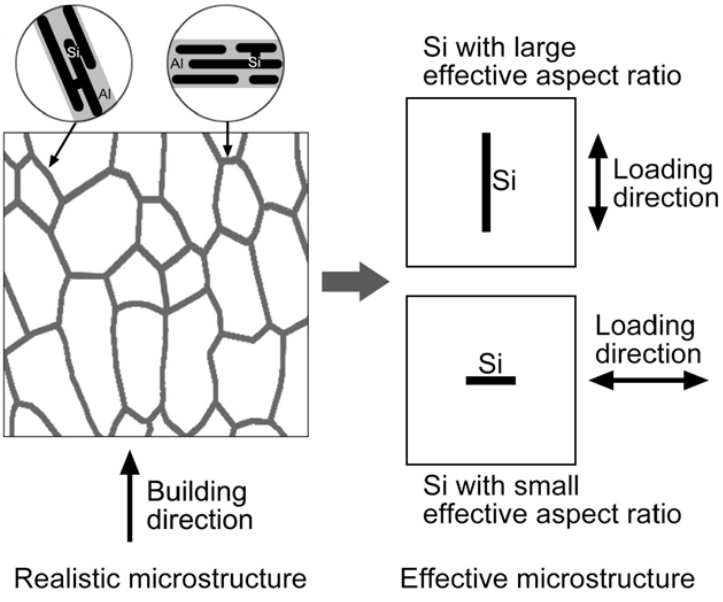

Fig. 31. Schematic drawing of effective aspect ratio of the Si-rich network for horizontal and vertical

specimens [185]. The figures are reprinted with permission from Elsevier.

(3) Role of melt pool border zone: The melt pool border effect on global yielding is expected to be dependent on loading direction. As the strength of CMP and HAZ is smaller than that of FMP [45, 171], the lower yield strength of vertical specimens could be explained by earlier yielding of the melt pool border when loaded along the building direction.

(4) Thermal dislocations and residual stresses: The distributions of initial thermal dislocations [25] and corresponding thermal stresses are expected to be anisotropic due to the thermal gradient pointing toward the melt pool center [91]. Exceptionally, Tan et al. [91] and Li et al. [182] revealed that vertical specimens presented a higher yield strength than the horizontal ones when using a high temperature (200°C) build platform and a stress relief heat treatment at 177°C for 4h, respectively. Both strategies relieve residual stresses while retaining the Si-rich network and nanosized particles in the microstructure. Therefore, thermal dislocations and residual stresses could be potential reasons leading to yield strength anisotropy.

4.5.2 Anisotropy in strain hardening

Although vertical specimens generally present lower yield strength than horizontal ones, their strain hardening capacity has been shown to be stronger. This is well reflected by higher ultimate tensile strength of vertical specimens despite lower yield strength [31, 46, 55, 93, 112, 115, 116] and explicitly revealed by larger strain hardening exponent [49].

Through in situ X-ray diffraction tensile tests on horizontal specimens, Zhang et al. [44] showed that Si phase stress significantly increased in the plastic flow stage, and the load bearing of the Si phase became the predominant contribution to macroscopic hardening. Based on load partition analysis, the higher strain hardening capacity of vertical specimens can be easily understood, in particular for the CMP and FMP regions. As shown in Fig. 31, the effective aspect ratio of the Si-rich network is higher along the building direction; the load bearing of the Si-rich eutectic is therefore expected to be larger, leading to higher strain hardening capacity of

vertical specimens [171]. Indeed, according to micropillar compression tests of FMP zone extracted from horizontal and vertical specimens, it is found that the vertical loading direction involves a stronger strain hardening under the same grain orientations, i.e., identical dislocation slip paths (see Fig. 32) [182]. This suggests that the higher strain hardening capacity of vertical specimens most likely originates from the stronger load bearing effect of the Si-rich network (i.e., higher Si phase stress). To confirm the conjecture, more direct evidence needs to be provided, for example through in situ X-ray diffraction testing or micromechanical simulation on both horizontal and vertical specimens.

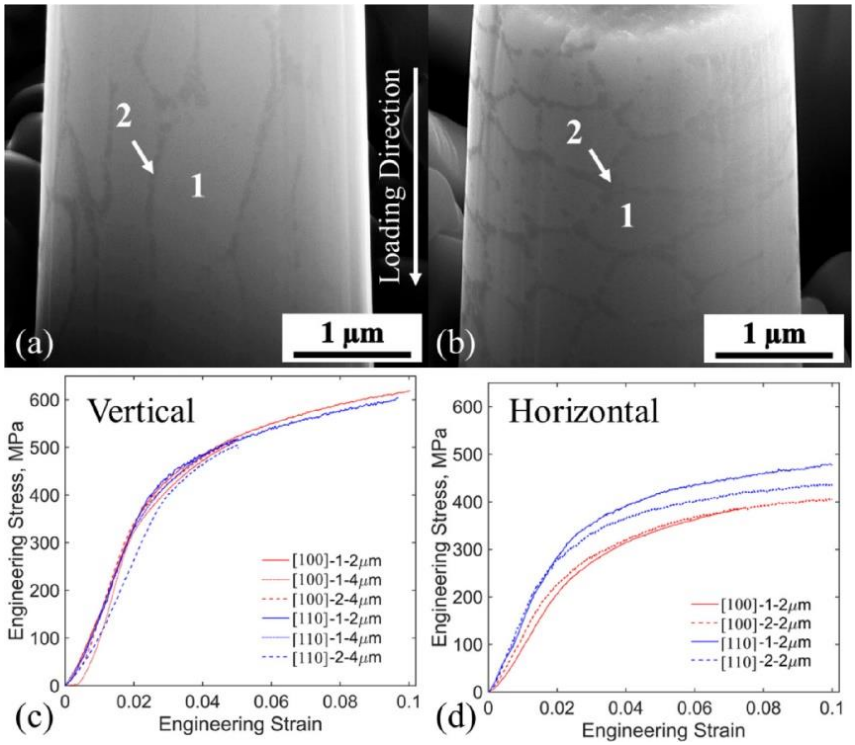

Fig. 32. Micropillar compression tests of FMP microstructure along (a) and perpendicular to (b) the building direction, and corresponding stress-strain curves for different crystal orientations and micropillar diameters for vertical (c) and horizontal (d) compression samples [182]. Regions 1 and 2 in (a) and (b) refer to the cell interior region and the cell wall region, respectively. The figures are reprinted with permission from Elsevier.

In contrast to the FMP and CMP, the degradation of Si network connectivity would lead to significantly smaller aspect ratio of the Si phase and consequently lower Si phase stress (i.e.,

lower load bearing effect) in the HAZ. Nevertheless, the strain gradient across the melt pool border can generate GNDs [170, 171], leading to additional contribution to strain hardening. In this sense, the softening effect of the melt pool border would be limited. How strain gradient hardening affects the load partition between different zones is still an open question.

4.5.3 Anisotropy in damage evolution

In the absence of large initial pores, the failure mechanism of LPBF AlSi10Mg is akin to that of conventional Al alloys, where the damage process is controlled by a hard secondary phase that either fractures or debonds from the Al matrix [186]. Such damage mechanism highly depends on the phase size, shape and relative orientation to loading direction, as these factors determine not only the stress transfer, but also the fracture strength of the secondary phase [187].

As the Si-rich eutectic mainly manifests as an elongated and interconnected network in LPBF AlSi10Mg, damage is found to exhibit anisotropic evolution behavior, especially when the Al cells are weak. Song et al. [171] investigated the damage mechanisms of samples built with the same LPBF parameters but different build platform temperatures, i.e., 35°C and 200°C. While the 35°C microstructure presents similar damage behavior for horizontal and vertical specimens, the 200°C counterpart exhibits anisotropic damage evolution. The anisotropy is manifested by the fact that damage initiates extremely close to final fracture in horizontal specimens but appears much earlier and experiences a relatively long growth process in vertical specimens (see Fig. 33a-f). The nano-hardness difference between highly deformed and intact microstructures coincides with the damage states for the two loading directions, the horizontal and vertical specimens undergoing hardness increase and decrease with respect to the intact state, respectively (see Fig. 33g-h).

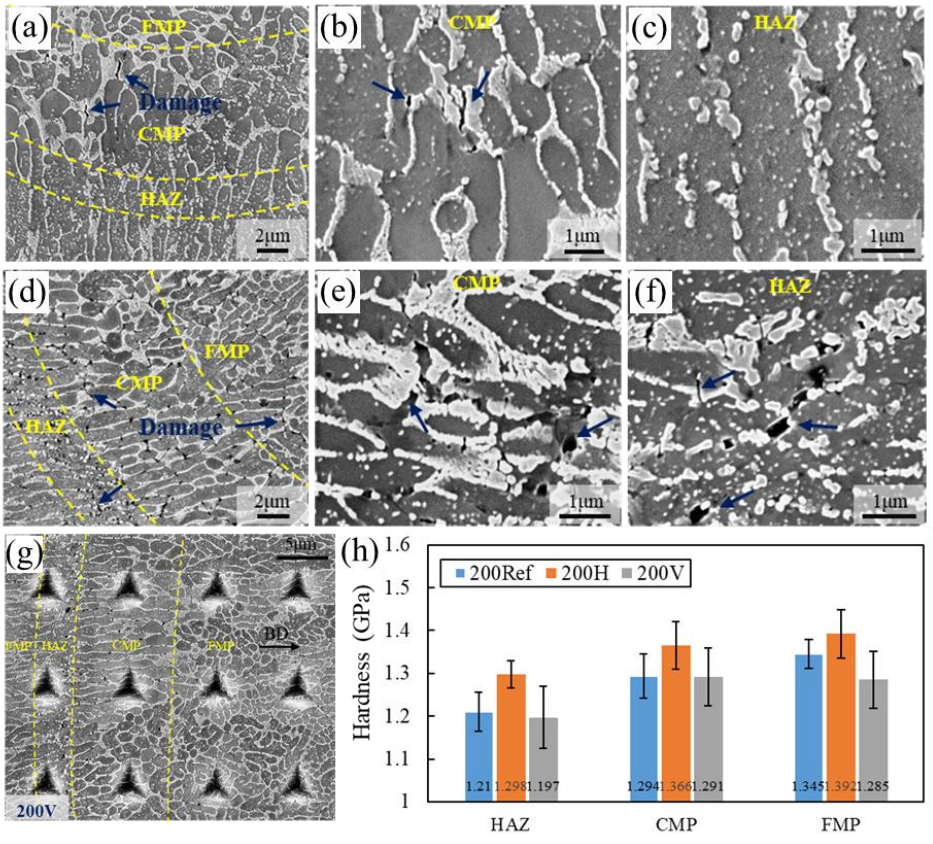

Fig. 33. Damage distribution in deformed horizontal (a)-(c) and vertical (d)-(f) specimens built on 200°C platform, corresponding nanoindentation on deformed microstructure (g) and hardness values in the FMP, CMP and HAZ before and after deformation (h) [171]. The specimens are unloaded at 96% and 94% of elongation to failure for the horizontal (200H) and vertical (200V) loading cases, respectively. 200 in (d) means 200°C build platform. The figures are reprinted with permission from Elsevier.

According to the analysis of Song et al. [171], damage behavior anisotropy may result from different load partitions (i.e., phase stress) in different loading directions, due to the elongated Si-rich network morphology. Therefore, phase stress characterization is necessary to understand LPBF AlSi10Mg damage behavior. Kim et al. [71] and Zhang et al. [44] have assessed the phase stress evolution of horizontal specimens by in situ neutron and X-ray diffraction tensile testing, respectively. However, experimental studies have yet to incorporate other loading directions. Numerical simulation can be an alternative tool for this endeavor, as will be discussed in section 7.

4.5.4 Anisotropy in ductility

Ductility of horizontal specimens is generally higher than that of vertical specimens at the same process parameters. The effect of initial porosity on ductility, as discussed in section 4.4.3, can partly explain the anisotropy in the presence of large lack of fusion defects. Sample-scale microstructure heterogeneity along the building direction was also found to account for the lower elongation of vertical specimens, as the coarser microstructure at the upper portion of the sample could promote strain localization [120].

When excluding the material defects and sample-scale heterogeneity, the key factor leading to the anisotropy involves damage competition between different melt pool zones, in other words the favorable fracture path. Zhao et al. [47] reported that crack propagated along the melt pool border of about 50% of the melt pools viewed on the mid-thickness plane for vertical specimens, while this proportion dropped to roughly 4% for horizontal ones. Clear evidences for the preferred crack propagation along the melt pool borders are presented in Fig. 34.

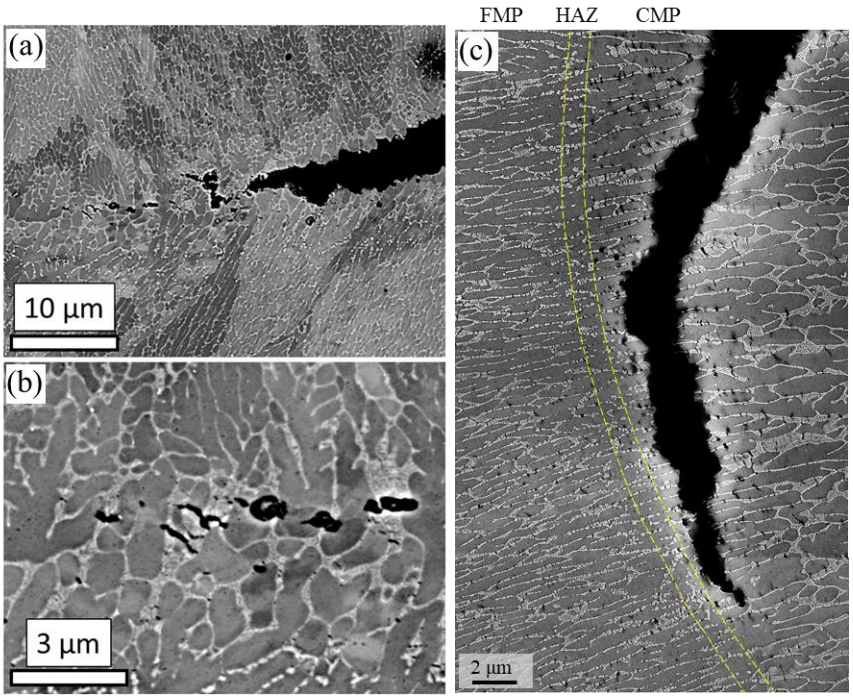

Fig. 34. Crack path along the melt pool border for vertical specimens. Damage distribution for materials presenting an elongation to fracture of roughly 5.2% [46] (a)-(b) and 9.4% [47] (c). (a) and (c) show a micro-crack along the melt pool border, (b) presents damage in the CMP zone. The figures

are reprinted with permission from Elsevier.

Many researchers attributed the lower ductility of vertical specimens to strain localization at the CMP [46], HAZ [45] or more generally the melt pool border [49, 62, 150], as it potentially leads to premature damage of vertical specimens. However, Song et al. [171] recently revealed that strain localization and even preferred crack propagation along melt pool borders did not remarkably compromise fracture strain of vertical specimens. This contradiction suggests that the underlying reasons for the anisotropy in ductility have not been brought to light yet. Further studies should address more in depth the damage sensitivity in and the damage competition between the three distinct zones (i.e., FMP, CMP and HAZ).

5. Fracture resistance

Fracture resistance, generally represented by fracture toughness, characterizes the resistance to the propagation of a pre-existing crack. It is a very important property in safety design of engineering structures. Fracture toughness is closely related to damage behavior and thus strongly depends on microstructure [164, 179]. There are only few studies on the fracture resistance of as built LPBF AlSi10Mg [188]. Nevertheless, basic trends can already be identified from previously reported data.

5.1 Fracture toughness

According to Pardoen and Hutchinson [164], the theoretical toughness measures the energy dissipation upon coalescence of the crack tip with the first void ahead of it. Toughness of metallic materials varies as a function of yield strength, strain hardening, initial porosity, void shape and spacing as well as void spacing anisotropy. Fracture toughness characterization should strictly respect small scale yielding condition at the crack tip, which normally requires a relatively large sample size to approach the plane strain state and a long sharp pre-crack to confine the plastic zone. E399 and E1820 are two widely used ASTM standards devoted to measure the K_{IC} and J_{IC}, with and without plastic dissipation, respectively.

The fracture toughness of cast Al-Si alloys is generally in the range of 20-30 MPa·m$^{1/2}$ [189, 190]. Paul et al. [49] reported a similar toughness variation range (19-30 MPa·m$^{1/2}$) for as built LPBF AlSi10Mg. Araújo et al. [123] calculated the fracture toughness with the critical crack tip opening distance (CTOD) and found a toughness range of 6.0-8.4 kJ·m^{-2}. Converting these values to stress intensity factors with $K_{IC} = \sqrt{(1-\nu^2) J_{IC} / E}$ (E is Young's modulus and ν is Poisson's ratio) yields approximately 28-33 MPa·m$^{1/2}$ (assuming E=70 GPa and $\nu = 0.3$) However, Hitzler et al. [48, 191] obtained much higher toughness, in the range of 40-60 MPa·m$^{1/2}$. These relatively high values are very likely due to the absence of fatigue pre-cracking prior to fracture toughness tests. Two trends are identified in the reported data:

(1) The fracture resistance presents a strong anisotropy. As can be noticed in Fig. 35, the toughness for the crack parallel to the building direction is much higher than that for the crack perpendicular to the building direction [48, 49, 123].

(2) The toughness highly depends on the scan strategy, whereas laser parameters have little influence. Fig. 35b shows that the rotation of 67° (67SS) between layers results in a higher toughness than the case with the rotation of 90° (90SS), despite similar material strength and ductility (refer to [49] for more details).

The anisotropy and the effect of the scan strategy on the fracture toughness are strongly related to the fracture path, as will be discussed in the following subsection.

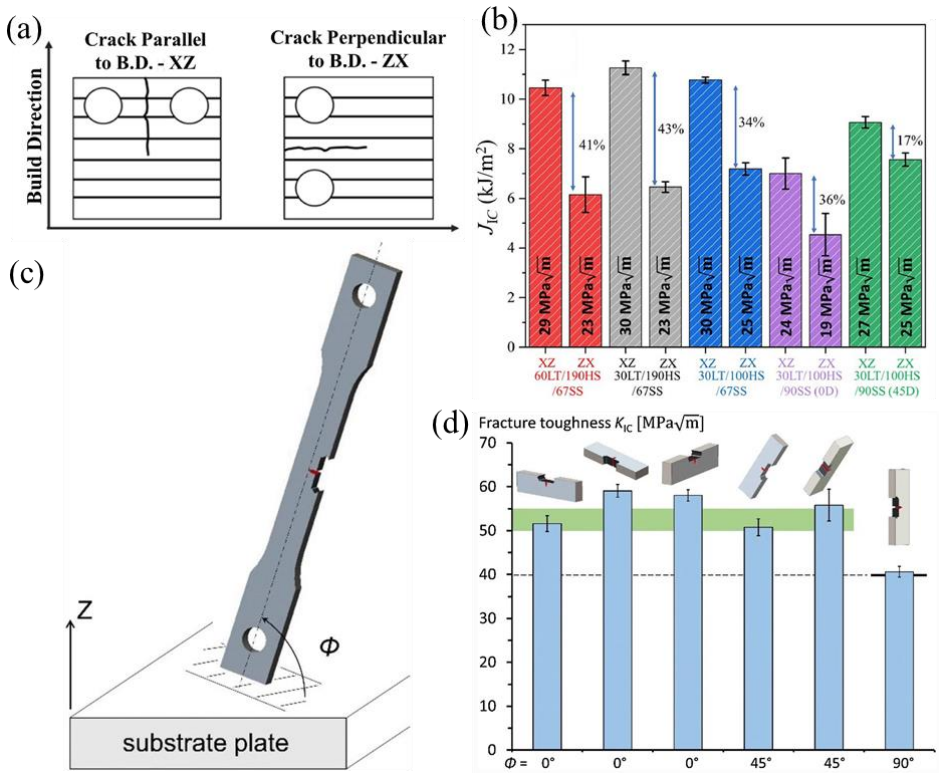

Fig. 35. Fracture toughness of as built LPBF AlSi10Mg as a function of process parameters and scan strategies. Tests with compact tension specimens incorporating fatigue induced pre-crack (a) and (b) [49], tests with single edge notched specimens without fatigue induced pre-crack (c) and (d) [48]. LT means layer thickness, HS hatch spacing, SS scan strategy in (b). The figures are reprinted with permission from Elsevier.

5.2 Fracture path

Fracture path (or crack propagation path) and its correlation with microstructure are important elements for understanding the fracture mechanism of metallic materials. It has been well recognized that a tortuous fracture path effectively increases the fracture toughness [192, 193] compared to a straight one.

The anisotropy of fracture toughness can be partly explained by the crack path tortuosity. Through specimen polishing to mid-section, Paul et al. [49] addressed the correlation between fracture path and the microstructure. As illustrated in Fig. 36a-c, the crack propagating parallel to the building direction mainly crosses the melt pools and presents a tortuous path induced by deflection at the melt pool borders. In contrast, when the crack propagates perpendicular to the

building direction, it mainly follows the melt pool borders, where the fracture resistance is expected to be lower (see Fig. 36d-f). Araújo et al. [123] have reported similar fracture paths for as built LPBF AlSi10Mg. The crack deflection level and difference of fracture resistance between the melt pool border and interior were believed to be responsible for the toughness anisotropy [49].

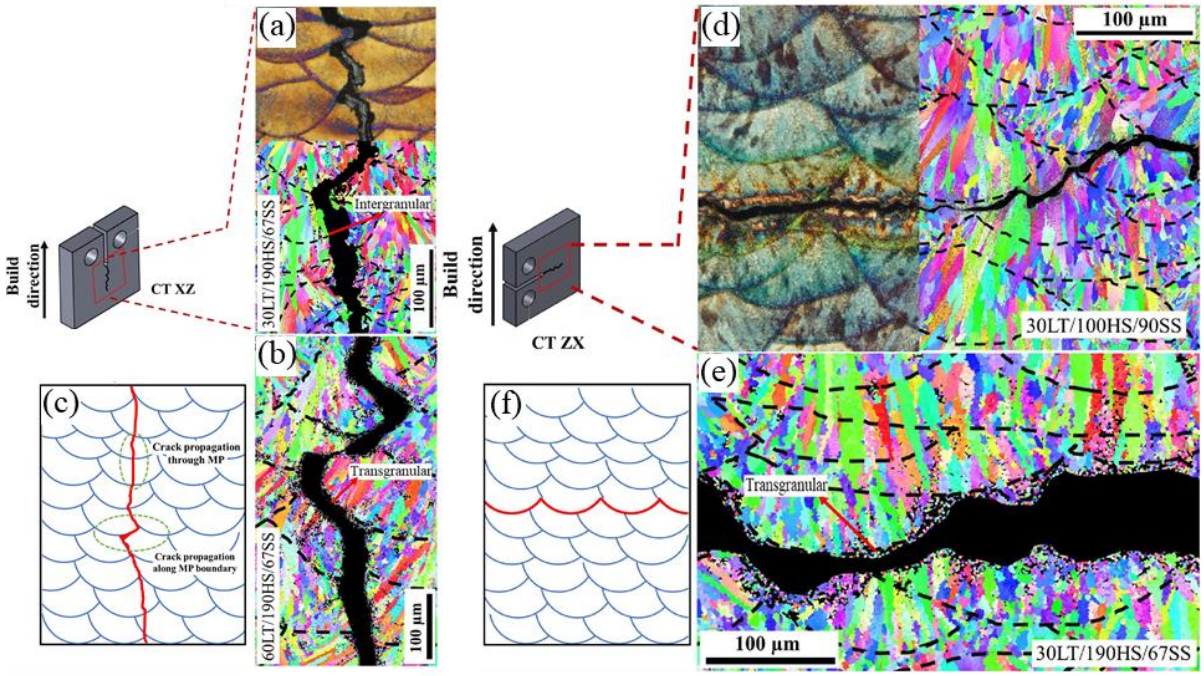

Fig. 36. Fracture path in pre-cracked compact tension specimens [49]. Observations of crack at specimen mid-sections with different process parameters (a), (b) for crack parallel to the building direction, and with different scan strategies (d), (e) for crack perpendicular to the building direction, schematic drawing illustrating the correlation between crack path and melt pool arrangements for crack propagating parallel (c) and perpendicular (f) to the building direction. The figures are reprinted with permission from Elsevier.

The dependence of fracture resistance on the scan strategy can be explained as follows [49]: the 67° rotation results in randomly distributed melt pools that promote more tortuous crack propagation through crack deflection and twisting; when employing the scan rotation of 90°, the crack propagates along the continuous melt pool boundaries without significant crack deflections, thus leading to an important decrease of toughness in both directions compared to

the 67° rotation case.

From the state of the art, it can be deduced that the melt pool arrangements play a vital role in the determination of fracture toughness of LPBF AlSi10Mg. Nevertheless, more fundamental research on the intrinsic fracture resistance of the three distinct zones (i.e., FMP, CMP and HAZ) is still lacking. To enhance the fracture resistance via optimizing the melt pool arrangements, such research gap should be filled in the future by, e.g., numerical simulations.

6. Fatigue resistance

Fatigue is the most frequent failure mode of engineering structures subjected to repeated loads. In concert with the demand on safety, a high fatigue resistance is generally required, especially for the aerospace field where additively manufactured metals present huge application potential. Fatigue resistance is known to be highly influenced by material defects, such as internal pores, inclusions and surface roughness that act as stress concentrators and promote fatigue crack nucleation [194, 195]. An important factor that limits the wide application of additively manufactured metals is the intrinsically formed porosity, which can be a few hundred microns large (see Fig. 17). The present review aims to summarize gained knowledge on fatigue resistance of as built LPBF AlSi10Mg, eventually through comparisons with post-treated counterparts to highlight the effects of initial porosity, yield strength and microstructure. For more general reviews on fatigue behavior of additively manufactured metals, readers can refer to Refs. [133, 188].

6.1 Fatigue life

Fatigue resistance is generally evaluated by the Wöhler (or S-N) curves, which illustrate the relationship between fatigue life and load level. According to loading cycles upon failure, fatigue can be categorized as low cycle fatigue (LCF), high cycle fatigue (HCF) and very high cycle fatigue (VHCF, also called ultra-high cycle fatigue). Very high cycle fatigue generally occurs at a stress level below the conventional fatigue strength and the relevant fatigue life is

longer than 10^7 loading cycles [196]. A key challenge for fatigue life assessment of additively manufactured metals is the large scatter of experimental data [197]. Fig. 37 presents several S-N curves for LPBF AlSi10Mg reported in literature, based on which the following critical factors determining fatigue life can be analyzed:

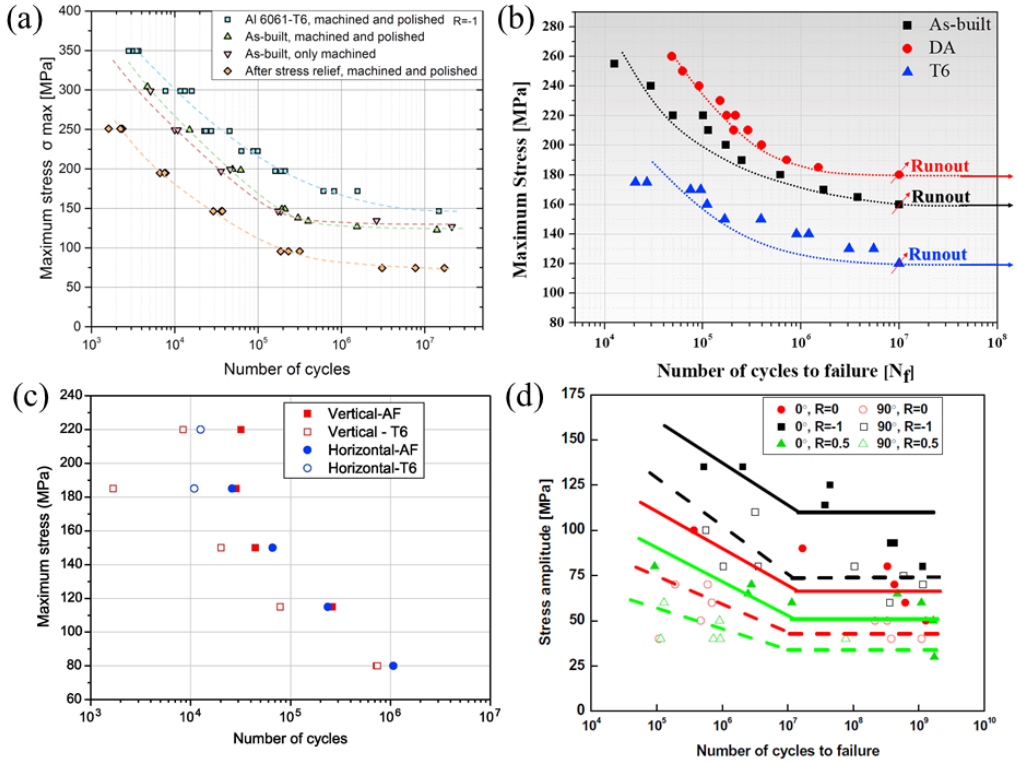

Fig. 37. Fatigue life of as built LPBF AlSi10Mg. Comparison with Al 6061-T6 and stress relief state [52] (a), comparison with direct aging and T6 states [198] (b), comparison between horizontal and vertical samples [65] (c), comparison between different stress ratios and loading directions [199] (d). DA means direct aging in (b), AF means as fabricated in (c), 0° and 90° correspond to horizontal and vertical samples, respectively, in (d). The figures are reprinted with permission from Elsevier.

(1) Effect of initial porosity. Uzan et al. [52] compared the fatigue life between wrought Al 6061-T6, as built and stress relieved (at 300°C for 2h) LPBF AlSi10Mg (Fig. 37a). They found that the Al 6061-T6 and stress relieved AlSi10Mg samples exhibited the highest and the lowest fatigue resistance, respectively. Note that in that study the Al 6061-T6 presents a slightly higher yield strength than the as built LPBF AlSi10Mg. Therefore, the reason for the better fatigue resistance of the Al 6061-T6 samples could be the absence of large porosity. Indeed,

Hannard et al. [187] showed that initial porosity in wrought 6XXX Al alloys was of the order of 0.1%, presenting an equivalent diameter generally smaller than 5 μm. In contrast, the initial pores can still reach a size of 50 μm even in sound as built LPBF AlSi10Mg presenting a low porosity of 0.13% [61]. Romano et al. [197] pointed out that pore size is the main cause of scatter in fatigue resistance of LPBF AlSi10Mg.

(2) Effect of yield strength. Regarding the stress relieved AlSi10Mg samples, the 300°C heat treatment generally reduces their yield strength but maintains the porosity level [61], therefore leading to a lower fatigue resistance compared to the as built state [57]. Indeed, a higher yield strength imparts a stronger fatigue resistance as local plasticity at defects can be effectively mitigated. Baek et al. [198] showed that the HCF life could be enhanced by a direct aging (DA) of as built LPBF AlSi10Mg, while it was significantly reduced by a T6 treatment (see Fig. 37b). The DA and T6 treatments increase and decrease the yield strength, respectively. Tridello et al. [200] showed that the stress relief heat treatment at 320°C also greatly reduced the lifetime under VHCF, due to a twofold yield strength decrease compared to the as built condition. It is worth mentioning that although hot isostatic pressing (HIP) has potential on porosity reduction, no success in extending fatigue life has been ever achieved on LPBF AlSi10Mg as the tried HIP parameters lead to a significant strength drop [201].

(3) Effect of loading direction. Larrosa et al. [65] compared the fatigue resistance of horizontal and vertical samples under machined and polished states. It was found that the vertical samples presented slightly lower fatigue life in the low to high cycle fatigue regime (lower than 10^6 cycles), as shown in Fig. 37c. A much more significant effect of loading direction was revealed by Qian et al. [199], covering a wide fatigue life range from 10^5 to 10^9 (i.e., VHCF) cycles and showing much better fatigue performance for horizontal samples (see Fig. 37d). The difference was considered to be induced by the orientation of the pores with respect to the loading direction, as flat lack of fusion defects are generally perpendicular to the

building direction (see Fig. 17c), therefore leading to higher stress concentrations at defects and promoting earlier fatigue crack initiation for vertical samples. This tendency seems to be maintained after T6 heat treatment [65] (see Fig. 37c) and stress relief heat treatment [34]. Surprisingly, Piette et al. [55] showed that the vertical samples presented longer lifetimes than the horizontal counterparts (see Fig. 37d) in the high to very high cycle fatigue regime (10^6-10^9 cycles). Nadot et al. [202] also obtained slightly longer fatigue lives for the vertical samples after T6 treatment. This abnormal behavior remained however unexplained.

6.2 Fatigue crack initiation

Fatigue crack initiation is a critical event in fatigue lifetime of metallic materials, especially for a high and very high cycle fatigue regime. Regarding LPBF AlSi10Mg, fatigue crack generally initiates on porosity (i.e., killer defect) [37, 50, 65, 118, 148]. Tang and Pistorius [203] demonstrated that oxide could also be critical crack initiation site.

Similar to damage mechanism investigation, fracture surface observation is also routinely performed to understand the fatigue crack initiation and propagation behaviors. Jian et al. [37] showed that the critical pores leading to fatigue failure were located either at the sample surface or in the sample interior, corresponding to HCF or VHCF regime, see Fig. 38a, b. Note that a defect is considered superficial when $a/h > 0.8$, where a and h denote the equivalent defect radius and the distance between the defect center and the external sample surface, respectively [204]. As the flat lack of fusion defects are preferentially oriented parallel to the horizontal plane (see Fig. 17c), the fatigue cracks typically present gouge-like and flat origins seen on the fracture surface for the horizontal and vertical samples, respectively (Fig. 38c, d). Unmelted powder can eventually be observed at the fatigue crack initiation sites [37, 50, 118].

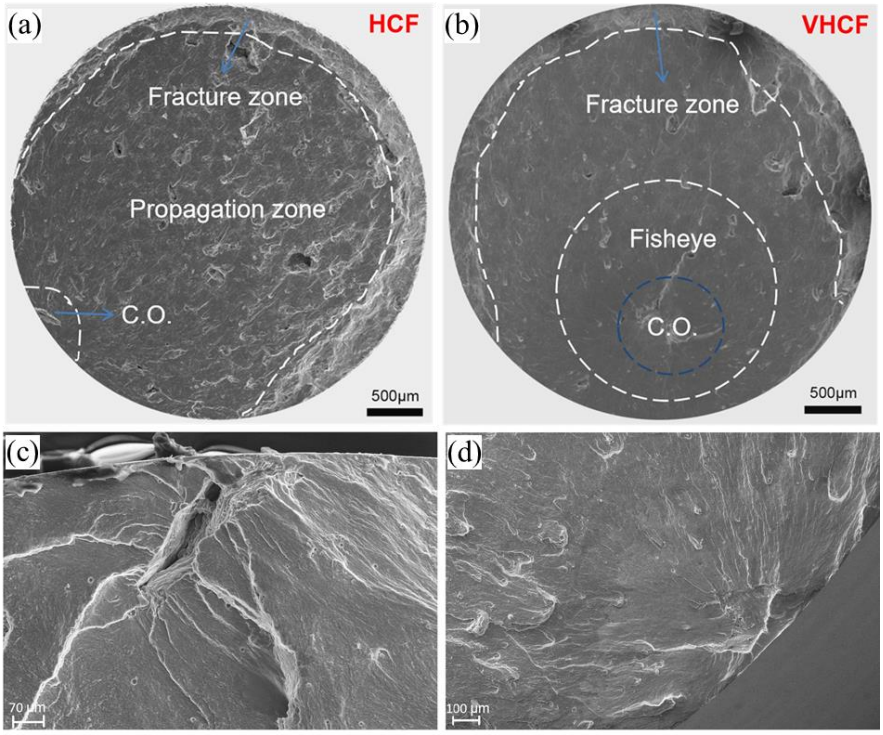

Fig. 38. Fatigue crack origins of as built LPBF AlSi10Mg samples. Surface porosity in high cycle fatigue with $N=2.74\times10^6$ (a), internal porosity in very high cycle fatigue with $N=4.48\times10^8$ [37] (b), typical manifestation of fracture origin (lack of fusion defects) for horizontal (c) and vertical (d) samples [118]. C.O. in (a) and (b) represents crack origin. The figures are reprinted with permission from Elsevier.

Why fatigue failure preferentially starts form surface pores in low and high cycle fatigue regimes? The driving force for the crack propagation is the stress intensity factor (SIF) range when treating the killer defects as short cracks. The SIF range depends on not only the defect size but also the defect location. Romano et al. [118] showed that, although the internal defects could be statistically larger, the stress intensity factor range was however higher for the surface defects due to a lower constraint. In contrast, the crack initiation generally occurs from internal or subsurface defects under VHCF, and the underlying mechanism is more complicated than that of HCF failure [205]. In fact, VHCF crack initiation is considered to be more closely related to local cyclic plastic deformation at microstructure inhomogeneities, such as defects. Recently, Li et al. [206] revealed a fine-granular-area (FGA) at the killer porosity of LPBF AlSi10Mg

under VHCF for a negative stress ratio. This indicates that grain refinement at the fatigue crack tip, a typical VHCF phenomenon, also exists in AM Al alloys. The FGA formation can be well explained by the numerous cyclic pressing (NCP) model proposed by Hong et al. [205], attributing grain refinement to localized intensive plastic deformation arising from repeated pressing between crack surfaces and a sufficient number of tension-compression loading cycles. From the abovementioned analysis, it could be deduced that the statistically larger internal defects would lead to more severe local plastic deformation and therefore become preferred crack initiation sites under VHCF. To prove this conjecture, micromechanical simulations need to be carried out.

It should be noted that fractographic analysis not only identifies the nature and position of the fatigue crack origin, but also provides information on killer porosity size. This allows validating statistical models to predict critical defect size, as will be discussed in section 6.4. Moreover, microstructure characterization beneath the fracture surface can also help to elucidate crack initiation mechanisms. This is particularly important for VHCF failure where crack initiation is the most critical event throughout fatigue life.

6.3 Fatigue crack growth

Fatigue crack growth (FCG) rate is also an important measure of fatigue resistance of metallic materials. Similar to the fracture toughness, the FCG rate is generally characterized with samples presenting sharp pre-cracks. Regarding the fatigue crack growth of LPBF AlSi10Mg, previous works mainly focused on the following two aspects:

(1) Effect of loading direction with respect to the melt pool border [55, 207]. Di Giovanni et al. [207] showed that, under the as built condition (with 67° rotation between layers as the scan strategy), the FCG rate was the highest when the crack plane was perpendicular to the building direction (i.e., Z-Y AB sample in Fig. 39, AB meaning as built). Interestingly, in the case where the crack plane was parallel to the building direction, the FCG rate also presented a

dependence on the crack propagation direction: the fatigue crack growth rate was lower when the propagation direction was perpendicular to the building direction (i.e., Y-X AB sample in Fig. 39) compared to the parallel case (i.e., Y-Z AB sample in Fig. 39). Moreover, for the Y-Z AB samples, the up-down or down-up propagation does not influence the FCG rate (Fig. 39b). The worst resistance to fatigue crack growth of the Z-Y AB sample was proposed to be induced by easy crack propagation along the weak HAZ zone (Fig. 39d). Similar observations have been reported by Piette et al. [55]. The difference between the Y-X and Y-Z samples was explained by residual stresses.

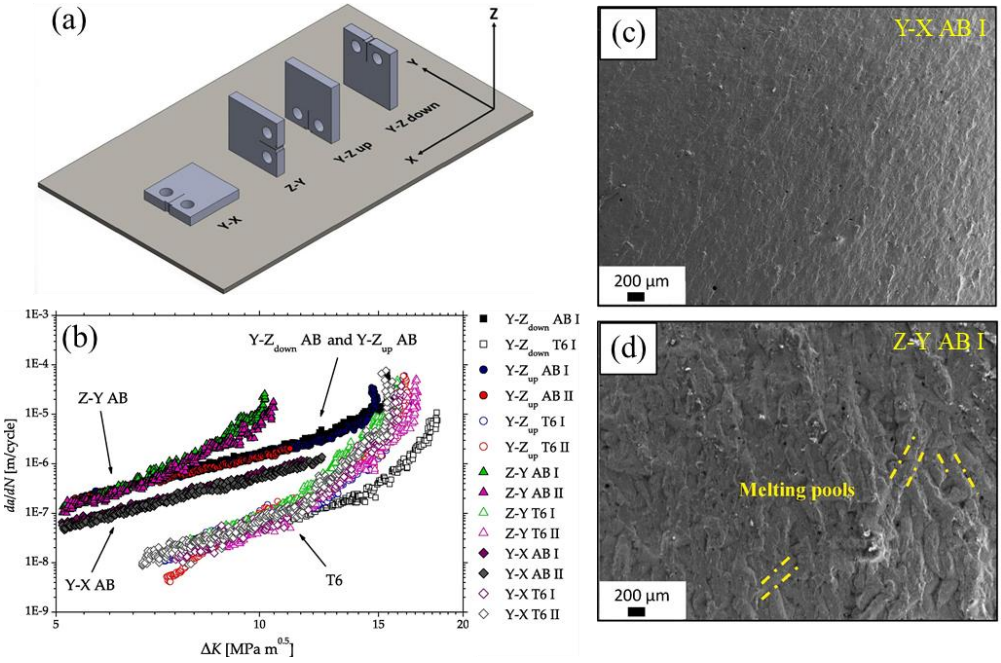

Fig. 39. Fatigue crack growth rate for different loading and notch directions [207]. Sample designation (a), experimental *da*/*dN* vs. Δ*K* curves (b), fracture surface morphologies of the samples with global crack plane parallel (c) and perpendicular (d) to the building direction. The figures are reprinted with permission from Elsevier.

(2) Comparison between as built and post-treated states [57, 207]. Post-treatments generally enhance the resistance to fatigue crack propagation. A T6 treatment could lower the fatigue crack growth rate by nearly ten times in the steady state regime [207] (see Fig. 39b). It was proposed that the reduction of FCG rate was due to more significant damage of the

microstructure consuming more energy during the crack propagation, compared to the as built state. Santos Macías et al. [57] also showed a FCG rate decrease by an order of magnitude after a stress relief heat treatment (SRHT, 300°C for 2h) or friction stir processing (FSP). They proposed two possible reasons for the improvement: i) increased plasticity induced crack closure for the SRHT and FSP; ii) enhanced crack branching in the FSP and SRHT samples.

It is worth mentioning that initial porosity could locally arrest the fatigue crack propagation by crack tip blunting, leading to a decrease of stress intensity factor [53]. However, as pores are dispersed in the sample volume, the crack front can only encounter very few pores, and crack arrest thus presents little effect on the global fatigue crack propagation process. Santos Macías et al. [57] also reached this conclusion, showing that the FCG rate was similar for the SRHT and FSP samples, though the latter presented a much lower porosity.

6.4 Fatigue strength and life prediction

Fatigue strength is generally regarded as the stress level corresponding to the asymptotic horizontal line in the S-N curve, usually in the HCF regime, whereas there is no real fatigue limit in the VHCF regime [208]. To predict the fatigue strength and fatigue life, a precise assessment of killer defects is indispensable. It should be noted that characterization of all defects in a large sample or structure is nearly impossible. Therefore, the probabilistic approach, performing X-ray computed tomography on some representative witness samples and applying statistics of extremes, becomes a popular tool to assess the killer defect size [118].

Extreme value statistics for defect evaluation was proposed more than 25 years ago, addressing the estimation of critical defect size for fatigue design. This approach has been recently adopted to assess the fatigue strength of additively manufactured metals [209]. Given that most fatigue failures start from the sample surface, Romano et al. [118] proposed to estimate the size of the maximum defects in an external circular crown (gauge volume) with a fixed thickness $h = \bar{a} / 0.8$ (see Fig. 40a), where $\bar{a}$ represents the average experimental radius

of the killers measured in the samples. It was demonstrated that the extreme value statistics for defects within the circular gauge volume led to reasonable prediction, as can be seen in Fig. 40b where the crosses represent the experimentally measured crack origin sizes and the blocks the predicted pore sizes.

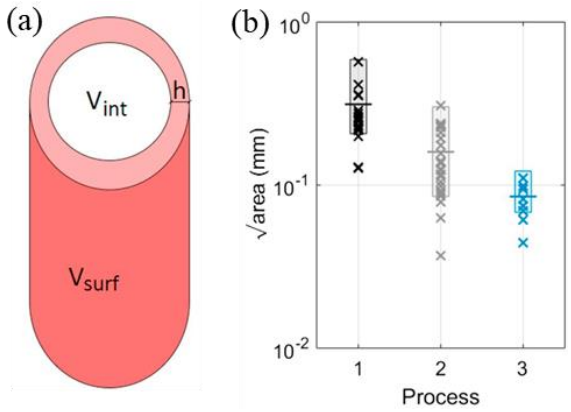

Fig. 40. Extreme value statistics for porosity of LPBF AlSi10Mg [118]. Schematic of gauge volume for surface defect size prediction (a), comparison between experimentally measured (crosses) and statistically predicted (blocks) killer defect size for different samples manufactured with different process parameters (b). The figures are reprinted with permission from Elsevier.

When the defect size is accurately assessed, the fatigue strength can be effectively predicted using models dedicated to fatigue resistance evaluation. The correlation between the defect size (i.e., Murakami's parameter expressed as $\sqrt{area}$ [210]) and the fatigue strength is generally described through the so-called Kitagawa-Takahashi diagram [211]. Beretta and Romano [212] showed that the wide scatter of the fatigue properties for AM metals could be significantly reduced when the data were correlated to the defect size at the failure origin through the Kitagawa-Takahashi diagram.

Romano et al. [118, 213] employed the Murakami-Endo [214] and El-Haddad models [215] to relate the fatigue strength to the critical defect size. After calibrating the model parameter with experimental data of LPBF AlSi10Mg, the authors predicted the fatigue strength of a bracket structure with the porosity size obtained from the extreme value statistics performed with partial tomography scans. However, no experimental validation of the prediction was

provided. Wu et al. [34] applied the same approach and estimated the fatigue limit of stress relieved LPBF AlSi10Mg. They demonstrated that the prediction error was within 10% for vertical samples, while it was over-conservative by about 35% for horizontal samples. Schneller et al. [216] proposed a fatigue strength prediction model that considered defect size, material hardness and residual stresses. They proved that the model, coupled with generalized extreme value distribution of defects, could accurately estimate the fatigue strength of as built and post-treated LPBF AlSi10Mg with respect to experimental measurements.

Regarding the fatigue life prediction, different approaches are used to treat LCF/HCF and VHCF issues. For the low and high cycle fatigue regimes, AM defects are generally treated as short cracks in order to be able to calculate the stress intensity factor, which in turn allows fatigue crack growth assessment. Romano et al. [118, 197] employed a NASGRO-type equation to describe the ΔK-da/dN relationship for as built LPBF AlSi10Mg, accounting for a plasticity-corrected crack length for calculating ΔK. The fatigue life is counted until the instantaneous fracture condition ($K_{Imax}=K_{IC}$) is met. The authors demonstrated that the predicted fatigue lives were very close to the experimental results, especially when the smallest, average and largest defect sizes were considered to assess the scatter of the data. Qian et al. [217] studied multiple defect induced fatigue crack growth in stress relieved LPBF AlSi10Mg. They performed the fatigue life prediction with the NASGRO-type equation and considered the influence of crack coalescence. The authors finally showed that the multiple crack growth model predicted a shorter propagation life (i.e., more conservative) than the single crack model when multiple defects were involved, especially in the case of large stress amplitudes. Concerning fatigue life prediction under VHCF, very few works on LPBF AlSi10Mg can be found in literature. The fracture mechanics based approach might be inappropriate due to the challenge of crack propagation modeling in stage I (for example crack propagation within the FGA). However, this critical stage can occupy more than 90% of fatigue life under VHCF [218]. Recently, Zhang

et al. [219] assessed VHCF lifetime of LPBF AlSi10Mg with a fatigue indicator parameter (FIP), defined as either increment of cumulative plastic strain or product of maximum tensile stress and elastic strain amplitude around the killer defect (i.e., porosity). They showed that the prediction of fatigue life with the plastic strain based FIP is in good agreement with experimental results. This result in turn confirms that crack initiation and early propagation are more closely related to local plastic deformation rather than stress intensity factor for VHCF failure, as previously stated in section 6.2.

From the state of the art, it can be concluded that porosity and mechanical strength are the two predominant factors determining the fatigue resistance of LPBF AlSi10Mg. To enhance the fatigue performance, a lower porosity and a higher yield strength are required. This necessitates further manufacturing process optimization, given that such improvement seems to be hardly achieved by post-treatments (e.g., stress relief heat treatment, HIP, T6, friction stir processing).

7. Modeling and simulation of plastic behavior

Modeling and simulation are efficient tools to predict or understand mechanical response at different scales. They can help to address the strengthening, hardening and even damage mechanisms of metallic materials. Compared to the experimental campaign on additively manufactured metals, much less efforts have been devoted to modeling and simulation up to now. Nevertheless, there is a growing trend of performing micromechanics and multi-scale modeling of LPBF AlSi10Mg in literature, mainly focused on plastic deformation behavior.

7.1 Micromechanics modeling and simulation

As LPBF AlSi10Mg presents a complex microstructure, conventional J_2 plastic model may not be able to accurately predict its deformation behavior. In contrast, micromechanics modeling takes into account microstructure features and basic plastic deformation mechanisms, and is therefore the ideal method for addressing the mechanical response of LPBF AlSi10Mg [178, 185, 220, 221].

7.1.1 Two-phase microstructure-based crystal plasticity modeling

Considering the difference of mechanical properties between the Al cells and the Si-rich eutectic, explicit modeling of both constituents allows to address their load partition and contribution to macroscopic flow stress. Kim et al. [178] and Zhang et al. [185] adopted the following modeling strategy: the Al cells are treated with a phenomenological crystal plasticity model and the Si-rich eutectic is simplified as Si particles with a specific aspect ratio (see Fig. 41a). Concerning the crystal plasticity model, the finite strain framework is generally adopted, in which the deformation gradient is decomposed into elastic part $\boldsymbol{F}^{\mathrm{e}}$ and plastic part $\boldsymbol{F}^{\mathrm{p}}$

$$\boldsymbol{F} = \boldsymbol{F}^{e}\boldsymbol{F}^{p} \tag{9}$$

The second Piola-Kirchhoff stress $\boldsymbol{S}$ is calculated by

$$\boldsymbol{S} = \boldsymbol{C} : \boldsymbol{E}^{e} \tag{10}$$

where $\boldsymbol{C}$ is the stiffness tensor and $\boldsymbol{E}^{\mathrm{e}}$ the Green strain $\boldsymbol{E}^{\mathrm{e}}=[(\boldsymbol{F}^{\mathrm{e}})^{\mathrm{T}}\,\boldsymbol{F}^{\mathrm{e}}-\boldsymbol{I}]/2$ ($\boldsymbol{I}$ is the identity tensor).

According to the kinematics of dislocation slip, the plasticity velocity gradient $\boldsymbol{L}^{\mathrm{p}}$ is related to the slip rate through

$$\boldsymbol{L}^{p} = \dot{\boldsymbol{F}}^{p}\boldsymbol{F}^{p-1} = \sum_{\alpha}\dot{\gamma}^{\alpha}(\boldsymbol{s}^{\alpha}\otimes\boldsymbol{m}^{\alpha})_{\mathrm{sym}} \tag{11}$$

where $\dot{\gamma}^{\alpha}$ is the slip rate of slip system α and $\boldsymbol{s}^{\alpha}$ and $\boldsymbol{m}^{\alpha}$ the slip direction vector and slip plane normal vector, respectively.

The slip rate is determined by the resolved shear stress τ^{α} and the critical threshold controlling the strain hardening (i.e., current strength of the slip system) g^{α} as follows

$$\dot{\gamma}^{\alpha} = \dot{\gamma}_{0}\left|\frac{\tau^{\alpha}}{g^{\alpha}}\right|^{m} sign(\tau^{\alpha}) \tag{12}$$

where $\dot{\gamma}_{0}$ is the reference strain rate, m denotes the strain rate sensitivity exponent, g^{α} contains self-hardening and latent hardening components governed by

$$\dot{g}^{\alpha} = \sum_{\beta} h^{\alpha\beta}\dot{\gamma}^{\beta} \tag{13}$$

where $h^{\alpha\beta}$ are the hardening moduli, with $h^{\alpha\alpha}$ representing the self-hardening and $h^{\alpha\beta}$ ($\alpha \neq \beta$) representing the latent hardening.

Different evolution models for the hardening moduli exist. Kim et al. [178] and Zhang et al. [185] adopted the following hardening law proposed by [222]

$$h^{\alpha\beta} = q^{\alpha\beta} h_0 (1 - \frac{\tau_0^{\alpha}}{\tau_{\text{sat}}})^a \tag{14}$$

where h_0, a, τ_{sat} and τ_0^{α} (i.e., initial slip resistance) are the hardening parameters that should be determined with experimental data, $q^{\alpha\beta}$ is a constant, which is usually assumed to be 1 considering isotropic hardening only.

The aforementioned model allows to consider the dependence of dislocation slip (i.e., plastic deformation) on grain orientation and can be used to describe the deformation behavior of the Al cells. Concerning the treatment of the Si-rich eutectic, different strategies have however been used in different studies. Kim et al. [178] and Li et al. [182] adopted the same constitutive model to the Al cells and the Si-rich eutectic with different parameters. In contrast, Zhang et al. [185] treated the Si-rich eutectic as an elastic material. It should be noted that both treatments lack direct experimental support. Although several stacking faults and shear steps were observed in the Si-rich eutectic of deformed LPBF AlSi10Mg [178], to which degree the Si-rich eutectic could plastically deform remains unclear.

Albeit the Si-rich eutectic is treated differently, after fitting the parameters with experimental data, both strategies were proved to be able to reasonably predict the phase strain or stress. Fig. 41 shows the results obtained with elastic Si-rich eutectic [185]. It can be noticed that the predicted volume average phase stresses match very well with the measurements by X-ray diffraction (see Fig. 41d). Moreover, the simulations allow to assess the stress distribution within the Al matrix (Fig. 41b) and the Si-rich eutectic (Fig. 41c), which are beyond the capacity of experimental characterization.

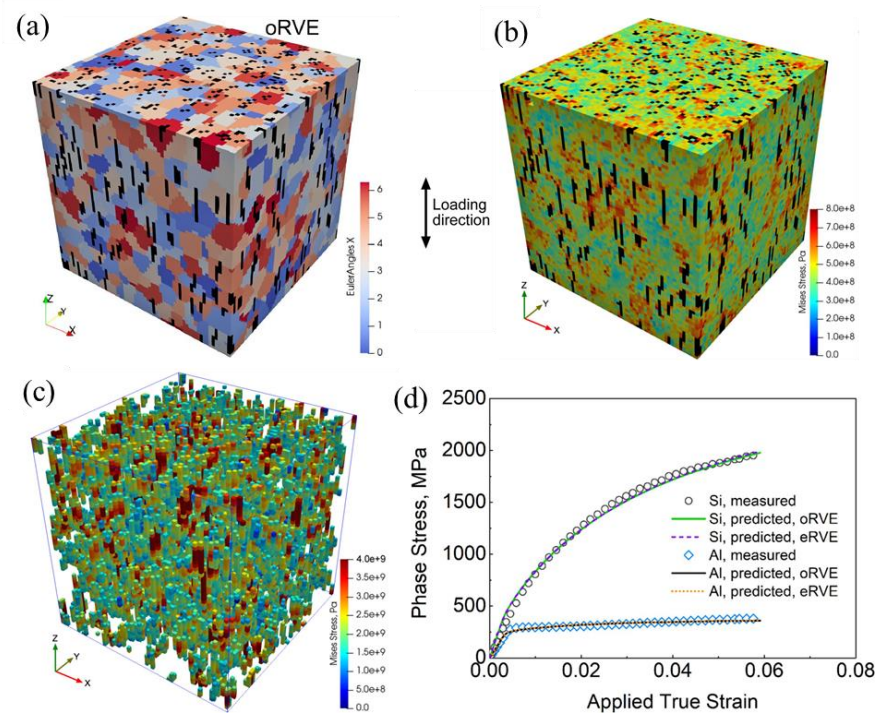

Fig. 41. Modeling and simulations of microstructure incorporating α-Al grains and Si-rich eutectic by crystal plasticity [185]. Optimized representative volume element (oRVE) (a), predicted von Mises stress distributions in Al (b) and Si (c) at the applied strain of 5.6%, comparison between measured and predicted phase stress as a function of applied true strain (d). In (a) and (b), the Si particles are shown in black color. The figures are reprinted with permission from Elsevier.

In fact, through parameter fitting, it is generally possible to reproduce experimental measurements with modeling and simulations. Nevertheless, a physically sound model should present a good transferability, i.e., the ability to be extended to other samples built with different LPBF parameters. In this sense, the deformation mechanism of the Si-rich eutectic should be further clarified to guide the micromechanics modeling. This might be achieved by sophisticated TEM characterization or by atomistic simulations (e.g., molecular dynamics), as will be discussed in section 8.5.

7.1.2 Homogeneous crystal plasticity modeling

The modeling strategy (i.e., explicit consideration of two phases) mentioned in section 7.1.1 can hardly handle the whole microstructure due to the scale gap between the Al cell and melt

pool hierarchies. In order to consider the macroscopic deformation behavior of the material, the microstructure needs to be treated as homogeneous. Such treatment allows to build a RVE containing several melt pools.

A representative work on homogeneous crystal plasticity modeling of LPBF AlSi10Mg has been conducted by Romanova et al. [221]. The crystal plasticity model in that work adopted the small strain framework, with the flow strength expressed by

$$g^{\alpha} = \tau_0^{\alpha} + k_1 D_i^{-1/2} + k_2 \left\langle d \right\rangle^{-1/2} + f(\varepsilon_{eq}^{p}) \tag{15}$$

where the first term of the right side τ_0^{α} denotes the initial critical resolved shear stress of the slip system α for pure Al, the second term represents the grain boundary strengthening, i.e., the Hall-Petch effect with D_i denoting the diameter of the ith grain, the third term accounts for the strengthening induced by the Si-rich network with $\left\langle d \right\rangle$ denoting the average Al cell size and k_2 the fitting parameter and the fourth term depicts the strain hardening as a function of accumulated equivalent plastic strain

$$f(\varepsilon_{eq}^{p}) = a_1(1-\exp(-a_2\varepsilon_{eq}^{p})) + b_1(1-\exp(-b_2\varepsilon_{eq}^{p})) \tag{16}$$

where a_1, a_2, b_1 and b_2 are fitting parameters.

The RVE model constructed by Romanova et al. [221] was achieved using the step-by-step packing method [223]. As shown in Fig. 42a, the model incorporates quite realistic columnar grains inside the melt pools and equiaxed grains at the melt pool borders. Such model can be used to study the mechanical response along different loading directions (see Fig. 42b-d). Moreover, the simulation results allow to assess stress and strain distributions between different melt pool zones, which are important elements for understanding the damage and fracture behaviors of LPBF AlSi10Mg.

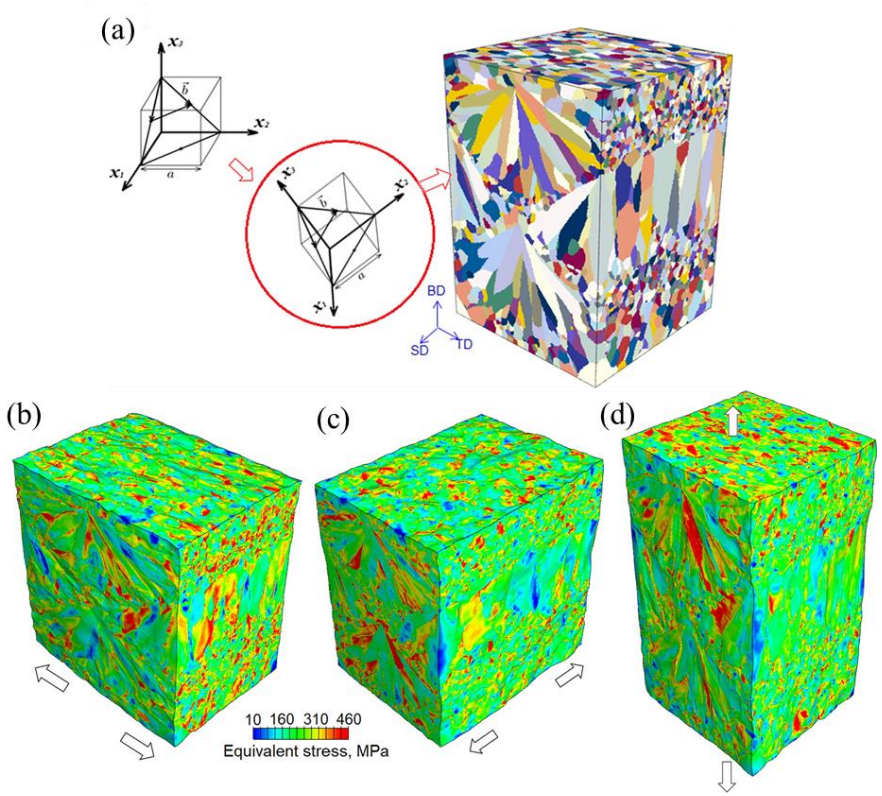

Fig. 42. Modeling and simulation of melt pool hierarchy RVE [221]. Polycrystal model of LPBF generated by step-by-step packing method (a), crystal plasticity finite element simulations in different loading directions (b)-(d). The figures are reprinted with permission from Elsevier.

7.2 Multi-scale modeling and simulation

The trans-scale and heterogeneous microstructure features of LPBF AlSi10Mg necessitates a multi-scale modeling framework to quantitatively build the link between the microstructure and the macroscopic mechanical behavior. Such frameworks are emerging in literature. The present review article will present two strategies recently proposed by Zhang et al. [224] and Li et al. [182].

7.2.1 Multi-scale Kocks-Mecking modeling

Zhang et al. [224] described the constitutive relation for LPBF AlSi10Mg with multi-scale Kocks-Mecking (K-M) models. At the microscale, the Al cells and Si-rich eutectic were treated separately, and the assumption of iso-strain, i.e., the plastic strain of Al cells is equal to the macro plastic strain of the tested specimen, was adopted. Therefore, the total stress of the

material can be calculated through linear summation of phase stresses as follows

$$\sigma_{\text{total}} = f_{\text{Al}}\sigma_{\text{Al}} + f_{\text{Si}}\sigma_{\text{Si}} \tag{17}$$

where f_{Al} and f_{Si} represent the volume fraction of the Al phase and Si-rich eutectic, respectively. This composite model has been shown to provide quite accurate predictions for LPBF AlSi10Mg [44].

In the framework of K-M model, both the flow stress and plastic deformation are related to dislocations. The flow stress in the Al phase (i.e., Al cells) can be determined using the Taylor hardening model [225]

$$\sigma_{\text{Al}} = \sigma_0 + M\alpha\mu b\sqrt{\rho} \tag{18}$$

where σ_0 is the friction stress, M the Taylor factor, α the Taylor hardening coefficient, μ the shear modulus, b the magnitude of the Burger's vector and ρ the dislocation density.

The evolution of the total dislocation density ($d\rho/d\varepsilon_p$) in the Al cells can be decomposed into the storage ($d\rho^+/d\varepsilon_p$) and dynamic recovery ($d\rho^-/d\varepsilon_p$) parts

$$\frac{d\rho}{d\varepsilon_p} = \frac{d\rho^+}{d\varepsilon_p} - \frac{d\rho^-}{d\varepsilon_p} = M\left(\frac{1}{bL} - l_2\rho\right) \tag{19}$$

where L is the mean free path of dislocation slip and l_2 a material constant. As L is expressed as $l_1/\sqrt{\rho}$ with l_1 being a material constant, the above equation can be further developed into

$$\frac{d\rho}{d\varepsilon_p} = k_1\sqrt{\rho} - k_2\rho \tag{20}$$

with two material parameters $k_1=M/(l_1 b)$ and $k_2=Ml_2$ which depend on the material microstructure.

As the iso-strain assumption was adopted, the dislocation density evolution can therefore be well determined with macro plastic strain. Since both flow stress and plastic deformation are related to dislocation density, the relationship between phase stress and plastic deformation can finally be established by the following law initially suggested by Voce [226] and then well

interpreted by the K-M model [227]

$$\sigma = \sigma_s - (\sigma_s - \sigma_i)\exp[-n_c(\varepsilon_p - \varepsilon_i)] \tag{21}$$

where σ_s denotes the saturation stress, σ_i and ε_i the true stress and strain upon the occurrence of plastic deformation (ε_i can generally be considered as 0) and n_c is a characteristic factor which can be related to k_2 ($n_c = k_2 / 2$) according to the K-M model.

With X-ray diffraction in situ tensile tests, Zhang et al. [44, 224] obtained the dislocation density evolution (Fig. 43a) and phase stress evolutions, based on which the two material parameters k_1 and k_2 were calibrated (Fig. 43b). It has been found that the dislocation density evolution involves three stages: stage A, where the dislocation density in the Al matrix increases quickly with a weak strain hardening effect; stages B and C, where the dislocation density increases slowly but with a more substantial strain hardening effect. This multistage strain hardening behavior of the Al phase is induced by the Si-rich network which imposes strong constraints on the dislocation motions [44]. In stage A, most dislocations are trapped within the Al cells. The interactions between dislocations from adjacent cells are suppressed, leading to a small forest dislocations hardening effect. With plastic strain increase, the total dislocation density becomes higher and approaches the saturated value. Therefore, the mutual interactions between dislocations become stronger and lead to a dramatic strain hardening effect in stage C, with stage B being a transition stage.

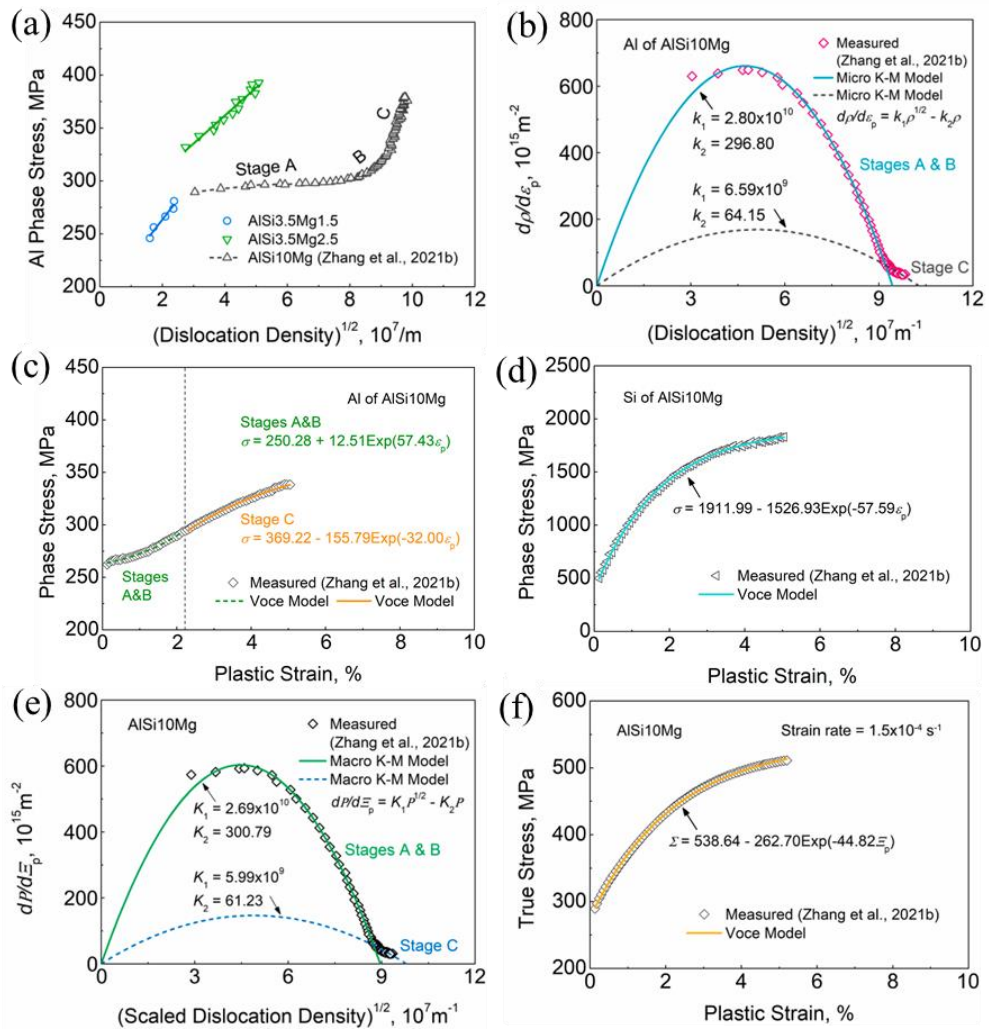

Fig. 43. Multi-scale K-M modeling of LPBF AlSi10Mg [224]. Al phase stress versus square root of dislocation density measured by X-ray diffraction (a), microscale K-M model fitting of dislocation density evolution rate (b), microscale Voce model fitting for the Al phase (c), microscale Voce model fitting for the Si-rich eutectic (d), macroscale K-M model fitting of scaled dislocation density evolution rate (e), macroscale Voce model fitting for homogenized AlSi10Mg (f). The figures are reprinted with permission from Elsevier.

Correspondingly, two sets of k_1 and k_2 are needed to fit the dislocation density evolution, as shown in Fig. 43b. Moreover, due to the constraint effect of the Si-rich network on dislocation interaction, the n_c parameter significantly deviates from $k_2/2$ in stage A when fitting the Al phase stress with the Voce hardening law, as can be noticed in Fig. 43c.

Concerning the Si phase at the microscale, the authors proposed that the high stress in this

stiff constituent was due to stored dislocation at the Al/Si interface, leading to stress concentration. The evolutionary average stress in the Si-rich eutectic is therefore assumed to be dominated by the dislocation density in the Al cells, which is further related to the plastic deformation of the Al matrix. Zhang et al. [224] showed that the stress of Si-rich eutectic could also be well predicted by the Voce law, see Fig. 43d. The Voce model therefore links the evolutionary stress of the Si-rich eutectic with the plastic deformation of the Al matrix.

At the macroscale, AlSi10Mg is treated as homogeneous. The macroscale K-M models are also developed based on the scaled dislocation density P, which is defined by the integral equality

$$P\int_{V} dV = \rho \int_{V_{\mathrm{Al}}} dv \tag{22}$$

where V is a defined volume of the alloy, and V_{Al} is the Al volume within V. Therefore, $P = \rho V_{\mathrm{Al}}/V = \rho f_{\mathrm{Al}}$.

Then, the macroscale K-M model can be defined as

$$\frac{dP}{d\Xi_p} = K_1\sqrt{P} - K_2 P \tag{23}$$

where K_1 and K_2 are material constants accounting for the scaled dislocation storage and annihilation processes.

Correspondingly, the macroscale Voce hardening law can be defined as

$$\Sigma = \Sigma_s - (\Sigma_s - \Sigma_0)\exp(-N_c\Xi_p) \tag{24}$$

where the macroscopic stress Σ equals the applied true stress, Σ_s the macroscale saturation stress, Σ_0 the macroscale yield strength, N_c the macroscale characteristic factor, and Ξ_p the macroscale plastic strain.

It is found that evolution of the scaled dislocation density can be well predicted by the macroscale K-M model (Fig. 43e), and the relation between the macroscopic stress and plastic

strain can be well captured by the macroscale Voce model (Fig. 43f). However, due to the fact that the macroscopic behavior is influenced by both the Al cells and the Si-rich eutectic, N_c is different from either $k_2/2$ or $K_2/2$.

From the aforementioned results, it can be concluded that the K-M model cannot fully describe the plastic deformation behavior of LPBF AlSi10Mg at either the microscale or the macroscale. The mechanism behind the K-M model is multiplication, annihilation and interaction of statistically stored dislocations. Therefore, the effects of precipitation hardening, solid solution hardening and eventually GND hardening are omitted in the K-M model. Nevertheless, these mechanisms might also significantly contribute to macroscopic hardening, leading to the deviation of n_c from $k_2/2$ in the stages A and B.

7.2.2 Microstructure-based multi-scale modeling and homogenization

Recently, Li et al. [182] proposed a microstructure-based multi-scale modeling framework, which accounts for the trans-scale, hierarchical and heterogeneous microstructure of LPBF AlSi10Mg. Two homogenization treatments were conducted to bridge the scale gaps, allowing to assess the macroscopic behavior of the material. This framework can be considered the most advanced and complete modeling strategy for handling the plastic deformation behavior of AM Al alloys, in particular the strength anisotropy, in the current state of the art. The modeling flowchart is illustrated in Fig. 44.

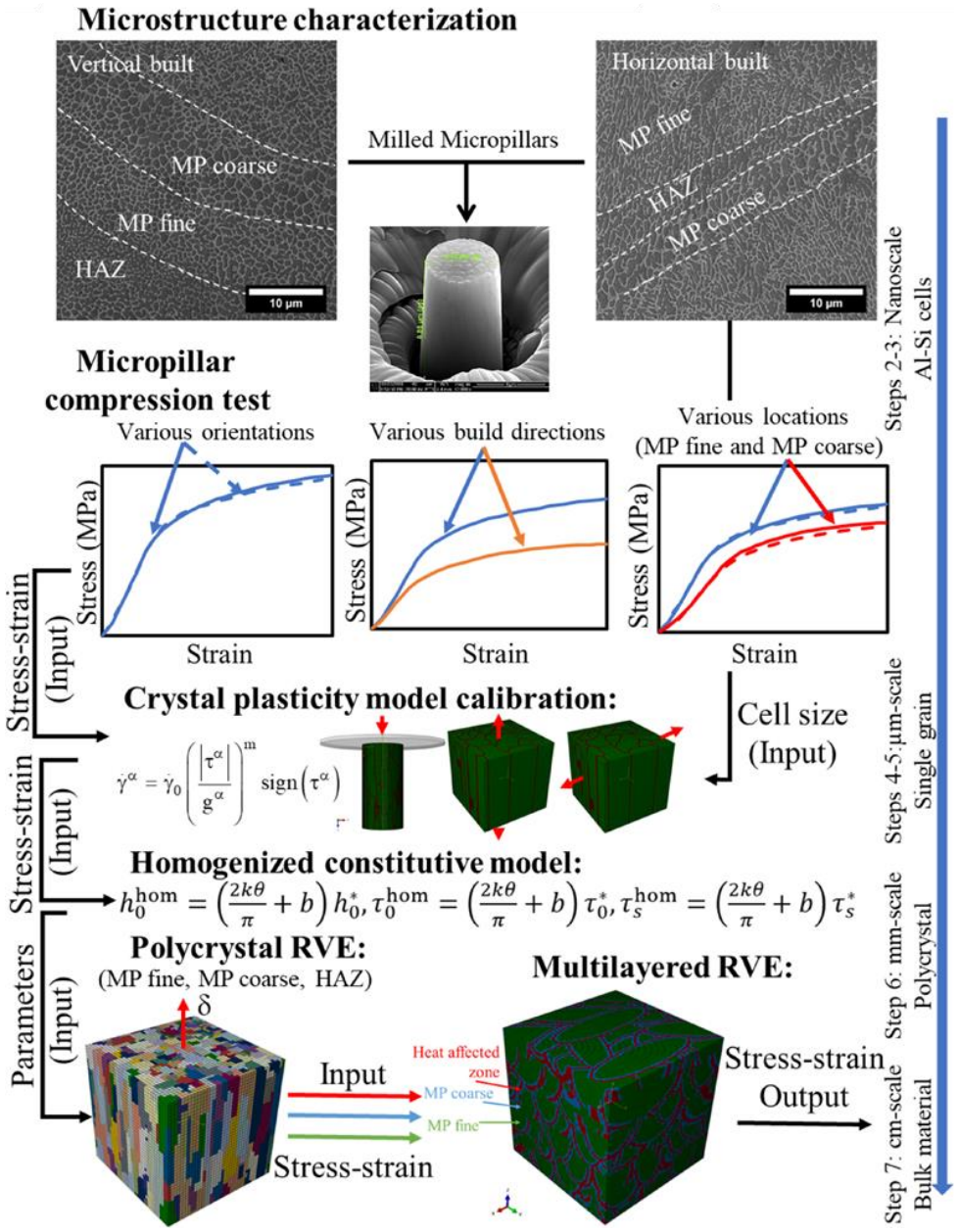

Fig. 44. Microstructure based multi-scale crystal plasticity modeling scheme of LPBF AlSi10Mg [182]. The figures are reproduced with permission from Elsevier.

At the microscale, a multi-phase crystal plasticity model was employed considering both the Al cells and the Si-rich network as elastoplastic materials, similarly to the treatment by Kim et al. [178]. The crystal plasticity model is the same as presented in section 7.1.1, except for the hardening moduli evolution part. The authors adopted the model proposed by Peirce et al. [228], where the self-hardening component reads

$$h_{\alpha\alpha} = h_0 \operatorname{sech}^2 \left| \frac{h_0 \gamma}{\tau_{\text{sat}} - \tau_0^{\alpha}} \right| \text{ (no sum over } \alpha) \tag{25}$$

where h_0 is the initial hardening modulus, τ_0^{α} the initial critical resolved shear stress of the slip system α , τ_{sat} the saturated flow stress and γ the sum of the shear strains on all slip systems at the current instant. The latent hardening component is given by

$$h_{\alpha\beta} = q h_{\alpha\alpha} \ (\alpha \neq \beta) \tag{26}$$

where q is a constant with a range of 1.0-1.4 and was taken as 1.0 for isotropic hardening by Li et al. [182]. The involved model parameters (h_0 , τ_0^{α} and τ_{sat}) were calibrated with the micropillar compression tests (see Fig. 44). The calibrated model was shown to successfully predict the mechanical behavior for different structure finenesses (i.e., FMP and CMP) and different loading directions (i.e., horizontal and vertical specimens). The microscale experiments and simulations suggest that the anisotropic flow behavior of LPBF AlSi10Mg is mainly induced by the orientation of the Si-rich network rather than the grain orientations [182].

In order to reduce the computational cost of simulations at the mesoscale (i.e., melt pool hierarchy), the collective behavior of the Al cells and Si-rich network was described by a computational homogenization scheme that was based on the same crystal plasticity model as for the microscale while using different material parameters h_0^{hom} , τ_0^{hom} and $\tau_{\text{sat}}^{\text{hom}}$

$$\begin{aligned} h_0^{\text{hom}} &= \left(\frac{2\text{k}\theta}{\pi} + \text{b} \right) h_0^* \\ \tau_0^{\text{hom}} &= \left(\frac{2\text{k}\theta}{\pi} + \text{b} \right) \tau_0^* \\ \tau_{\text{sat}}^{\text{hom}} &= \left(\frac{2\text{k}\theta}{\pi} + \text{b} \right) \tau_{\text{sat}}^* \end{aligned} \tag{27}$$

where $h_0^*, \tau_0^*, \tau_{\text{sat}}^*$, k and b are materials constants, and θ the angle between the long axis of the Si-rich network and the maximum principal stress direction, which is in the range of

$[0,\ \pi/2]$. The coefficient $2k\theta/\pi+b$ was introduced to capture the effect of the Si network orientation, as the yield strength and ultimate tensile strength of horizontal, diagonal and vertical specimens exhibited approximately a linear dependence on θ in macroscopic uniaxial tensile tests. The term $2/\pi$ was used to normalize θ to be in the range of [0, 1], and k and b were used to enforce the linear relation. Therefore, the introduction of $2k\theta/\pi+b$ allows to account for the Si-rich network orientation induced anisotropy.

The five parameters (h_0^*, τ_0^*, τ_{sat}^*, k and b) were calibrated with 3D RVE simulations using the microscale crystal plasticity model (see Fig. 44). It should be noted that when homogenizing the microstructure, the collective behavior depends on the size and volume fraction of the Si-rich eutectic. These two features were related to the Al cell size. To take this information into account, two sets of parameters were first obtained, corresponding to the Al cell sizes of 0.5 μm (FMP) and 1 μm (CMP), respectively. Then, linear interpolation and extrapolation were used for other Al cell sizes. In particular, the HAZ was considered to present globular Si particles, which do not involve characteristic orientation. Therefore, the collective behavior of the HAZ structure was described by an isotropic crystal plasticity model without $2k\theta/\pi+b$.

After achieving the homogenized models and corresponding material parameters, the mechanical behaviors of polycrystals in the FMP, CMP and HAZ were assessed with polycrystalline RVEs (see Fig. 44). To account for the Al cell size variation among grains, a normal distribution of cell diameter was first obtained and then random values of cell diameters generated by the normal distribution were assigned to the RVE grains. As for the HAZ region, identical Si particle distribution in each grain was assumed. The model and corresponding simulation results are shown in Fig. 45a and b. It can be observed that the proposed homogenized model can capture the anisotropic nature of the FMP and CMP zones, due to the introduction of $2k\theta/\pi+b$. The distinction between FMP and CMP is achieved using different normal distribution parameters for the Al cell size.

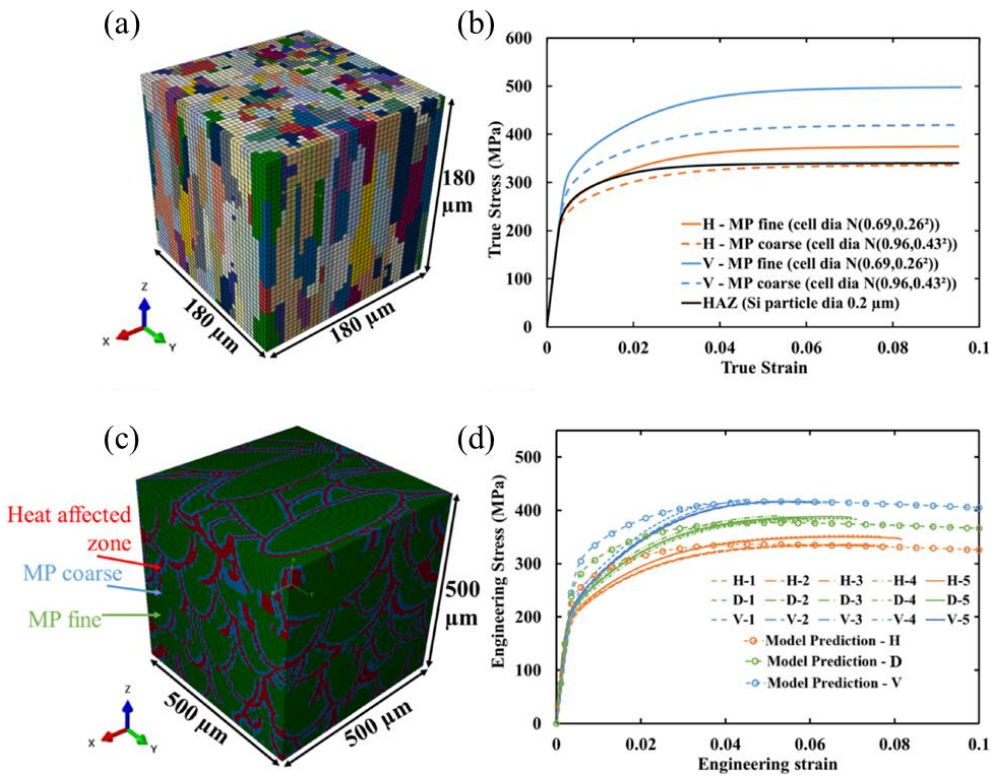

Fig. 45. Mesoscale and macroscale property prediction by RVE simulations [182]. Polycrystal RVE model (a) and corresponding simulations with homogenized crystal plasticity model for different regions of melt pool and different loading directions (b), multilayered RVE model (c) and corresponding simulations with interpolated behavior from polycrystal RVE simulations (d). The figures are reprinted with permission from Elsevier.

At the macroscale, to investigate the collective behavior of the bulk microstructure, Li et al. [182] constructed a RVE model incorporating several layers of melt pools composed of the FMP, CMP and HAZ regions (Fig. 44). A piecewise linear interpolation of the simulation results of different regions presented in Fig. 45b was used as material property input for both horizontal and vertical RVE models. The multilayered RVE model and corresponding simulation results are shown in Fig. 45c and d. The simulations can predict the mechanical response of the bulk microstructure well in different loading directions, especially in terms of tensile strength.

This multi-scale modeling scheme successfully bridges different structure scales and allows to assess the macroscopic behavior. It can be regarded as the most advanced modeling strategy for LPBF AlSi10Mg so far. Although it is not explicitly addressed in the study, the microscale

crystal plasticity finite element simulations allow to evaluate the phase stresses in both horizontal and vertical specimens and consequently help to understand the anisotropic damage behavior, which, according to Song et al [171], originates from dependence of phase load partition on loading direction.

Nevertheless, the following points still have to be improved to generalize this multi-scale scheme: (i) the HAZ structure needs to be more accurately modeled, treating the Si-rich eutectic as globular particles might be far from the real structure revealed by 3D characterization (see Fig. 10); (ii) when homogenizing two phases, some important information, such as Si-rich network size and connectivity, shall be introduced; if one can introduce size and connectivity coefficients to distinguish FMP, CMP and HAZ, then only one set of parameters need to be calibrated for all zones; (iii) the transition from polycrystal RVE to multilayered RVE shall be performed using more sophisticated homogenization method rather than linear interpolation.

8. Remaining issues and outlook for further work

The present review has combed the state of the art on as built LPBF AlSi10Mg on different aspects such as microstructure, strength, damage, ductility, fracture toughness, fatigue resistance and modeling and simulations. Learning from the previous works, we propose that the following points deserve further investigations, in order to draw a more complete roadmap from process strategy to microstructure and then to mechanical performance of LPBF Al alloys.

8.1 Process strategy-microstructure mapping

The correlation between process strategy and microstructure has not been fully established. Although previous works have achieved basic causal relationship separately describing the influences of laser parameters, scan strategy and build platform temperature on microstructure morphology and size, precise control of microstructure still remains challenging. For example, the process window leading to nanosized particles within Al cells is not identified yet. Note that the nanosized particles can significantly strengthen the α-Al phase (see Table 3) and hence

influence the load partition between phases, which in turn promotes or delays damage initiation. In this sense, more attention needs to be paid on solid state thermal cycling after rapid solidification, which can play a vital role in the precipitation phenomenon for additive manufactured metals [229].

Given the remarkable influence of build platform temperature, it will be important to investigate this factor jointly with laser parameters in the future. Mechanistic model and newly emerged machine learning approach, accompanied with high throughput experiments, can be applied to tackle the issue of identifying an optimized process window (see Fig. 46), as already tried in some previous works [68, 230, 231], presenting great potential to shape the future of metal additive manufacturing [59]. The ultimate goal of process optimization is to achieve dense and mechanically sound LPBF parts.

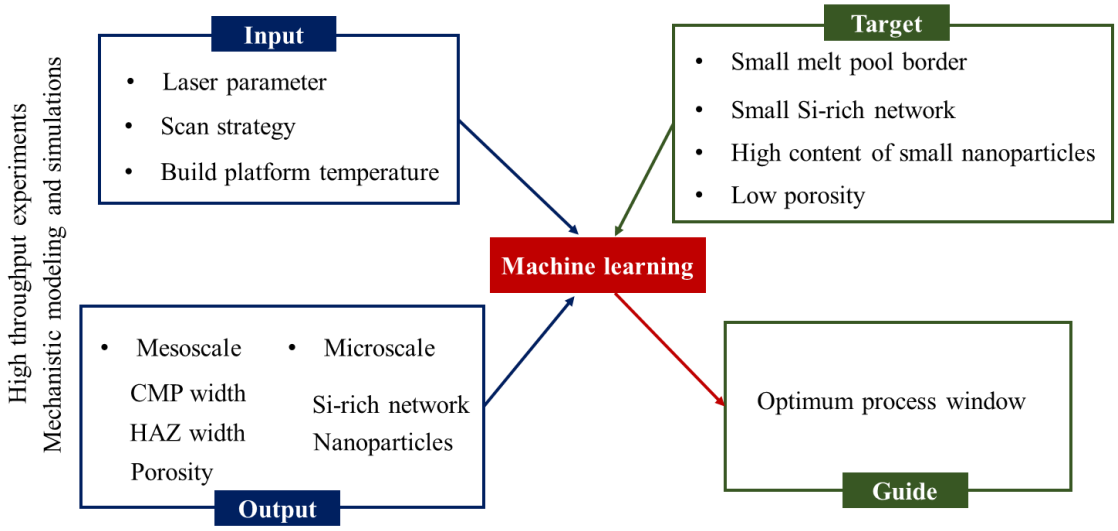

Fig. 46. Machine learning assisted process optimization workflow.

8.2 Microstructure descriptor

Unlike conventional cast or wrought Al alloys, LPBF AlSi10Mg presents a more complex microstructure, as reflected by its trans-scale, hierarchical and heterogeneous features. It is commonly desired to define a microstructure descriptor that can be directly linked to mechanical strength. The microstructure of conventional Al alloys is generally described by the

morphology and dimension of grains, precipitates and secondary phase. However, it is quite challenging to shape a microstructure descriptor for LPBF AlSi10Mg, given the aforementioned features.

Recently, Liu et al. [68] defined dimensional-scale index I_d and shape index I_s based on the principal component analysis (PCA) to describe the size and morphology of the Si-rich eutectic in the FMP zone (Fig. 47a and b). The index I_d involves the structure size (area, major axis length and perimeter) and shape fullness (i.e., roundness and convexity). A higher I_d indicates larger Al cells which on average contain more convex hull structures. The index I_s involves the shape (i.e., aspect ratio and eccentricity) and boundary details (i.e., tortuosity). A higher I_s indicates a slimmer cell structure with a smoother boundary. Furthermore, I_d is significantly more influential than I_s. Through variable regression analysis, the authors have shown that though single I_d, I_s and grain size cannot fully explain the large differences of strength for different microstructures, the combination of the three does a much better job.

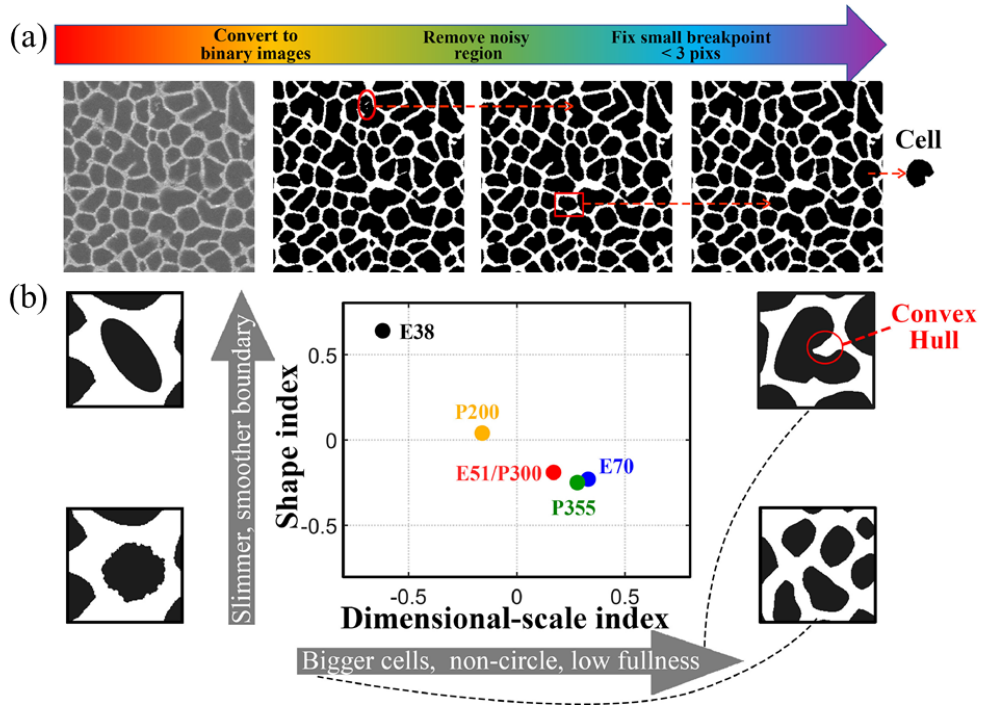

Fig. 47. Definition of dimensional-scale index I_d and shape index I_s [68]. Image processing steps to extract the Si-rich network (a), schematic interpretation for mean values of the morphology indices I_d and I_s (b). The figures are reprinted with permission from Elsevier.

Regarding the description of HAZ, it is unclear whether the aforementioned dimensional-scale index and shape index still work or not, given the degraded Si-rich eutectic connectivity. Moreover, how to quantify the connectivity of the Si-rich network remains an issue. The common treatment is to define the connectivity as the volume fraction of the largest object of one phase with respect to the total volume fraction of that phase in the analyzed volume [26, 47]. However, one can obtain the same value for a fully interconnected network and a network with many broken branches. Evidently, local branch breakage will impact the load transfer and consequently influence the mechanical strength. In previous investigations, researchers usually tended to consider the Si-rich eutectic in the HAZ as fully globular particles [45, 182]. However, this may not be accurate, as the 3D visualization of HAZ suggests that the Si-rich eutectic presents a branched morphology instead of being fully globular (see Fig. 10).

8.3 Stress partition in different zones

The evolutions of average phase stresses of Al cells and Si-rich eutectic as a function of macroscopic strain have been revealed by Kim et al. [71] and Zhang et al. [44]. These experimental data allow to understand the contribution of each phase to macroscopic flow stress and can also serve as support for constitutive model parameter calibration [178, 224]. However, as LPBF AlSi10Mg contains a heterogeneous microstructure, the load partition between Al cells and Si-rich eutectic in FMP, CMP and HAZ (Al cell hierarchy) and load partition between FMP, CMP and HAZ regions (melt pool hierarchy) are still to be unraveled. It is widely recognized that the CMP and HAZ are weaker zones in the microstructure. The load partition between different regions is expected to vary as a function of loading direction. Characterization of load partition at these two microstructure hierarchies will be important to understand the anisotropic strength and damage behaviors.

The CMP and HAZ are quite small, direct measurements of stress at such a low scale are quite challenging. When the mechanical properties of FMP, CMP and HAZ have been acquired

by micromechanical testing, as done by Li et al. [182], the load partition between different regions can be indirectly achieved by strain measurement, for example through digital image correlation (DIC). High-resolution DIC based on nanosized speckle pattern has been well developed and employed to investigate local deformation behaviors of metals [232-235]. In particular, the cool, dry speckle pattern deposition strategy recently proposed by Shafqat and Hoefnagels [234] would be appropriate for as built LPBF AlSi10Mg, which is sensible to high temperature. As shown in Fig. 48a, the specific nanoparticle deposition setup is made of readily available non-specialized parts, and the patterning process does not require exposure to chemicals, physical contact or vacuum. Moreover, the patterning is carried out at nearly room temperature (around 37°C). An example of 50 nm silica nanoparticle deposition on polished steel is shown in Fig. 48b, c. Such speckle pattern could allow to assess the local deformation field, even inside the melt pool border.

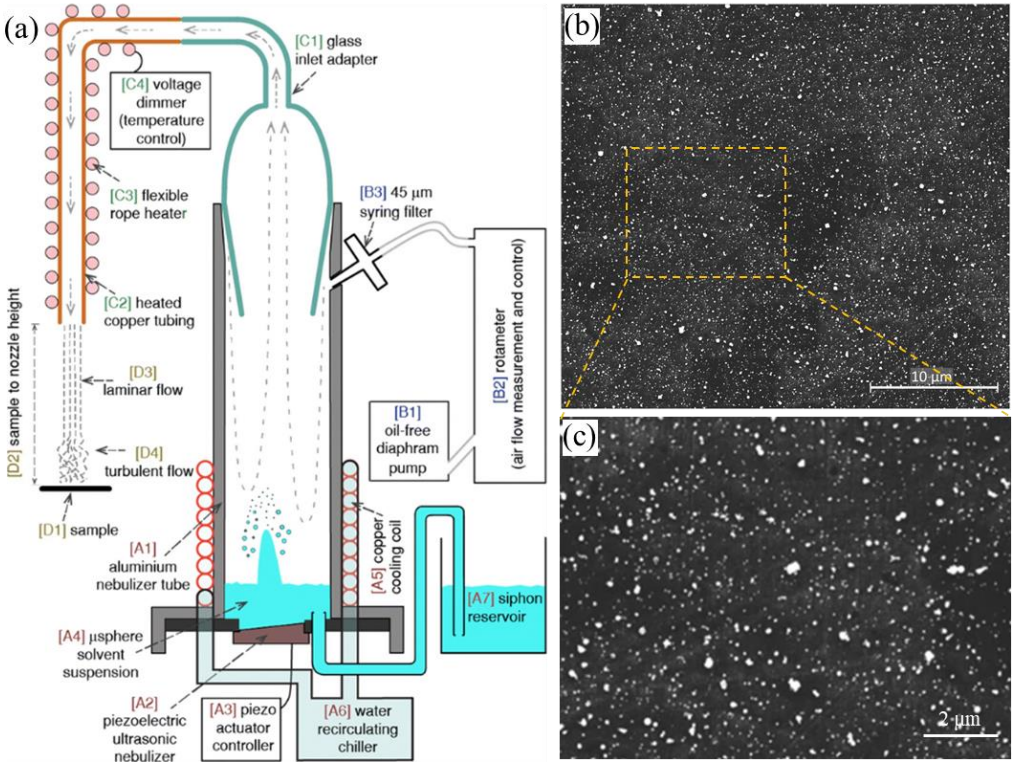

Fig. 48. Cool, dry, nano-scale DIC patterning using specific patterning setup [234]. Schematic drawing of the proposed setup (a), SEM image of 50 nm silica nanoparticles deposited on a polished steel specimen (b), local view of the speckle pattern (c). The figures are reproduced with permission from

Springer Nature.

One should also be aware of the effect of strain gradient, which promotes additional hardening effect. It is noteworthy that Song et al. [171] revealed quite strong strain gradient at the melt pool border of vertical specimens. It is therefore necessary to assess the contribution of strain gradient to flow stress via numerical simulation, as will be discussed in section 8.5.

8.4 Damage evolution and competition

From the review of previous studies, it can be seen that the most debatable issue for mechanical behavior of LPBF AlSi10Mg is the damage mechanism. Most researchers proposed that damage will be confined at the melt pool border due to strain localization. This viewpoint coincides with the presence of melt pool traces on fracture surface [45, 47, 49, 113, 150, 180]. However, with careful characterization on sound (i.e., low initial porosity) sample, some recent works showed that damage can be randomly dispersed in the microstructure, even for vertical specimens [47, 171]. Moreover, although the crack propagates more frequently along melt pool borders of vertical specimens, the fracture strain is found to be very close between horizontal and vertical specimens [47, 171]. In this sense, the damage initiation and evolution in the FMP, CMP and HAZ regions as well as their competition deserve further investigations to fully understand the damage mechanisms of LPBF AlSi10Mg.

It is noteworthy that Zhao et al. [27] have demonstrated that a low initial porosity does not significantly influence the ductility. Then, what are the critical porosity size and density with which damage and fracture process will be greatly accelerated? Will the critical size and density be dependent on mechanical strength and therefore be different for distinct melt pool zones (between FMP, CMP and HAZ)? These questions should be properly addressed in future studies to guide the tolerance design of porosity in printed parts.

8.5 Modeling and simulation

Modeling and simulation are emerging research branches on mechanical behavior of LPBF

metals. To capture the underlying microstructure features controlling the macroscopic flow stress, multi-scale modeling scheme has already been attempted for AlSi10Mg [182, 224]. It is worth mentioning that such modeling framework is a good fit for the trans-scale and heterogeneous microstructural features of LPBF AlSi10Mg, as presented in Fig. 49.

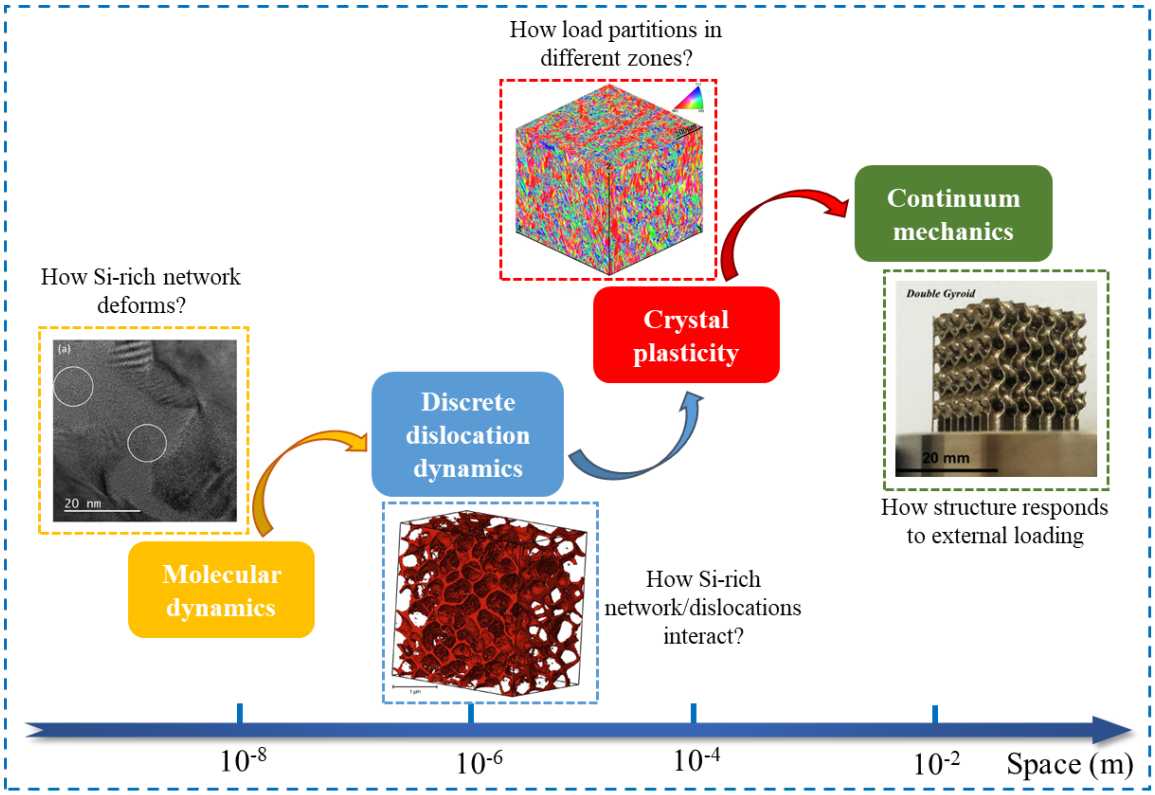

Fig. 49. Multiscale modeling and simulation strategy for LPBF AlSi10Mg. The inserted figures are reprinted from [25, 26, 73, 92] with permission from Elsevier.

However, modeling and simulation are only at an incipient development stage and several issues still need to be tackled to validate the reliability of pre-existing models and to guide further model developments, such as:

(1) Mechanical behavior of Si-rich eutectic: It is necessary to clarify whether the Si-rich eutectic yields or not under external loading. This point is particularly important as it will influence the Si-eutectic stress level which in turn determines damage initiation of the microstructure. Molecular dynamics simulations can be employed to address this issue (Fig. 49), accompanied with more detailed TEM characterization.

(2) Geometric model of HAZ structure: HAZ modeling should consider more accurately the Si-rich eutectic morphology, which is far from globular according to the 3D characterization (Fig. 10). An accurate geometric model is the base for reliable load partition analysis.

(3) Interaction between Si-rich network and dislocations: Dislocation motion is constrained within the Al cells by the Si-rich network (either highly interconnected or degraded). The shape of the Si-rich network therefore greatly influences dislocation evolution and consequently strain hardening. Considering that the network morphology has been accurately characterized in the FMP, CMP and HAZ [26], the interaction between Si-rich network and dislocations can be investigated by discrete dislocation dynamics simulations (Fig. 49). Results of such simulations can be used for parameter calibration of the crystal plasticity models.

(4) Contribution of strain gradient (GNDs) to the flow stress of α-Al and melt pool border: The strain gradient effect will impact the load partition between phases and regions. Experimental characterization has already confirmed the presence of strain gradient at both the Al cell and melt pool hierarchies; it is hence important to take into account the strain gradient hardening in modeling, using for example the mechanism-based strain gradient crystal plasticity theory [236, 237] or conventional theory of mechanism-based strain gradient plasticity [238].

(5) Homogenization of lower scale response: The treatments of homogenization in previous works are still quite approximative. For example, when homogenizing the Al cells and the Si-rich eutectic, the important microstructure information, i.e., the Si-rich network size was lost in the upscale treatment in [182]. Moreover, the mesoscale to macroscale transition was only based on data interpolation. In the future, more sophisticated homogenization methods [239] shall be applied to bridge different structure scales.

Previous modeling and simulation mainly focused on the plastic deformation. In the future, efforts should also be dedicated to develop a damage evolution model to describe damage

competition between the FMP, CMP and HAZ regions. Traditional damage models for ductile materials can be tried, such as GTN [240-242] and Lemaitre [243] models; model parameters might vary for different regions given the microstructural heterogeneity. Moreover, micromechanical modeling based on RVE can also be employed explicitly considering the real Al cells and Si-rich eutectic. Then the multi-scale damage models can be constructed using the homogenization approach. The ultimate goal is to establish an integrated model incorporating both plastic deformation and damage evolution.

After acquiring the multi-scale plasticity and damage models, parametric studies can be performed to seek an optimized microstructure imparting both high strength and ductility. For example, to improve the ductility, an efficient way might be increasing the strength and hardening ability of the Al phase, which will mitigate the load bearing of the Si network, delaying damage initiation. Xiao et al. [244] showed that incorporation of nano-TiB_2 particles could slightly enhance the strength while significantly increase the ductility of LPBF AlSi10Mg.

9. Conclusions

In the present review, the state of the art on knowledge of microstructure and mechanical behavior of as built LPBF AlSi10Mg has been thoroughly presented and discussed. Summarizing previous works, the following conclusions can be drawn:

(1) With the application of advanced characterization techniques, microstructural features of LPBF AlSi10Mg have been described comprehensively. Moreover, basic qualitative correlation between process strategy and microstructural characteristics has been established.

(2) Initial porosity cannot be completely eliminated due to the complex laser powder interdependency dynamics. However, porosity can already be reduced to a low level with parameter optimization. Even using machine manufacturer recommended parameters, very high density of as built parts can be achieved.

(3) Dependence of yield strength, strain hardening, damage and fracture resistance on

microstructure morphology and fineness has been clarified. Anisotropic strength seems to be induced by the elongated cellular Si-rich network, while anisotropic fracture toughness mainly originates from the melt pool arrangement. Low initial porosity appears to present a very limited influence on strength and ductility.

(4) Fatigue failure generally initiates from surface defects and internal defects (i.e., porosity or oxide) in the low to high cycle fatigue and very high cycle fatigue regimes, respectively. As built material presents a higher fatigue resistance compared to post-treated counterparts involving a similar porosity level but lower mechanical strength. Vertical samples generally present a lower fatigue strength due to the detrimental orientation of lack of fusion defects.

(5) A multi-scale modeling scheme addressing plastic deformation has been proposed. Such modeling strategy is appropriate and necessary to depict the mechanical behavior of the trans-scale, hierarchical and heterogeneous microstructure of LPBF AlSi10Mg.

On the other hand, the following aspects still deserve further investigation in the future to fully establish the process-microstructure-performance relation and to explore the great potential of LPBF Al alloys:

(1) Accurate manufacturing strategy-microstructure mapping: Previous works mainly focused on the influence of process strategy on the Al cells and melt pools; little attention has been paid to solid solution and nanosized particles. Note that the Al matrix strength would alter load partition between phases and therefore influence strength and damage behavior.

(2) Unified microstructure description: Unified microstructure descriptors allow to quantify the microstructural features. They can be used for strength prediction with either theoretical or numerical models. How to describe the microstructure throughout the melt pool with one or a few parameters still seems challenging.

(3) Load partition between heterogeneous zones: Previous experimental works have attempted to address load partition between the Si-rich eutectic and Al cells. However, how the

stress field is distributed in different regions (i.e., FMP, CMP and HAZ) is still unknown.

(4) Damage evolution and competition between heterogeneous zones: Damage evolution is highly dependent on microstructure. Previous works have primarily clarified damage evolution in the FMP or CMP. Nevertheless, synergetic developments of damage evolution and stress redistribution in different regions are still open scientific endeavors.

(5) Multi-scale modeling and simulation: Investigations via modeling and simulation are emerging. The multi-scale strategy is believed to be the appropriate methodology to assess strength, hardening and damage behavior of a complex microstructure such as that of LPBF AlSi10Mg. More efforts are needed to improve modeling of plastic deformation and to initiate modeling of damage evolution.

It is worth pointing out that the aforementioned issues are related to not only LPBF AlSi10Mg, but also to other additively manufactured metals, given the common inherent trans-scale, hierarchical and heterogeneous features of the AM induced microstructure. In this sense, the gained knowledge and the modeling scheme are expected to be transferred directly to developed or emerging AM metals, in particular AM Al alloys.

Declaration of Competing Interest

The authors declare that they have no known competing financial interests or personal relationships that could have appeared to influence the work reported in this paper.

Acknowledgements

L.Z. acknowledges the support from the Fundamental Research Funds for the Central Universities, China (2021XXJS116). A.S. thanks the WALInnov LongLifeAM project (convention n° 1810016) funded by the Service public de Wallonie Économie Emploi Recherche (SPW-EER) and the European Research Council (ERC) for the Starting Grant ALUFIX project (grant agreement n° 716678).

References

[1] D.D. Gu, W. Meiners, K. Wissenbach, R. Poprawe, Laser additive manufacturing of metallic components: materials, processes and mechanisms, International Materials Reviews 57 (2012) 133-164.
[2] W.J. Sames, F.A. List, S. Pannala, R.R. Dehoff, S.S. Babu, The metallurgy and processing science of metal additive manufacturing, International Materials Reviews 61 (2016) 315-360.
[3] B. Blakey-Milner, P. Gradl, G. Snedden, M. Brooks, J. Pitot, E. Lopez, M. Leary, F. Berto, A. du Plessis, Metal additive manufacturing in aerospace: A review, Materials and Design 209 (2021) 110008.
[4] E. RUAG Altair, Sentinel Antenna Bracket. <https://www.eos.info/01_parts-and-applications/case_studies_applications_parts/_case_studies_pdf/en_cases/cs_m_aerospace_ruag_en.pdf (accessed Mar. 04, 2022)>).
[5] Altair, Generative Design and Topology Optimization by Altair. <https://cdn2.hubspot.net/hubfs/47251/Altair_Generative_Design_Report.pdf (accessed Mar. 04, 2022)>).
[6] M.E. Orme, R. Vernon, I.J. Madera, R. Yancey, F. Mouriaux, Additive manufacturing of lightweight, optimized, metallic components suitable for space flight, Journal of Spacecraft and Rockets 54 (2017) 1050-1059.
[7] Sogeti, Vertical tail plane bracket. <https://www.eos.info/01_parts-and-applications/case_studies_applications_parts/_case_studies_pdf/en_cases/cs_m_aerospace_sogeti_en.pdf (accessed Mar. 04, 2022)>).
[8] J.H. Martin, B.D. Yahata, J.M. Hundley, J.A. Mayer, T.A. Schaedler, T.M. Pollock, 3D printing of high-strength aluminium alloys, Nature 549 (2017) 365-369.
[9] M.L. Montero-Sistiaga, R. Mertens, B. Vrancken, X. Wang, B. Van Hooreweder, J.-P. Kruth, J. Van Humbeeck, Changing the alloy composition of Al7075 for better processability by selective laser melting, Journal of Materials Processing Technology 238 (2016) 437-445.
[10] S.Y. Zhou, Y. Su, H. Wang, J. Enz, T. Ebel, M. Yan, Selective laser melting additive manufacturing of 7xxx series Al-Zn-Mg-Cu alloy: Cracking elimination by co-incorporation of Si and TiB2, Additive Manufacturing 36 (2020) 101458.
[11] W. Stopyra, K. Gruber, I. Smolina, T. Kurzynowski, B. Kuźnicka, Laser powder bed fusion of AA7075 alloy: Influence of process parameters on porosity and hot cracking, Additive Manufacturing 35 (2020) 101270.
[12] P. Mair, L. Kaserer, J. Braun, N. Weinberger, I. Letofsky-Papst, G. Leichtfried, Microstructure and mechanical properties of a TiB2-modified Al–Cu alloy processed by laser powder-bed fusion, Materials Science and Engineering A 799 (2021) 140209.
[13] F. Belelli, R. Casati, M. Vedani, J. Volpp, Design and characterization of Al-Mg-Si-Zr alloys with improved laser powder bed fusion processability, Metallurgical and Materials Transactions A 53 (2022) 331-343.
[14] R. Li, M. Wang, Z. Li, P. Cao, T. Yuan, H. Zhu, Developing a high-strength Al-Mg-Si-Sc-Zr alloy for selective laser melting: Crack-inhibiting and multiple strengthening mechanisms, Acta Materialia 193 (2020) 83-98.
[15] D. Bayoumy, D. Schliephake, S. Dietrich, X.H. Wu, Y.M. Zhu, A.J. Huang, Intensive processing optimization for achieving strong and ductile Al-Mn-Mg-Sc-Zr alloy produced by selective laser melting, Materials and Design 198 (2021) 109317.
[16] D. Liu, B. Yürekli, T. Ullsperger, G. Matthäus, L. Schade, S. Nolte, M. Rettenmayr, Microstructural aspects of additive manufacturing of Al-Li alloys with high Li content, Materials and Design 198 (2021) 109323.
[17] R. Xu, R. Li, T. Yuan, P. Niu, M. Wang, Z. Lin, Microstructure, metallurgical defects and hardness of Al-Cu-Mg-Li-Zr alloy additively manufactured by selective laser
melting, Journal of Alloys and Compounds 835 (2020) 155372.
[18] Z. Wang, X. Lin, N. Kang, Y. Wang, X. Yu, H. Tan, H. Yang, W. Huang, Making selective-laser-melted high-strength Al–Mg–Sc–Zr alloy tough via ultrafine and heterogeneous microstructure, Scripta Materialia 203 (2021) 114052.
[19] L. Zhou, H. Hyer, S. Thapliyal, R.S. Mishra, B. McWilliams, K. Cho, Y. Sohn, Process-dependent composition, microstructure, and printability of Al-Zn-Mg and Al-Zn-Mg-Sc-Zr alloys manufactured by

laser powder bed fusion, Metallurgical and Materials Transactions A 51 (2020) 3215-3227.
[20] L. Zhou, H. Hyer, J. Chang, A. Mehta, T. Huynh, Y. Yang, Y. Sohn, Microstructure, mechanical performance, and corrosion behavior of additively manufactured aluminum alloy 5083 with 0.7 and 1.0 wt% Zr addition, Materials Science and Engineering A 823 (2021) 141679.
[21] L. Zhou, H. Hyer, S. Park, H. Pan, Y. Bai, K.P. Rice, Y. Sohn, Microstructure and mechanical properties of Zr-modified aluminum alloy 5083 manufactured by laser powder bed fusion, Additive Manufacturing 28 (2019) 485-496.
[22] A. Mehta, L. Zhou, T. Huynh, S. Park, H. Hyer, S. Song, Y. Bai, D.D. Imholte, N.E. Woolstenhulme, D.M. Wachs, Y. Sohn, Additive manufacturing and mechanical properties of the dense and crack free Zr-modified aluminum alloy 6061 fabricated by the laser-powder bed fusion, Additive Manufacturing 41 (2021) 101966.
[23] F. Li, T. Zhang, Y. Wu, C. Chen, K. Zhou, Microstructure, mechanical properties, and crack formation of aluminum alloy 6063 produced via laser powder bed fusion, Journal of Materials Science (2022).
[24] H. Hyer, L. Zhou, A. Mehta, S. Park, T. Huynh, S. Song, Y. Bai, K. Cho, B. McWilliams, Y. Sohn, Composition-dependent solidification cracking of aluminum-silicon alloys during laser powder bed fusion, Acta Materialia 208 (2021) 116698.
[25] W. Lefebvre, G. Rose, P. Delroisse, E. Baustert, F. Cuvilly, A. Simar, Nanoscale periodic gradients generated by laser powder bed fusion of an AlSi10Mg alloy, Materials and Design 197 (2021) 109264.
[26] J.G. Santos Macías, T. Douillard, L. Zhao, E. Maire, G. Pyka, A. Simar, Influence on microstructure, strength and ductility of build platform temperature during laser powder bed fusion of AlSi10Mg, Acta Materialia 201 (2020) 231–243.
[27] L. Zhao, J.G. Santos Macías, L. Ding, H. Idrissi, A. Simar, Damage mechanisms in selective laser melted AlSi10Mg under as built and different post-treatment conditions, Materials Science and Engineering A 764 (2019) 138210.
[28] A. Hadadzadeh, B.S. Amirkhiz, B. Langelier, J. Li, M. Mohammadi, Microstructural consistency in the additive manufactured metallic materials: A study on the laser powder bed fusion of AlSi10Mg, Additive Manufacturing 46 (2021) 102166.
[29] H. Wu, Y. Ren, J. Ren, L. Liang, R. Li, Q. Fang, A. Cai, Q. Shan, Y. Tian, I. Baker, Selective laser melted AlSi10Mg alloy under melting mode transition: Microstructure evolution, nanomechanical behaviors and tensile properties, Journal of Alloys and Compounds 873 (2021) 159823.
[30] L. Thijs, K. Kempen, J.P. Kruth, J.V. Humbeeck, Fine-structured aluminium products with controllable texture by selective laser melting of pre-alloyed AlSi10Mg powder, Acta Materialia 61 (2013) 1809–1819.
[31] U. Patakham, A. Palasay, P. Wila, R. Tongsri, MPB characteristics and Si morphologies on mechanical properties and fracture behavior of SLM AlSi10Mg, Materials Science and Engineering A 821 (2021) 141602.
[32] J.C. Hastie, M.E. Kartal, L.N. Carter, M.M. Attallah, D.M. Mulvihill, Classifying shape of internal pores within AlSi10Mg alloy manufactured by laser powder bed fusion using 3D X-ray micro computed tomography: Influence of processing parameters and heat treatment, Materials Characterization 163 (2020) 110225.
[33] C. Weingarten, D. Buchbinder, N. Pirch, W. Meiners, K. Wissenbach, R. Poprawe, Formation and reduction of hydrogen porosity during selective laser melting of AlSi10Mg, Journal of Materials Processing Technology 221 (2015) 112-120.
[34] Z. Wu, S. Wu, J. Bao, W. Qian, S. Karabal, W. Sun, P.J. Withers, The effect of defect population on the anisotropic fatigue resistance of AlSi10Mg alloy fabricated by laser powder bed fusion, International Journal of Fatigue 151 (2021) 106317.
[35] I. Maskery, N.T. Aboulkhair, M.R. Corfield, C. Tuck, A.T. Clare, R.K. Leach, R.D. Wildman, I.A. Ashcroft, R.J.M. Hague, Quantification and characterisation of porosity in selectively lasermelted Al–Si10–Mg using X-ray computed tomography, Materials Characterization 111 (2016) 193-204.
[36] M. Giovagnoli, G. Silvi, M. Merlin, M.T. Di Giovanni, Optimisation of process parameters for an additively manufactured AlSi10Mg alloy: Limitations of the energy density-based approach on porosity and mechanical properties estimation, Materials Science and Engineering A 802 (2021) 140613.
[37] Z.M. Jian, G.A. Qian, D.S. Paolino, A. Tridello, F. Berto, Y.S. Hong, Crack initiation behavior and fatigue performance up to very-high-cycle regime of AlSi10Mg fabricated by selective laser melting with two

powder sizes, International Journal of Fatigue 143 (2021) 106013.
[38] L. Zhao, J.G. Santos Macías, A. Dolimont, A. Simar, E. Rivière-Lorphèvre, Comparison of residual stresses obtained by the crack compliance method for parts produced by different metal additive manufacturing techniques and after friction stir processing, Additive Manufacturing 36 (2020) 101499.
[39] J. Wu, X.Q. Wang, W. Wang, M.M. Attallah, M.H. Loretto, Microstructure and strength of selectively laser melted AlSi10Mg, Acta Materialia 117 (2016) 311-320.
[40] B. Chen, S.K. Moon, X. Yao, G. Bi, J. Shen, J. Umeda, K. Kondoh, Strength and strain hardening of a selective laser melted AlSi10Mg alloy, Scripta Materialia 141 (2019) 45-49.
[41] N. Takata, M. Liu, H. Kodaira, A. Suzuki, M. Kobashi, Anomalous strengthening by supersaturated solid solutions of selectively laser melted Al–Si-based alloys, Additive Manufacturing 33 (2020) 101152.
[42] A. Hadadzadeh, C. Baxter, B.S. Amirkhiz, M. Mohammadi, Strengthening mechanisms in direct metal laser sintered AlSi10Mg: Comparison between virgin and recycled powders, Additive Manufacturing 23 (2018) 108-120.
[43] Z. Li, Z. Li, Z. Tan, D. Xiong, Q. Guo, Stress relaxation and the cellular structure-dependence of plastic deformation in additively manufactured AlSi10Mg alloys, International Journal of Plasticity 127 (2020) 102640.
[44] X.X. Zhang, A. Lutz, H. Andrä, M. Lahres, W.M. Gan, E. Maawad, C. Emmelmann, Evolution of microscopic strains, stresses, and dislocation density during in-situ tensile loading of additively manufactured AlSi10Mg alloy, International Journal of Plasticity 139 (2021) 102946.
[45] J. Delahaye, J.T. Tchuindjang, J. Lecomte-Beckers, O. Rigo, A.M. Habraken, A. Mertens, Influence of Si precipitates on fracture mechanisms of AlSi10Mg parts processed by selective laser melting, Acta Materialia 175 (2019) 160–170.
[46] T. Maconachie, M. Leary, J. Zhang, A. Medvedev, A. Sarker, D. Ruan, G. Lu, O. Faruque, M. Brandt, Effect of build orientation on the quasi-static and dynamic response of SLM AlSi10Mg, Materials Science and Engineering A 788 (2020) 139445.
[47] L. Zhao, J.G. Santos Macías, T. Douillard, Z-H. Li, A. Simar, Unveiling damage sites and fracture path in laser powder bed fusion AlSi10Mg: Comparison between horizontal and vertical loading directions, Materials Science and Engineering A 807 (2021) 140845.
[48] L. Hitzler, E. Sert, E. Schuch, A. Öchsner, M. Merkel, B. Heine, E. Werner, Fracture toughness of L-PBF fabricated aluminium-silicon: a quantitative study on the role of crack growth direction with respect to layering, Progress in Additive Manufacturing 5 (2020) 259-266.
[49] M.J. Paul, Q. Liu, J.P. Best, X. Li, J.J. Kruzic, U. Ramamurty, B. Gludovatz, Fracture resistance of AlSi10Mg fabricated by laser powder bed fusion, Acta Materialia 211 (2021) 116869.
[50] E. Brandl, U. Heckenberger, V. Holzinger, D. Buchbinder, Additive manufactured AlSi10Mg samples using selective laser melting (SLM): Microstructure, high cycle fatigue, and fracture behavior, Materials and Design 34 (2012) 159-169.
[51] N.T. Aboulkhair, I. Maskery, C. Tuck, I. Ashcroft, N.M. Everitt, Improving the fatigue behaviour of a selectively laser melted aluminium alloy: Influence of heat treatment and surface quality, Materials and Design 104 (2016) 174-182.
[52] N.E. Uzan, R. Shneck, O. Yeheskel, N. Frage, Fatigue of AlSi10Mg specimens fabricated by additive manufacturing selective laser melting (AM-SLM), Materials Science and Engineering A 704 (2017) 229-237.
[53] M. Awd, S. Siddique, J. Johannsen, C. Emmelmann, F. Walther, Very high-cycle fatigue properties and microstructural damage mechanisms of selective laser melted AlSi10Mg alloy, International Journal of Fatigue 124 (2019) 55-69.
[54] S. Beretta, M. Gargourimotlagh, S. Foletti, A. du Plessis, M. Riccio, Fatigue strength assessment of “as built” AlSi10Mg manufactured by SLM with different build orientations, International Journal of Fatigue 139 (2020) 105737.
[55] T.D. Piette, R.J. Warren, A.G. Spangenberger, E.J. Hummelt, D.A. Lados, Microstructure evolution, fatigue crack growth, and ultrasonic fatigue in as-fabricated laser powder bed and conventionally cast Al–10Si-0.4Mg: A mechanistic understanding and integrated flaw-sensitive fatigue design methods, Materials Science and Engineering A 825 (2021) 141892.

[56] Z. Xu, A. Liu, X. Wang, Fatigue performance and crack propagation behavior of selective laser melted AlSi10Mg in 0°, 15°, 45° and 90° building directions, Materials Science and Engineering A 812 (2021) 141141.
[57] J.G. Santos Macías, C. Elangeswaran, L. Zhao, J.-Y. Buffière, B.V. Hooreweder, A. Simar, Fatigue crack nucleation and growth in laser powder bed fusion AlSi10Mg under as built and post-treated conditions, Materials and Design 210 (2021) 110084.
[58] K.G. Prashanth, J. Eckert, Formation of metastable cellular microstructures in selective laser melted alloys, Journal of Alloys and Compounds 707 (2017) 27-34.
[59] T. DebRoy, T. Mukherjee, H.L. Wei, J.W. Elmer, J.O. Milewski, Metallurgy, mechanistic models and machine learning in metal printing, Nature Reviews Materials 6 (2021) 48-68.
[60] S.A. Khairallah, A.A. Martin, J.R.I. Lee, G. Guss, N.P. Calta, J.A. Hammons, M.H. Nielsen, K. Chaput, E. Schwalbach, M.N. Shah2, M.G. Chapman, T.M. Willey, A.M. Rubenchik, A.T. Anderson, Y.M.Wang, M.J. Matthews, W.E. King, Controlling interdependent meso-nanosecond dynamics and defect generation in metal 3D printing, Science 368 (2020) 660-665.
[61] J.G. Santos Macías, C. Elangeswaran, L. Zhao, B.V. Hooreweder, J. Adrien, E. Maire, J.-Y. Buffière, W. Ludwig, P.J. Jacques, A. Simar, Ductilisation and fatigue life enhancement of selective laser melted AlSi10Mg by friction stir processing, Scripta Materialia 170 (2019) 124-128.
[62] N. Takata, H. Kodaira, K. Sekizawa, A. Suzuki, M. Kobashi, Change in microstructure of selectively laser melted AlSi10Mg alloy with heat treatments, Materials Science and Engineering A 704 (2017) 218–228.
[63] A.H. Maamoun, M. Elbestawi, G.K. Dosbaeva, S. C. Veldhuis, Thermal post-processing of AlSi10Mg parts produced by selective laser melting using recycled powder, Additive Manufacturing 21 (2018) 234-247.
[64] N.T. Aboulkhair, I. Maskery, C. Tuck, I. Ashcroft, N.M. Everitt, The microstructure and mechanical properties of selectively laser melted AlSi10Mg: The effect of a conventional T6-like heat treatment, Materials Science and Engineering A 667 (2019) 139-146.
[65] N.O. Larrosa, W. Wang, N. Read, M.H. Loretto, C. Evans, J. Carr, U. Tradowsky, M.M. Attallah, P.J. Withers, Linking microstructure and processing defects to mechanical properties of selectively laser melted AlSi10Mg alloy, Theoretical and Applied Fracture Mechanics 98 (2018) 123-133.
[66] T. Hirata, T. Kimura, T. Nakamoto, Effects of hot isostatic pressing and internal porosity on the performance of selective laser melted AlSi10Mg alloys, Materials Science and Engineering A 772 (2020) 138713.
[67] D. Gu, X. Shi, R. Poprawe, D.L. Bourell, R. Setchi, J. Zhu, Material-structure-performance integrated laser-metal additive manufacturing, Science 372 (2021) 932.
[68] Q. Liu, H. Wu, M.J. Paul, P. He, Z. Peng, B. Gludovatz, J.J. Kruzic, C.H. Wang, X. Liu, Machine-learning assisted laser powder bed fusion process optimization for AlSi10Mg: New microstructure description indices and fracture mechanisms, Acta Materialia 201 (2020) 316-328.
[69] C. Gobert, A. Kudzal, J. Sietins, C. Mock, J. Sun, B. McWilliams, Porosity segmentation in X-ray computed tomography scans of metal additively manufactured specimens with machine learning, Additive Manufacturing 36 (2020) 101460.
[70] W. Muhammad, A.P. Brahme, O. Ibragimova, K. Inal J. Kang, A machine learning framework to predict local strain distribution and the evolution of plastic anisotropy & fracture in additively manufactured alloys, International Journal of Plasticity 136 (2021) 102867.
[71] D.K. Kim, W. Woo, J.H. Hwang, K. An, S.H. Choi, Stress partitioning behavior of an AlSi10Mg alloy produced by selective laser melting during tensile deformation using in situ neutron diffraction, Journal of Alloys and Compounds 686 (2016) 281-286.
[72] J.C. Hastie, J. Koelblin, M.E. Kartal, M.M. Attallah, R. Martinez, Evolution of internal pores within AlSi10Mg manufactured by laser powder bed fusion under tension: As-built and heat treated conditions, Materials and Design 204 (2021) 109645.
[73] N.T. Aboulkhair, M. Simonelli, L. Parry, I. Ashcroft, C. Tuck, R. Hague, 3D printing of Aluminium alloys: Additive Manufacturing of Aluminium alloys using selective laser melting, Progress in Materials Science 106 (2019) 100578.
[74] J. Zhang, B. Song, Q. Wei, D. Bourell, Y. Shi, A review of selective laser melting of aluminum alloys:

Processing, microstructure, property and developing trends, Journal of Materials Science & Technology 35 (2019) 270–284.
[75] J. Fiocchi, A. Tuissi, C.A. Biffi, Heat treatment of aluminium alloys produced by laser powder bed fusion: A review, Materials and Design 204 (2021) 109651.
[76] P. Ponnusamy, R.A.R. Rashid, S.H. Masood, D. Ruan, S. Palanisamy, Mechanical properties of SLM-printed aluminium alloys: A review, materials 13 (2020) 4301.
[77] H.R. Kotadia, G. Gibbons, A. Das, P.D. Howes, A review of laser powder bed fusion additive manufacturing of aluminium alloys: Microstructure and properties, Additive Manufacturing 46 (2021) 102155.
[78] T. DebRoy, H.L. Wei, J.S. Zuback, T. Mukherjee, J.W. Elmer, J.O. Milewski, A.M. Beese, A. Wilson-Heid, A. De, W. Zhang, Additive manufacturing of metallic components – Process, structure and properties, Progress in Materials Science 92 (2018) 112-224.
[79] C. Panwisawas, Y.T. Tang, R.C. Reed, Metal 3D printing as a disruptive technology for superalloys, Nature Communications 11 (2020) 2327.
[80] X.P. Li, X.J. Wang, M. Saunders, A. Suvorova, L.C. Zhang, Y.J. Liu, M.H. Fang, Z.H. Huang, T.B. Sercombe, A selective laser melting and solution heat treatment refined Al–12Si alloy with a controllable ultrafine eutectic microstructure and 25% tensile ductility, Acta Materialia 95 (2015) 74-82.
[81] P. Van Cauwenbergh, V. Samaee, L. Thijs, J. Nejezchlebová, P. Sedlák, A. Ivekovi ć, D. Schryvers, B. Van Hooreweder, K. Vanmeensel, Unravelling the multi-scale structure–property relationship of laser powder bed fusion processed and heat-treated AlSi10Mg, Scientific Reports 11 (2021) 6423.
[82] X. Liu, C. Zhao, X. Zhou, Z. Shen, W. Liu, Microstructure of selective laser melted AlSi10Mg alloy, Materials and Design 168 (2019) 107667.
[83] A. Hadadzadeh, B.S. Amirkhiz, M. Mohammadi, Contribution of Mg2Si precipitates to the strength of direct metal laser sintered AlSi10Mg, Materials Science and Engineering A 739 (2019) 295-300.
[84] T. Maeshima, K. Oh-ishi, Solute clustering and supersaturated solid solution of AlSi10Mg alloy fabricated by selective laser melting, Heliyon 5 (2019) e01186.
[85] J. Fite, S.E. Pradeela, J.A. Slotwinski, T.P. Weihs, Evolution of the microstructure and mechanical properties of additively manufactured AlSi10Mg during room temperature holds and low temperature aging, Additive Manufacturing 36 (2020) 101429.
[86] H. Qin, Q. Dong, V. Fallah, M.R. Daymond, Rapid solidification and non-equilibrium phase constitution in laser powder bed fusion (LPBF) of AlSi10Mg alloy: Analysis of nano-precipitates, eutectic phases, and hardness evolution, Metallurgical and Materials Transactions A 51A (2020) 448-466.
[87] J. Fite, S.E. Prameela, J.A. Slotwinski, T.P. Weihs, Evolution of the microstructure and mechanical properties of additively manufactured AlSi10Mg during room temperature holds and low temperature aging, Additive Manufacturing 36 (2020) 101429.
[88] W. Kan, Y. Nadot, M. Foley, L. Ridosz, G. Proust, J.M. Cairney, Factors that affect the properties of additively-manufactured AlSi10Mg: Porosity versus microstructure, Additive Manufacturing 29 (2019) 100805.
[89] L. Zhou, A. Mehta, E. Schulz, B. McWilliams, K. Cho, Y. Sohn, Microstructure, precipitates and hardness of selectively laser melted AlSi10Mg alloy before and after heat treatment, Materials Characterization 143 (2018) 5-17.
[90] M. Albu, R. Krisper, J. Lammer, G. Kothleitner, J. Fiocchi, P. Bassani, Microstructure evolution during in-situ heating of AlSi10Mg alloy powders and additive manufactured parts, Additive Manufacturing 36 (2020) 101605.
[91] Q. Tan, J. Zhang, N. Mo, Z. Fan, Y. Yin, M. Bermingham, Y. Liu, H. Huang, M.-X. Zhang, A novel method to 3D-print fine-grained AlSi10Mg alloy with isotropic properties via inoculation with LaB6 nanoparticles, Additive Manufacturing 32 (2020) 101034.
[92] H. Qin, V. Fallah, Q. Dong, M. Brochu, M.R. Daymond, M. Gallerneault, Solidification pattern, microstructure and texture development in laser powder bed fusion (LPBF) of Al10SiMg alloy, Materials Characterization 145 (2018) 29-38.
[93] D. Buchbinder, W. Meiners, K. Wissenbach, R. Poprawe, Selective laser melting of aluminum die-cast

alloy–correlations between process parameters, solidification conditions, and resulting mechanical properties, Journal of Laser Applications 27 (2015) S29205.
[94] J. Liu, A.C. To, Quantitative texture prediction of epitaxial columnar grains in additive manufacturing using selective laser melting, Additive Manufacturing 16 (2017) 58-64.
[95] P. Liu, Z. Wang, Y. Xiao, M.F. Horstemeyer, X. Cui, L. Chen, Insight into the mechanisms of columnar to equiaxed grain transition during metallic additive manufacturing, Additive Manufacturing 26 (2019) 22-29.
[96] Y. He, M. Zhong, N. Jones, J. Beuth, B. Webler, The columnar-to-equiaxed transition in melt pools during laser powder bed fusion of M2 steel, Metallurgical and Materials Transactions A 52 (2021) 4206-4221.
[97] G.M. Karthik, H.S. Kim, Heterogeneous aspects of additive manufactured metallic parts: A review, Metals and Materials International 27 (2021) 1-39.
[98] C. Han, Q. Fang, Y. Shi, S.B. Tor, C.K. Chua, K. Zhou, Recent Advances on High-Entropy Alloys for 3D Printing, Advanced Materials (2020) 1903855.
[99] Y.M. Wang, T. Voisin, J.T. McKeown, J. Ye, N.P. Calta, Z. Li, Z. Zeng, Y. Zhang, W. Chen, T.T. Roehling, R.T. Ott, M.K. Santala, P.J. Depond, M.J. Matthews, A.V. Hamza, T. Zhu, Additively manufactured hierarchical stainless steels with high strength and ductility, Nature Materials 17 (2018) 63-70.
[100] Z. Li, B. He, Q. Guo, Strengthening and hardening mechanisms of additively manufactured stainless steels: The role of cell sizes, Scripta Materialia 177 (2020) 17-21.
[101] A.T. Silvestri, A. Astarita, A. El Hassanin, A. Manzo, U. Iannuzzo, G. Iannuzzo, V. De Rosa, F. Acerra, A. Squillace, Assessment of the mechanical properties of AlSi10Mg parts produced through selective laser melting under different conditions, Procedia Manufacturing 47 (2020) 1058-1064.
[102] M. Moshiri, S. Candeo, S. Carmignato, S. Mohanty, G. Tosello, Benchmarking of laser powder bed fusion machines, Journal of Manufacturing and Materials Processing 3 (2019) 85.
[103] M.E. Glicksman, Principles of solidification, New York: Springer (2011).
[104] S. Kou, Welding Metallurgy, John Wiley & Sons, 2003.
[105] U. Scipioni Bertoli, A.J. Wolfer, M.J. Matthews, J.P.R. Delplanque, J.M. Schoenung, On the limitations of volumetric energy density as a design parameter for selective laser melting, Materials and Design 113 (2017) 331-340.
[106] M. Tang, P.C. Pistorius, S. Narra, J.L. Beuth, Rapid solidification: selective laser melting of AlSi10Mg, JOM 68 (2016) 960-966.
[107] H. Hyer, L. Zhou, S. Park, G. Gottsfritz, G. Benson, B. Tolentino, B. McWilliams, K. Cho, Y. Sohn, Understanding the laser powder bed fusion of AlSi10Mg alloy, Metallography, Microstructure, and Analysis 9 (2020) 484-502.
[108] G. Vastola, G. Zhang, Q.X. Pei, Y.-W. Zhang, Controlling of residual stress in additive manufacturing of Ti6Al4V by finite element modeling, Additive Manufacturing 12 (2016) 231-239.
[109] M. Galati, L. Iuliano, A literature review of powder-based electron beam melting focusing on numerical simulations, Additive Manufacturing 19 (2018) 1-20.
[110] Z.W. Xu, Q. Wang, X.S. Wang, C.H. Tan, M.H. Guo, P.B. Gao, High cycle fatigue performance of AlSi10Mg alloy produced by selective laser melting, Mechanics of Materials 148 (2020) 103499.
[111] C.G. Wang, J.X. Zhu, G.W. Wang, Y. Qin, M.Y. Sun, J.L. Yang, X.F. Shen, S.K. Huang, Effect of building orientation and heat treatment on the anisotropic tensile properties of AlSi10Mg fabricated by selective laser melting, Journal of Alloys and Compounds 895 (2022).
[112] L. Girelli, M. Tocci, M. Gelfi, A. Pola, Study of heat treatment parameters for additively manufactured AlSi10Mg in comparison with corresponding cast alloy, Materials Science and Engineering A 739 (2019) 317–328.
[113] X. Li, D. Yi, X. Wu, J. Zhang, X. Yang, Z. Zhao, Y. Feng, J. Wang, P. Bai, B. Liu, Y. Liu, Effect of construction angles on microstructure and mechanical properties of AlSi10Mg alloy fabricated by selective laser melting, Journal of Alloys and Compounds 881 (2021) 160459.
[114] J. Fiocchi, C.A. Biffi, C. Colombo, L.M. Vergani, A. Tuissi, Ad hoc heat treatments for selective laser melted AlSi10Mg alloy aimed at stress-relieving and enhancing mechanical performances, JOM 72 (2020) 1118-1127.

[115] R. Casati, M.H. Nasab, M. Coduri, V. Tirelli, M. Vedani, Effects of platform pre-heating and thermal-treatment strategies on properties of AlSi10Mg alloy processed by selective laser melting, Metals 8 (2018) 954.
[116] E. Padovano, C. Badini, A. Pantarelli, F. Gili, F. D'Aiuto, A comparative study of the effects of thermal treatments on AlSi10Mg produced by laser powder bed fusion, Journal of Alloys and Compounds 831 (2020) 154822.
[117] A. Hadadzadeh, B.S. Amirkhiz, J. Li, M. Mohammadi, Columnar to equiaxed transition during direct metal laser sintering of AlSi10Mg alloy: Effect of building direction, Additive Manufacturing 23 (2018) 121-131.
[118] S. Romano, A. Brückner-Foit, A. Brandão, J. Gumpinger, T. Ghidini, S. Beretta, Fatigue properties of AlSi10Mg obtained by additive manufacturing: Defect-based modelling and prediction of fatigue strength, Engineering Fracture Mechanics 187 (2018) 165-189.
[119] E. Sert, L. Hitzler, S. Hafenstein, M. Merkel, E. Werner, A. Öchsner, Tensile and compressive behaviour of additively manufactured AlSi10Mg samples, Progress in Additive Manufacturing 5 (2020) 305-313.
[120] L. Hitzler, C. Janousch, J. Schanz, M. Merkel, B. Heine, F. Mack, W. Hall, A. Öchsner, Direction and location dependency of selective laser melted AlSi10Mg specimens, Journal of Materials Processing Technology 243 (2017) 48-61.
[121] H. Bian, K. Aoyagi, Y. Zhao, C. Maeda, T. Mouri, A. Chiba, Microstructure refinement for superior ductility of Al-Si alloy by electron beam melting, Additive Manufacturing 32 (2020) 100982.
[122] J. Fiocchi, A. Tuissi, P. Bassani, C.A. Biffi, Low temperature annealing dedicated to AlSi10Mg selective laser melting products, Journal of Alloys and Compounds 695 (2017) 3402-3409.
[123] L.C. Araújo, A.H.G. Gabriel, E.B. da Fonseca, J.A. Avila, A.L. Jardini, R. Seno Junior, E.S.N. Lopes, Effects of build orientation and heat treatments on the tensile and fracture toughness properties of additively manufactured AlSi10Mg, International Journal of Mechanical Sciences 213 (2022) 106868.
[124] A. Kempf, K. Hilgenberg, Influence of heat treatments on AlSi10Mg specimens manufactured with different laser powder bed fusion machines, Materials Science and Engineering A 818 (2021) 141371.
[125] L. Zhuo, Z. Wang, H. Zhang, E. Yin, Y. Wang, T. Xu, C. Li, Effect of post-process heat treatment on microstructure and properties of selective laser melted AlSi10Mg alloy, Materials Letters 234 (2019) 196-200.
[126] K. Kempen, L. Thijs, J. Van Humbeeck, J.-P. Kruth, Processing AlSi10Mg by selective laser melting: parameter optimisation and material characterisation, Materials Science and Technology 31 (2015) 917-928.
[127] T.-H. Park, M.-S. Baek, H. Hyer, Y. Sohn, K.-A. Lee, Effect of direct aging on the microstructure and tensile properties of AlSi10Mg alloy manufactured by selective laser melting process, Materials Characterization 176 (2021) 111113.
[128] H. Zhang, Y. Wang, J.J. Wang, D.R. Ni, D. Wang, B.L. Xiao, Z.Y. Ma, Achieving superior mechanical properties of selective laser melted AlSi10Mg via direct aging treatment, Journal of Materials Science & Technology 108 (2022) 226-235.
[129] I. Rosenthal, R. Shneck, A. Stern, Heat treatment effect on the mechanical properties and fracture mechanism in AlSi10Mg fabricated by additive manufacturing selective laser melting process, Materials Science and Engineering A 729 (2018) 310-322.
[130] Q. Guo, C. Zhao, L.I. Escano, Z. Young, L. Xiong, K. Fezzaa, W. Everhart, B. Brown, T. Sun, L. Chen, Transient dynamics of powder spattering in laser powder bed fusion additive manufacturing process revealed by in-situ high-speed highenergy x-ray imaging, Acta Materialia 151 (2018) 169-180.
[131] P. Bidare, I. Bitharas, R.M. Ward, M.M. Attallah, A.J. Moore, Fluid and particle dynamics in laser powder bed fusion, Acta Materialia 142 (2018) 107-120.
[132] R. Cunningham, C. Zhao, N. Parab, C. Kantzos, J. Pauza, K. Fezzaa, T. Sun, A.D. Rollett, Keyhole threshold and morphology in laser melting revealed by ultrahigh-speed x-ray imaging, Science 363 (2019) 489-852.
[133] N. Sanaei, A. Fatemi, Defects in additive manufactured metals and their effect on fatigue performance: A state-of-the-art review, Progress in Materials Science 117 (2021) 100724.

[134] C. Galy, E. Le Guen, E. Lacoste, C. Arvieu, Main defects observed in aluminum alloy parts produced by SLM: From causes to consequences, Additive Manufacturing 22 (2018) 165-175.
[135] J.G. Kaufman, E.L. Rooy, Aluminum alloy castings: properties, processes, and applications, ASM International (2004).
[136] K.V. Yang, P. Rometsch, T. Jarvis, J. Rao, S. Cao, C. Davies, X. Wu, Porosity formation mechanisms and fatigue response in Al-Si-Mg alloys made by selective laser melting, Materials Science and Engineering A 712 (2018) 166-174.
[137] M. Tang, P.C. Pistorius, J.L. Beuth, Prediction of lack-of-fusion porosity for powder bed fusion, Additive Manufacturing 14 (2017) 39-48.
[138] M.A. Balbaa, A. Ghasemi, E. Fereiduni, M.A. Elbestawi, S.D. Jadhav, J.-P. Kruth, Role of powder particle size on laser powder bed fusion processability of AlSi10mg alloy, Additive Manufacturing 37 (2021) 101630.
[139] A.A. Martin, N.P. Calta, S.A. Khairallah, J. Wang, P.J. Depond, A.Y. Fong, V. Thampy, G.M. Guss, A.M. Kiss, K.H. Stone, C.J. Tassone, J.N. Weker, M.F. Toney, T. van Buuren, M.J. Matthews, Dynamics of pore formation during laser powder bed fusion additive manufacturing, Nature Communications 10 (2019) 1987.
[140] J. Lu, X. Lin, N. Kang, Y. Cao, Q. Wang, W. Huang, Keyhole mode induced simultaneous improvement in strength and ductility of Sc modified Al-Mn alloy manufactured by selective laser melting, Materials Science and Engineering A 811 (2021) 141089.
[141] S.A. Khairallah, A.T. Anderson, A. Rubenchik, W.E. King, Laser powder-bed fusion additive manufacturing: Physics of complex melt flow and formation mechanisms of pores, spatter, and denudation zones, Acta Materialia 108 (2016) 36-45.
[142] L. Wang, Y. Zhang, H.Y. Chia, W. Yan, Mechanism of keyhole pore formation in metal additive manufacturing, npj Computational Materials 8 (2022) 22.
[143] H. Wu, J. Ren, Q. Huang, X. Zai, L. Liu, C. Chen, S. Liu, X. Yang, R. Li, Effect of laser parameters on microstructure, metallurgical defects and property of AlSi10Mg printed by selected laser melting, Journal of Micromechanics and Molecular Physics 02 (2017) 1750017.
[144] J. Gheysen, M. Marteleur, C. van der Rest, Efficient optimization methodology for laser powder bed fusion parameters to manufacture dense and mechanically sound parts validated on AlSi12 alloy, Materials and Design 199 (2021) 109433.
[145] Q. Yan, B. Song, Y. Shi, Comparative study of performance comparison of AlSi10Mg alloy prepared by selective laser melting and casting, Journal of Materials Science & Technology 41 (2020) 199–208.
[146] L.F. Wang, J. Sun, X.L. Yu, Y. Shi, X.G. Zhu, L.Y. Cheng, H.H. Liang, B. Yan, L.J. Guo, Enhancement in mechanical properties of selectively laser-melted AlSi10Mg aluminum alloys by T6-like heat treatment, Materials Science and Engineering A 734 (2018) 299-310.
[147] U. Tradowsky, J. White, R.M. Ward, N. Read, W. Reimers, M.M. Attallah, Selective laser melting of AlSi10Mg: Influence of post-processing on the microstructural and tensile properties development, Materials and Design 105 (2016) 212-222.
[148] M. Awd, F. Stern, A. Kampmann, D. Kotzem, J. Tenkamp, F. Walther, Microstructural characterization of the anisotropy and cyclic deformation behavior of selective laser melted AlSi10Mg structures, metals 8 (2018) 825.
[149] N. Read, W. Wang, K. Essa, M.M. Attallah, Selective laser melting of AlSi10Mg alloy: Process optimisation and mechanical properties development, Materials and Design 65 (2015) 417-424.
[150] Z.H. Xiong, S. L. Liu, S. F. Li, Y. Shi, Y.F. Yang, R.D.K. Misra, Role of melt pool boundary condition in determining the mechanical properties of selective laser melting AlSi10Mg alloy, Materials Science and Engineering A 740-741 (2019) 148–156.
[151] Y. Ou, Q. Zhang, Y. Wei, Y. Hu, S. Sui, J. Chen, X. Wang, W. Li, Evolution of heterogeneous microstructure and its effects on tensile properties of selective laser melted AlSi10Mg alloy, Journal of Materials Engineering and Performance 30 (2021) 4341-4355.
[152] K. Kempen, L. Thijs, J. Van Humbeeck, J.-P. Kruth, Mechanical properties of AlSi10Mg produced by selective laser melting, Physics Procedia 39 (2012) 439-446.
[153] A. Salandari-Rabori, P. Wang, Q. Dong, V. Fallah, Enhancing as-built microstructural integrity and tensile properties in laser powder bed fusion of AlSi10Mg alloy using a comprehensive parameter

optimization procedure, Materials Science and Engineering A 805 (2021) 140620.
[154] Y. Cao, X. Lin, Q.Z. Wang, S.Q. Shi, L. Ma, N. Kang, W.D. Huang, Microstructure evolution and mechanical properties at high temperature of selective laser melted AlSi10Mg, Journal of Materials Science & Technology 62 (2021) 162–172.
[155] T. Yang, T. Liu, W. Liao, E. MacDonald, H. Wei, C. Zhang, X. Chen, K. Zhang, Laser powder bed fusion of AlSi10Mg: Influence of energy intensities on spatter and porosity evolution, microstructure and mechanical properties, Journal of Alloys and Compounds 849 (2020) 156300.
[156] C. Zhang, H. Zhu, Z. Hu, L. Zhang, X. Zeng, A comparative study on single-laser and multi-laser selective laser melting AlSi10Mg defects, microstructure and mechanical properties, Materials Science and Engineering A 746 (2019) 416-423.
[157] M. Fousová, D. Dvorský, A. Michalcová, D. Vojtěch, Changes in the microstructure and mechanical properties of additively manufactured AlSi10Mg alloy after exposure to elevated temperatures, Materials Characterization 137 (2018) 119-126.
[158] W. Li, S. Li, J. Liu, A. Zhang, Y. Zhou, Q. Wei, C. Yan, Y. Shi, Effect of heat treatment on AlSi10Mg alloy fabricated by selective laser melting: Microstructure evolution, mechanical properties and fracture mechanism, Materials Science and Engineering A 663 (2016) 116-125.
[159] K. Riener, N. Albrecht, S. Ziegelmeier, R. Ramakrishnan, L. Haferkamp, A.B. Spierings, G.J. Leichtfried, Influence of particle size distribution and morphology on the properties of the powder feedstock as well as of AlSi10Mg parts produced by laser powder bed fusion (LPBF), Additive Manufacturing 34 (2020) 101286.
[160] B. Amir, E. Grinberg, Y. Gale, O. Sadot, S. Samuha, Influences of platform heating and post-processing stress relief treatment on the mechanical properties and microstructure of selective-laser-melted AlSi10Mg alloys, Materials Science and Engineering A 822 (2021) 141612.
[161] D. Buchbinder, W. Meiners, N. Pirch, K. Wissenbach, J. Schrage, Investigation on reducing distortion by preheating during manufacture of aluminum components using selective laser melting, Journal of Laser Applications 26 (2014) 012004.
[162] A. Mehta, L. Zhou, H. Hyer, T. Huynh, B. Lu, K. Graydon, E.J. Drobner, S.H. Park, Y. Sohn, Microstructural characteristics and mechanical properties of additively manufactured Cu-10Sn alloys by laser powder bed fusion, Materials Science and Engineering A 838 (2022) 142775.
[163] H. Hyer, A. Mehta, K. Graydon, N. Kljestan, M. Knezevic, D. Weiss, B. McWilliams, K. Cho, Y. Sohn, High strength aluminum-cerium alloy processed by laser powder bed fusion, Additive Manufacturing 52 (2022) 102657.
[164] T. Pardoen, J.W. Hutchinson, Micromechanics-based model for trends in toughness of ductile metals, Acta Materialia 51 (2003) 133-148.
[165] A.T. Kermanidis, A. Tzamtzis, Analytical modeling of fatigue crack propagation based on cyclic hardening and a characteristic damage length, International Journal of Fatigue 141 (2020) 105684.
[166] A. Deschamps, Y. Bréchet, Influence of predeformation and ageing of an Al-Zn-Mg alloy-II. Modeling of precipitation kinetics and yield stress, Acta Materialia 47 (1999) 293-305.
[167] A.J. Ardell, Precipitation hardening, Metallurgical and Materials Transactions A 16 (1985) 2131-2165.
[168] Z. Saghi, P.A. Midgley, Electron tomography in the (S)TEM: from nanoscale morphological analysis to 3D atomic imaging, Annual Review of Materials Research 42 (2012) 59-79.
[169] X.X. Zhang, H. Andrä, S. Harjo, W. Gong, T. Kawasaki, A. Lutz, M. Lahres, Quantifying internal strains, stresses, and dislocation density in additively manufactured AlSi10Mg during loading-unloading-reloading deformation, Materials and Design 198 (2021) 109339.
[170] D. Ben, Y. Ma, H. Yang, L. Meng, X. Shao, H. Liu, S.Wang, Q. Duan, Z. Zhang, Heterogeneous microstructure and voids dependence of tensile deformation in a selective laser melted AlSi10Mg alloy, Materials Science and Engineering A 798 (2020) 140109.
[171] L. Song, L. Zhao, L. Ding, Y. Zhu, M. Huang, A. Simar, Z. Li, Microstructure and loading direction dependent hardening and damage behavior of laser powder bed fusion AlSi10Mg, Materials Science and Engineering A 832 (2022) 142484.
[172] L. Zhao, A. Maynadier, D. Nelias, Stiffness and fracture analysis of photovoltaic grade silicon plates, International Journal of Solids and Structures 97-98 (2016) 355-369.

[173] S.I. Tan, B.S. Berry, B.L. Crowder, Elastic and Anelastic Behavior of Ion-Implanted Silicon, Applied Physics Letters 20 (1972) 88-90.
[174] X. Zhang, J.D. Comins, A.G. Every, P.R. Stoddart, W. Pang, Surface Brillouin scattering study of the surface excitations in amorphous silicon layers produced by ion bombardment, Physical Review B 58 (1998) 13677-13685.
[175] M.D. Kluge, J.R. Ray, Elastic constants and density of states of a molecular-dynamics model of amorphous silicon, Physical Review B 37 (1988) 4132-4136.
[176] C. Mathioudakis, P.C. Kelires, Softening of elastic moduli of amorphous semiconductors, Journal of Non-Crystalline Solids 266-269 (2000) 161-165.
[177] Y. Wang, J. Ding, Z. Fan, L. Tian, M. Li, H. Lu, Y. Zhang, E. Ma, J. Li, Z. Shan, Tension-compression asymmetry in amorphous silicon, Nature Materials (2021).
[178] D.-K. Kim, J.-H. Hwang, E.-Y. Kim, Y.-U. Heo, W. Woo, S.-H. Choi, Evaluation of the stress-strain relationship of constituent phases in AlSi10Mg alloy produced by selective laser melting using crystal plasticity FEM, Journal of Alloys and Compounds 714 (2017) 687-697.
[179] A. Pineau, A.A. Benzerga, T. Pardoen, Failure of metals I: Brittle and ductile fracture, Acta Materialia 107 (2016) 424-483.
[180] M. Schuch, T. Hahn, M. Bleckmann, The mechanical behavior and microstructure of additively manufactured AlSi10Mg for different material states and loading conditions, Materials Science and Engineering A 813 (2021) 141134.
[181] A. Suzuki, T. Miyasaka, N. Takata, M. Kobashi, M. Kato, Control of microstructural characteristics and mechanical properties of AlSi12 alloy by processing conditions of laser powder bed fusion, Additive Manufacturing 48 (2021) 102383.
[182] P. Li, Y. Kim, A.C. Bobel, L.G. Hector Jr., A.K. Sachdev, S. Kumar, A.F. Bower, Microstructural origin of the anisotropic flow stress of laser powder bed fused AlSi10Mg, Acta Materialia 220 (2021) 117346.
[183] V.C. Nardone, K.M. Prewo, On the strength of discontinuous silicon carbide reinforced aluminum composites, Scripta Metallurgica 20 (1986) 43-48.
[184] H.J. Ryu, S.I. Cha, S.H. Hong, Generalized shear-lag model for load transfer in SiC/Al metal-matrix composites, Journal of Materials Research 18 (2003) 2851-2858.
[185] X.X. Zhang, H. Andrä, Crystal plasticity simulation of the macroscale and microscale stress-strain relations of additively manufactured AlSi10Mg alloy, Computational Materials Science 200 (2021) 110832.
[186] L. Babout, E. Maire, R. Fougères, Damage initiation in model metallic materials: X-ray tomography and modelling, Acta Materialia 52 (2004) 2475-2487.
[187] F. Hannard, T. Pardoen, E. Maire, C.L. Bourlot, R. Mokso, A. Simar, Characterization and micromechanical modelling of microstructural heterogeneity effects on ductile fracture of 6xxx aluminium alloys, Acta Materialia 103 (2016) 558-572.
[188] T.H. Becker, P. Kumar, U. Ramamurty, Fracture and fatigue in additively manufactured metals, Acta Materialia 219 (2021) 117240.
[189] K. Lee, Y.N. Kwon, S. Lee, Effects of eutectic silicon particles on tensile properties and fracture toughness of A356 aluminum alloys fabricated by low-pressure-casting, casting-forging, and squeeze-casting processes, Journal of Alloys and Compounds 461 (2008) 532-541.
[190] N.D. Alexopoulos, M. Tiryakioğlu, Relationship between fracture toughness and tensile properties of A357 cast aluminium alloy, Metallurgical and Materials Transactions A 40A (2009) 702-716.
[191] L. Hitzler, J. Hirsch, J. Schanz, B. Heine, M. Merkel, W. Hall, A. Öchsner, Fracture toughness of selective laser melted AlSi10Mg, Proceedings of the Institution of Mechanical Engineers, Part L: Journal of Materials: Design and Applications 233 (2019) 615-621.
[192] R.O. Ritchie, The conflicts between strength and toughness, Nature Materials 10 (2011) 817-822.
[193] L. Zhao, L. Ding, J. Soete, H. Idrissi, G. Kerckhofs, A. Simar, Fostering crack deviation via local internal stresses in Al/NiTi composites and its correlation with fracture toughness, Composites Part A: Applied Science and Manufacturing 126 (2019) 105617.
[194] J.A. Bannantine, J. Comer, J.L. Handrock, Fundamentals of metal fatigue analysis, Prentice-Hall, Englewood Gliffs, NJ (1990).

[195] A. Pineau, D.L. McDowell, E.P. Busso, S.D. Antolovich, Failure of metals II: Fatigue, Acta Materialia 107 (2016) 484-507.
[196] G. Qian, C. Zhou, Y. Hong, Experimental and theoretical investigation of environmental media on very-high-cycle fatigue behavior for a structural steel, Acta Materialia 59 (2011) 1321-1327.
[197] S. Romano, L. Patriarca, S. Foletti, S. Beretta, LCF behaviour and a comprehensive life prediction model for AlSi10Mg obtained by SLM, International Journal of Fatigue 117 (2018) 47-62.
[198] M.S. Baek, R. Kreethi, T.H. Park, Y. Sohn, K.A. Lee, Influence of heat treatment on the high-cycle fatigue properties and fatigue damage mechanism of selective laser melted AlSi10Mg alloy, Materials Science and Engineering A 819 (2021) 141486.
[199] G. Qian, Z. Jian, Y. Qian, X. Pan, X. Ma, Y. Hong, Very-high-cycle fatigue behavior of AlSi10Mg manufactured by selective laser melting: Effect of build orientation and mean stress, International Journal of Fatigue 138 (2020) 105696.
[200] A. Tridello, J. Fiocchi, C.A. Biffi, G. Chiandussi, M. Rossetto, A. Tuissi, D.S. Paolino, Influence of the annealing and defects on the VHCF behavior of an SLM AlSi10Mg alloy, Fatigue & Fracture of Engineering Materials & Structures 42 (2019) 2794-2807.
[201] J.G. Santos Macías, L. Zhao, D. Tingaud, B. Bacroix, G. Pyka, C. van der Rest, L. Ryelandt, A. Simar, Hot isostatic pressing of laser powder bed fusion AlSi10Mg: parameter identification and mechanical properties, Journal of Materials Science (2022).
[202] Y. Nadot, C. Nadot-Martin, W. Kan, S. Boufadene, M. Foley, J. Cairney, G. Proust, L. Ridosz, Predicting the fatigue life of an AlSi10Mg alloy manufactured via laser powder bed fusion by using data from computed tomography, Additive Manufacturing 32 (2020) 100899.
[203] M. Tang, P.C. Pistorius, Oxides, porosity and fatigue performance of AlSi10Mg parts produced by selective laser melting, International Journal of Fatigue 94 (2017) 192-201.
[204] Y. Murakami, Metal fatigue: effects of small defects nonmetallic inclusions, Oxford: Elsevier (2002).
[205] Y. Hong, X. Liu, Z. Lei, C. Sun, The formation mechanism of characteristic region at crack initiation for very-high-cycle fatigue of high-strength steels, International Journal of Fatigue 89 (2016) 108-118.
[206] J. Li, J. Sun, G. Qian, L. Shi, Defect-induced cracking and fine granular characteristics in very-high-cycle fatigue of laser powder bed fusion AlSi10Mg alloy, International Journal of Fatigue 158 (2022) 106770.
[207] M.T. Di Giovanni, J.T. Oliveira de Menezes, G. Bolelli, E. Cerri, E.M. Castrodeza, Fatigue crack growth behavior of a selective laser melted AlSi10Mg, Engineering Fracture Mechanics 217 (2019) 106564.
[208] B. Pyttel, D. Schwerdt, C. Berger, Very high cycle fatigue-Is there a fatigue limit?, International Journal of Fatigue 33 (2011) 49-58.
[209] S. Beretta, More than 25 years of extreme value statistics for defects: Fundamentals, historical developments, recent applications, International Journal of Fatigue 151 (2021) 106407.
[210] Y. Murakami, Analysis of stress intensity factors of modes I, II and III for inclined surface cracks of arbitrary shape, Engineering Fracture Mechanics 22 (1985) 101-114.
[211] H. Kitagawa, S. Takahashi, Applicability of fracture mechanics to very small cracks or the cracks in the early stage, In: Proc 2nd int confmech behaviour of materials – ICM2 627–631.
[212] S. Beretta, S. Romano, A comparison of fatigue strength sensitivity to defects for materials manufactured by AM or traditional processes, International Journal of Fatigue 94 (2017) 178-191.
[213] S. Romano, A. Brandão, J. Gumpinger, M. Gschweitl, S. Beretta, Qualification of AM parts: Extreme value statistics applied to tomographic measurements, Materials and Design 131 (2017) 32-48.
[214] Y. Murakami, M. Endo, Effect of defects, inclusions and inhomogeneities on fatigue strength, International Journal of Fatigue 16 (1994) 163-182.
[215] M.H. El Haddad, T.H. Topper, K.N. Smith, Prediction of non propagating cracks, Engineering Fracture Mechanics 11 (1979) 573-584.
[216] W. Schneller, M. Leitner, S. Leuders, J.M. Sprauel, F. Grün, T. Pfleifer, O. Jantschner, Fatigue strength estimation methodology of additively manufactured metallic bulk material, Additive Manufacturing 39 (2021) 101688.
[217] W. Qian, S. Wu, Z. Wu, S. Ahmed, W. Zhang, G. Qian, P.J. Withers, In situ X-ray imaging of fatigue crack growth from multiple defects in additively manufactured AlSi10Mg alloy, International Journal of

Fatigue 155 (2022) 106616.
[218] M.-L. Zhu, L. Jin, F.-Z. Xuan, Fatigue life and mechanistic modeling of interior micro-defect induced cracking in high cycle and very high cycle regimes, Acta Materialia 157 (2018) 259-275.
[219] J. Zhang, J. Li, S. Wu, W. Zhang, J. Sun, G. Qian, High-cycle and very-high-cycle fatigue lifetime prediction of additively manufactured AlSi10Mg via crystal plasticity finite element method, International Journal of Fatigue 155 (2022) 106577.
[220] Y. Li, H. Xu, W. Lai, Z. Li, X. Su, A Multiscale Material Modeling Approach to Predict the Mechanical Properties of Powder Bed Fusion (PBF) Metal, in: N.S.a.M. Seifi (Ed.) Structural Integrity of Additive Manufactured Materials and Parts, 2020, pp. 203–213.
[221] V. Romanova, R. Balokhonov, O. Zinovieva, E. Emelianova, E. Dymnich, M. Pisrev, A. Zinoviev, Micromechanical simulations of additively manufactured aluminum Alloys, Computers and Structures 244 (2021) 106412.
[222] S.R. Kalidindi, C.A. Bronkhorst, L. Anaud, Crystallographic texture evolution in bulk deformation processing of FCC metals, Journal of the Mechanics and Physics of Solids 40 (1992) 537-569.
[223] V. Romanova, R. Balokhonov, A method of step-by-step packing and its application in generating 3D microstructures of polycrystalline and composite materials, Engineering with Computers 37 (2021) 241-250.
[224] X.X. Zhang, D. Knoop, H. Andrä, S. Harjo, T. Kawasaki, A. Lutz, M. Lahres, Multiscale constitutive modeling of additively manufactured Al–Si–Mg alloys based on measured phase stresses and dislocation density, International Journal of Plasticity 140 (2021) 102972.
[225] G.I. Taylor, The mechanism of plastic deformation of crystals. Part I. Theoretical, Proceedings of the Royal Society A: Mathematical, Physical and Engineering Sciences 145 (1934) 362-387.
[226] E. Voce, A practical strain hardening function, Metallurgia 51 (1955) 219-226.
[227] Y. Estrin, H. Mecking, A unified phenomenological description of work hardening and creep based on one-parameter models, Acta Metallurgica 32 (1984) 57-70.
[228] D. Peirce, R.J. Asaro, A. Needleman, An analysis of nonuniform and localized deformation in ductile single crystals, Acta Metallurgica 30 (1982) 1087-1119.
[229] M. Ben Haj Slama, L. Yedra, E. Heripre, M.V. Upadhyay, Insight on precipitate evolution during additive manufacturing of stainless steels via in-situ heating-cooling experiments in a transmission electron microscope, Materialia 21 (2022) 101368.
[230] H. Azizi, A. Ebrahimi, N. Ofori-Opoku, M. Greenwood, N. Pravatas, M. Mohammadi, Characterizing the microstructural effect of build direction during solidification of laser-powder b e d fusion of Al-Si alloys in the dilute limit: A phase-field study, Acta Materialia 214 (2021) 116983.
[231] P. He, Q. Liu, J.J. Kruzic, X. Li, Machine-learning assisted additive manufacturing of a TiCN reinforced AlSi10Mg composite with tailorable mechanical properties, Materials Letters 307 (2022) 131018.
[232] W.A. Scrivens, Y. Luo, M.A. Sutton, S.A. Collette, M.L. Myrick, P. Miney, P.E. Colavita, A.P. Reynolds, X. Li, Development of patterns for digital image correlation measurements at reduced length scales, Experimental Mechanics 47 (2007) 63-77.
[233] A. Orozco-Caballero, D. Lunt, J.D. Robson, J.Quinta da Fonseca, How magnesium accommodates local deformation incompatibility: A high-resolution digital image correlation study, Acta Materialia 133 (2017) 367-379.
[234] S. Shafqat, J.P.M. Hoefnagels, Cool, dry, nano-scale DIC patterning of delicate, heterogeneous, non-planar specimens by micro-mist nebulization, Experimental Mechanics 61 (2021) 917-937.
[235] F. Di Gioacchino, J. Quinta da Fonseca, Plastic strain mapping with sub-micron resolution using digital image correlation, Experimental Mechanics 53 (2013) 743-754.
[236] C.S. Han, H. Gao, Y. Huang, W.D. Nix, Mechanism-based strain gradient crystal plasticity-I. Theory, Journal of the Mechanics and Physics of Solids 53 (2005) 1188-1203.
[237] C.S. Han, H. Gao, Y. Huang, W.D. Nix, Mechanism-based strain gradient crystal plasticity-II. Analysis, Journal of the Mechanics and Physics of Solids 53 (2005) 1204-1222.
[238] Y. Huang, S. Qu, K.C. Hwang, M. Li, H. Gao, A conventional theory of mechanism-based strain gradient plasticity, International Journal of Plasticity 20 (2004) 753-782.
[239] F. Rosters, P. Eisenlohr, L. Hantcherli, D.D. Tjahjanto, T.R. Bieler, D. Raabe, Overview of constitutive

laws, kinematics, homogenization and multiscale methods in crystal plasticity finite-element modeling: Theory, experiments, applications, Acta Materialia 58 (2010) 1152-1211.
[240] A.L. Gurson, Continuum theory of ductile rupture by void nucleation and growth: Part I-yield criteria and flow rules for porous ductile media, Journal of Engineering Materials and Technology (1977).
[241] C.C. Chu, A. Needleman, Void nucleation effects in biaxially streched sheets, Journal of Engineering Materials and Technology 102 (1980) 249-256.
[242] V. Tvergaard, A. Needleman, Analysis of the cup-cone fracture in a round tensile bar, Acta Metallurgica 32 (1984) 157-169.
[243] J. Lemaitre, A continuous damage mechanics model for ductile fracture, Journal of Engineering Materials and Technology 107 (1985) 83-89.
[244] Y.K. Xiao, Z.Y. Bian, Y. Wu, G. Ji, Y.Q. Li, M.J. Li, Q. Lian, Z. Chen, A. Addad, H.W. Wang, Effect of nano-TiB2 particles on the anisotropy in an AlSi10Mg alloy processed by selective laser melting, Journal of Alloys and Compounds 798 (2019) 644-655.